# A.C. Magnetic Susceptibility in the Study of Magnetic Systems




Craig Victor Topping

Worcester College

University of Oxford

A thesis submitted for the degree of

*Doctor of Philosophy*

Trinity Term 2018

**A.C. Magnetic Susceptibility in the Study of Magnetic Systems**

Craig Victor Topping, Worcester College, University of Oxford, Trinity Term 2018

**Abstract of thesis submitted for the degree of Doctor of Philosophy**

This thesis describes the application of various techniques to the study of magnetic phenomena in condensed matter systems with a particular focus given to a.c. magnetic susceptibility. This is accomplished by briefly discussing the basic theory of condensed matter magnetism before describing measurement techniques employed in this thesis. I discuss magnetometry in detail, contrasting d.c. susceptibility with a.c. susceptibility in the context of the applicability of the latter to the study of slow magnetic dynamics. In order to understand the a.c. response of materials containing slow magnetic dynamics I take a theoretical approach and show how the commonly used models for describing such behaviour arise from the more overarching linear response theory. I then show common treatments of a.c. susceptibility data before reviewing the a.c. response of various classes of material while discussing the origin of the associated magnetic sluggishness.

Subsequently, I show studies of two different classes of material showing magnetic sluggishness. In the first study of single-molecule magnets two families are examined: the simpler $Co_2^{3+}Ln^{3+}$ family (Ln = Gd, Ho, Tb and Er) and the more complex $Ni_4^{2+}Ln_4^{3+}$ family (Ln = Gd, Ho, Dy, and Tb). By beginning with the $Co_2Ln$ family in which only the central $Ln^{3+}$ ion possesses a magnetic moment I use a.c. susceptibility to show the Tb and Er analogues to display field-induced slow magnetic relaxation consistent with single-molecule magnet behaviour while the Gd and Ho analogues do not. Combining these results with d.c. magnetic measurements in the context of the structure of these compounds allows the origin of this behaviour to be shown to be associated with the relevant $Ln^{3+}$ ions. This sets out the process utilised for elucidating the magnetic behaviour of the more complex $Ni_4^{2+}Ln_4^{3+}$ family in which both transition metal ions and lanthanide ions possess a magnetic moment. As such, the possible magnetic exchanges between ions are evaluated using d.c. techniques and I propose the Dy and Tb analogues to form Ni–Ln dimers (ferromagnetic and antiferromagnetic respectively). Using a.c. susceptibility I demonstrate $Ni_4Dy_4$ and $Ni_4Tb_4$ to display field-induced slow magnetic relaxation of single-molecule magnet origin only in $Ni_4Dy_4$.

The second study I present focuses on the low temperature magnetism associated with the superconducting family $Li_{1-x}Fe_x(OH)Fe_{1-y}Se$ which is comprised of alternating two-dimensional layers of $Fe_{1-y}Se$ and $Li_{1-x}Fe_x(OH)$. The $Fe^{2+}$ ions of the hydroxide layer possess a magnetic moment and by considering a random distribution of these ions in such a layer I suggest the low temperature magnetic state to likely be disordered and spin glass-like. Taking advantage of samples provided by synthetic chemists of superconducting and non-superconducting members of this family I show that d.c. magnetometry and heat capacity measurements support a spin glass-like state. A.c. susceptibility and $\mu$SR measurements demonstrate that the magnetic state of $Li_{1-x}Fe_x(OH)Fe_{1-y}Se$ contains slow relaxation of a spin glass type.

# Acknowledgements

There are many people I owe thanks to over the course of my research. It is difficult to list them all but nonetheless I hope to express my gratitude.

I am deeply indebted to the many members of Quantum Materials at Oxford, old and new. They have been extraordinarily welcoming and supportive over my time at Oxford making research a much more pleasant endeavour. I hope this continues for many years to come.

I owe great thanks to my supervisor, Stephen Blundell. He has been a great supervisor and fostered a fantastic working atmosphere making it comfortable to discuss any aspect of research. I am also thankful to the other members of his group: Franz, Fran and Matt. I must apologise to Dharmalingam Prabhakaran for so often being the bearer of bad news and finding some new problem with a Quantum Design product. His help has been invaluable. I also give thanks to Nathaniel Davies who had the misfortune to be at the desk next to me and act as my sounding board for the past few years. I would also like to thank Paul Goddard and Jamie Brambleby for several enjoyable collaborations. My thesis also owes great thanks to Daniel Woodruff and the rest of Simon Clarke's group in Chemistry for providing samples. I also thank Rob Storey and Kieran McCall for always having helium.

Special thanks must be given to the pulsed magnetic field laboratory at Oxford, the Nicholas Kurti Magnetic Field Laboratory. If the upgrade of this had not been beset by various delays (including the appearance of an indoor pool) this thesis would have looked very different. Despite the difficulties associated with this project it has been a joy working on it with Stephen Blundell, Rob Storey, Tony Hickman, Paul Goddard and Johan Fopma. It seems misery does indeed love company.

Finally, I thank my friends back home, family and my dearest, Nicole. You have all made this possible.

# List of Publications

C. V. Topping and S. J. Blundell, **A.C. susceptibility as a probe of low-frequency magnetic dynamics**, *J. Phys. Condens. Matter*, *Accepted*.

P. Chen, B. Holinsworth, K. O'Neal, X. Luo, C. V. Topping, S.-W. Cheong, J. Singleton, E. S. Choi and L. Musfeldt, **Frustration and glassy character in $RIn_{1-x}Mn_xO_3$ (R = Tb, Dy, Gd)**, *Inorg. Chem.*, 57, 12501–12508, (2018).

J. E. Page, C. V. Topping, A. Scrimshire, P. A. Bingham, P. Manuel, S. J. Blundell and M. A. Hayward, **$Sr_2FeIrO_6$ revisited - phase separation and a $J_{eff} \neq 0$ state for $Ir^{5+}$?**, *Inorg. Chem.*, 57, 10303–10311, (2018).

C. V. Topping, F. K. K. Kirschner, S. J. Blundell, P. J. Baker, D. N. Woodruff, F. Schild, H. Sun and S. J. Clarke, **Coexistence of magnetism and superconductivity in separate layers of the iron-based superconductor $Li_{1-x}Fe_x(OH)Fe_{1-y}Se$**, *Phys. Rev. B*, 95, 134419, (2017).

J. Brambleby, P. A. Goddard, J. Singleton, M. Jaime, T. Lancaster, L. Huang, J. Wosnitza, C. V. Topping, K. E. Carreiro, H. E. Tran, Z. E. Manson J. L. Manson, **Adiabatic physics of an exchange-coupled spin-dimer system: Magnetocaloric effect, zero-point fluctuations, and possible two-dimensional universal behaviour**, *Phys. Rev. B*, 95, 024404, (2017).

J. Singleton, J. W. Kim, C. V. Topping, A. Hansen, E.-D. Mun, S. Chikara, I. Lakis, S. Ghannadzadeh, P. A. Goddard, X. Luo, Y. S. Oh, S.-W. Cheong and V. S. Zapf, **Magnetic properties of $Sr_3NiIrO_6$ and $Sr_3CoIrO_6$: Magnetic hysteresis with coercive fields of up to 55 T**, *Phys. Rev. B*, 94, 224408, (2016).

F. K. K. Kirschner, F. Lang, C. V. Topping, P. J. Baker, F. L. Pratt, S. E. Wright, D. N. Woodruff, S. J. Clarke and S. J. Clarke, **Robustness of superconductivity to competing magnetic phases in tetragonal FeSe**, *Phys. Rev. B*, 94, 134509, (2016).

D. N. Woodruff, F. Schild, C. V. Topping, S. J. Cassidy, J. N. Blandy, S. J. Blundell, A. L. Thompson and S. J. Clarke, **The Parent Li(OH)FeSe Phase of Lithium Iron Hydroxide Selenide Superconductors**, *Inorg. Chem.*, 55, 9886, (2016).

P. A. Goddard, J. Singleton, I. Franke, J. S. Möller, T. Lancaster, A. J. Steele, C. V. Topping, S. J. Blundell, F. L. Pratt, C. Baines, J. Bendix, R. D. McDonald, J. Brambleby, M. R. Lees, S. H. Lapidus, P. W. Stephens, B. W. Twamley,

M. M. Conner, K. Funk, J. F. Corbey, H. E. Tran, J. A. Schlueter and J. L Manson, **Control of the third dimension in copper-based square-lattice antiferromagnets**, *Phys. Rev. B*, 93, 094430, (2016).

S. Biswas, J. Goura, S. Das, C. V. Topping, J. Brambleby, P. A. Goddard and V. Chandrasekhar, **Octanuclear Heterobimetallic $\{Ni_4Ln_4\}$ Assemblies Possessing $Ln_4$ Square Grid [2 × 2] Motifs: Synthesis, Structure and Magnetism**, *Inorg. Chem.*, 55, 8422, (2016).

J. Goura, J. Brambleby, C. V. Topping, P. A. Goddard, R. S. Narayanan, A. K. Bar and V. Chandrasekhar, **Heterometallic trinuclear $\{Co^{III}_2Ln^{III}\}$ (Ln = Gd, Tb, Ho and Er) complexes in a bent geometry. Field-induced single-ion magnetic behaviour of the $Er^{III}$ and $Tb^{III}$ analogues**, *Dalton Trans.*, 45, 9235, (2016).

A. Sinclair, J. A. Rodgers, C. V. Topping, M. Míšek, R. D. Stewart, W. Kockelmann, J.-W. G. Bos and J. P. Attfield, **Synthsis and Properties of Lanthanide Ruthenium(III) Oxide Perovskites**, *Angew. Chem. Int. Ed.*, 53, 8343, (2014).

T. Lancaster, P. A. Goddard, S. J. Blundell, F. R. Foronda, S. Ghannadzadeh, J. S. Möller, P. J. Baker, F. L. Pratt, C. Baines, L. Huang, J. Wosnitza, R. D. McDonald, K. A. Modic, J. Singleton, C. V. Topping, T. A. W. Beale, F. Xiao, J. A. Schlueter, A. M. Barton, R. D. Cabrera, K. E. Carreiro, H. E. Tran and J. L. Manson, **Controlling Magnetic Order and Quantum Disorder in Molecule-Based Magnets**, *Phys. Rev. Lett.*, 112, 207201, (2014).

S. H. Lapidus, J. L. Manson, J. Liu, M. J. Smith, P. A, Goddard, J. Bendix, C. V. Topping, J. Singleton, C. Dunmars, J. F. Mitchell and J. A. Schlueter, **Quantifying magnetic exchange in doubly-bridged Cu–$X_2$–Cu (X = F, Cl, Br) chains enabled by solid state synthesis of $CuF_2$(pyrazine)**, *Chem. Commun.*, 49, 3558, (2013).

*“Ah, the outdoors,” Shallan said. “I visited that mythical place once.”*

*— Brandon Sanderson, The Way of Kings*

For my parents and for Nicole

# Contents

**Abstract** i

**Acknowledgements** ii

**List of Publications** iii

**1 Condensed Matter Magnetism (and Briefly Superconductivity)** 1
- 1.1 Introduction and Significance . . . 1
- 1.2 Magnetism and Atoms . . . 2
- 1.3 The Interaction of Magnetic Moments . . . 12
- 1.4 Order and Frustration . . . 17
- 1.5 Superconductivity . . . 22

**2 Non-magnetometry Techniques** 26
- 2.1 Introduction . . . 26
- 2.2 Heat Capacity . . . 26
- 2.3 $\mu$SR . . . 32
- 2.4 Scattering . . . 38

**3 D.C. and A.C. Magnetometry** 44
- 3.1 Introduction . . . 44
- 3.2 D.C. Magnetic Susceptibility . . . 45
- 3.3 A.C. Magnetic Susceptibility . . . 47
  - 3.3.1 Three characteristic regimes . . . 47
  - 3.3.2 Linear response theory . . . 50
  - 3.3.3 The damped harmonic oscillator . . . 51
  - 3.3.4 Dielectric relaxation . . . 55
  - 3.3.5 A range of relaxation times . . . 56
  - 3.3.6 The Cole-Cole plot . . . 63
  - 3.3.7 A.C. Susceptometer . . . 64
- 3.4 Application to real experimental systems . . . 66
  - 3.4.1 Superparamagnets and Single-Molecule Magnets . . . 66
  - 3.4.2 Spin Glasses . . . 75
  - 3.4.3 Spin Ice . . . 78
  - 3.4.4 Long Range Magnetic Order . . . 80
  - 3.4.5 Paramagnetism . . . 82
  - 3.4.6 Superconductors . . . 83

3.5 Conclusion . . . . . 88

**4 Studies of Two Families of Lanthanide-based Single-Molecule Magnets 89**
4.1 Introduction . . . . . 89
4.2 The $Co_2Ln$ Family . . . . . 91
4.2.1 Experimental Methods . . . . . 91
4.2.2 Synthesis and Structure . . . . . 92
4.2.3 D.C. Magnetometry . . . . . 93
4.2.4 A.C. Magnetometry . . . . . 97
4.2.5 Origin of Lanthanide Anisotropy . . . . . 107
4.2.6 Conclusion . . . . . 109
4.3 The $Ni_4Ln_4$ . . . . . 110
4.3.1 Experimental Methods . . . . . 111
4.3.2 Synthesis and Structure . . . . . 111
4.3.3 Possible Magnetic Exchanges . . . . . 113
4.3.4 A.C. Magnetometry . . . . . 122
4.3.5 Conclusion . . . . . 133
4.4 General Conclusion . . . . . 134

**5 Layer-based Magnetism in the $Li_{1-x}Fe_x(OH)Fe_{1-y}Se$ Family 136**
5.1 Introduction . . . . . 136
5.2 Experimental Methods . . . . . 138
5.3 Synthesis and Structure . . . . . 139
5.4 The Hydroxide Layer . . . . . 140
5.5 D.C. Magnetometry . . . . . 141
5.6 A.C. Magnetometry . . . . . 144
5.7 Heat Capacity . . . . . 148
5.8 ZF-$\mu$SR . . . . . 152
5.9 Conclusion . . . . . 153

**6 Concluding Remarks 155**

**A The Generalised Debye Model 158**

# Chapter 1

# Condensed Matter Magnetism (and Briefly Superconductivity)

## 1.1 Introduction and Significance

The phenomenon of magnetism has captured the imagination of people for thousands of years. An average person will likely have a (knowing) first encounter with magnetism as a child with permanent magnets decorating a refrigerator or in some manner of toy. In a young mind an invisible force that can attract or repel certain objects ignites thoughts of no less than magic. On maturity such wonder typically dims with less thought given to magnetism; relegating it to a novelty or a small, convenient tool. This simply does not do justice the influence magnetism has had on the development of human civilisation. Magnets have helped shape the past and are ubiquitous and integral to modern life.

The origin of the compass in China in the $11$th and $12$th centuries proved a great stride forward in naval navigation and the realisation in the $1800$s of the intrinsic link between electricity and magnetism allowed Michael Faraday to build the first electric generator literally powering modern society. The advent of quantum mechanics allowed an explanation of why solids such as a lodestone could be magnetic (the magnetism of condensed matter). This explained the

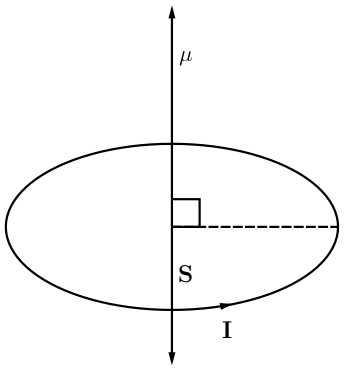



Figure 1.1: Graphic illustration of the relationship between magnetic moment ($\boldsymbol{\mu}$), current ($\boldsymbol{I}$) and associated angular momentum ($\boldsymbol{S}$) for an electron. Due to the definition of current as the flow of positive charge $\boldsymbol{\mu}$ and $\boldsymbol{S}$ are anti-parallel.

workings of possibly the first known magnets and also offered insights into all materials leading to many of today's devices which incorporate some form of magnetism such as various forms of data storage, magnetic resonance imaging (MRI) devices and speakers. As such, there is considerable modern research devoted to the understanding of the magnetism of condensed matter, especially exotic states, with the possibility of device application in the future.

This chapter aims to give a brief introduction to magnetism in condensed matter to highlight key concepts that have been utilised throughout the enclosed research. This is by no means a comprehensive overview with a more detailed introduction available in Ref. [1]. Additionally, a short foray into superconductivity is made.

## 1.2 Magnetism and Atoms

It is useful and instructional to consider how atoms and ions may be magnetic. Maxwell's equations demonstrate that electricity and magnetism are linked with the Bio-Savart law specifically quantifying the magnetic field produced in the presence of a moving charge [1]. This naturally leads to a loop of current de-

scribing a magnetic dipole moment, $\boldsymbol{\mu}$. More simply (since a loop of current consists of moving electrons with an angular momentum, $\boldsymbol{L}$) any object possessing charge and angular momentum can be defined to possess an associated magnetic moment,

$$\boldsymbol{\mu} = \gamma \boldsymbol{L}, \tag{1.1}$$

where $\gamma$ is the gyromagnetic ratio [1]. Fig. 1.1 demonstrates this graphically. Therefore, the magnetic moment of an atom may arise from the angular momenta of the charged electrons or nuclei. In quantifying the magnitude of these moments the natural units are the Bohr magneton, $\mu_{\mathrm{B}}$, and the nuclear magneton, $\mu_{\mathrm{N}}$. The former originates from the magnetic moment of an electron in the lowest energy orbit of the semi-classical Bohr model, $\mu_{\mathrm{B}} = e\hbar/2m_{\mathrm{e}}$ [1]. $\mu_{\mathrm{N}}$ is the same result replacing the mass of an electron with that of a proton. Due to the vast differences between these masses ($m_{\mathrm{e}} \ll m_{\mathrm{p}}$), $\mu_{\mathrm{B}} \gg \mu_{\mathrm{N}}$ and electrons can be considered the primary source of magnetism in condensed matter. Generally, nuclear effects can be considered a perturbation on the electron-only moments as they are much smaller effects [1, 2].

Even restricting discussion to electron-only effects matters can be further complicated by electrons possessing two forms of angular momentum, orbital ($\boldsymbol{L}$) and spin ($\boldsymbol{S}$). Thus, the moment of an atom or ion due to electrons is the sum of these two quantities,

$$\boldsymbol{\mu_{\mathrm{tot}}} = \boldsymbol{\mu_L} + \boldsymbol{\mu_S} = -g_L \mu_{\mathrm{B}} \boldsymbol{L} - g_S \mu_{\mathrm{B}} \boldsymbol{S}, \tag{1.2}$$

where $g_L$ and $g_S$ are the electron orbital and spin g-factors respectively. Notably, the electron only moments are actually anti-parallel to their respective angular momenta. This is due to the negative charge of the electron [1, 3]. While describing a system's magnetic moment in terms of the total angular momentum,

$\boldsymbol{J} = \boldsymbol{L}+\boldsymbol{S}$, may seem more natural an obstacle exists in the application of Eq. 1.1. Due to the g-factors for $\boldsymbol{L}$ and $\boldsymbol{S}$ being unequal, $\boldsymbol{\mu_{\mathrm{tot}}} \nparallel \boldsymbol{J}$ [1–3]. Nonetheless, it would be convenient to continue to express magnetic moment as proportional to an angular momentum. This prompts the definition of an effective magnetic moment,

$$\boldsymbol{\mu_{\mathrm{eff}}} = -g_J \mu_{\mathrm{B}} \boldsymbol{J}, \tag{1.3}$$

where $g_J$ is the Landé g-factor defined as

$$g_J = \frac{3}{2} + \frac{S(S+1) - L(L+1)}{2J(J+1)}. \tag{1.4}$$

$\boldsymbol{\mu_{\mathrm{eff}}}$ is a projection of $\boldsymbol{\mu_{\mathrm{tot}}}$ on $\boldsymbol{J}$ [2, 3]. This effective moment allows an intrinsic property of the atom (the angular momentum) to be extracted if $\boldsymbol{\mu_{\mathrm{eff}}}$ is known or vice versa. Furthermore, with the energy of a classical magnetic moment in a magnetic field defined as $E = -\boldsymbol{\mu} \cdot \boldsymbol{B}$ an appropriate Hamiltonian for the interaction between an electronic moment and magnetic field can be defined as

$$\mathcal{H} = -\boldsymbol{\mu_{\mathrm{eff}}} \cdot \boldsymbol{B} = g_J \mu_{\mathrm{B}} \boldsymbol{J} \cdot \boldsymbol{B}. \tag{1.5}$$

$\boldsymbol{B}$ may be an externally applied field (leading to the Zeeman effect and hence the above being referred to as a Zeeman term in a larger Hamiltonian) [1, 2, 4]. Many other effects utilise the same form of Hamiltonian using an appropriate $\boldsymbol{\mu}$ and $\boldsymbol{B}$ such as the spin-orbit interaction [1–3] and hyperfine structure [1, 2].

This treatment has assumed a vector model in which vector quantities may be replaced by the appropriate quantum mechanical operators [2, 5]. Furthermore, the $L$-$S$ (or Russel-Saunders) coupling scheme has been adopted. While this is the typical scheme encountered (and initially taught) it is useful to remember that it results from the successive application of perturbation theory for smaller and smaller energy perturbations. Therefore it must be ensured that the stud-

ied systems obey the relative energy scale requirements for each perturbation. When attempting to solve the Hamiltonian of a $N$-electron atom, the system is simplified using the central-field approximation [2]. This takes the difficult to solve correlated multi-electron Hamiltonian

$$\mathcal{H}_{\mathrm{multi-e}} = \sum_{i=1}^{N} \left[ -\frac{\hbar^2}{2m_{\mathrm{e}}} \nabla_i^2 - \frac{Ze^2/4\pi\epsilon_0}{r_i} + \sum_{j>i}^{N} \frac{e^2/4\pi\epsilon_0}{r_{ij}} \right], \tag{1.6}$$

where $Z$ is the atomic number of the atom, $r_i$ the distance of electron $i$ from the nucleus and $r_{ij}$ is the distance from electron $i$ to $j$ and gathers all centrally acting parts of potential energy into a central field potential with the remaining parts gathered into a residual electrostatic term

$$\mathcal{H}_{\mathrm{multi-e}} = \mathcal{H}_{\mathrm{CF}} + \mathcal{H}_{\mathrm{RE}}. \tag{1.7}$$

The precise detail of $\mathcal{H}_{\mathrm{CF}}$ and $\mathcal{H}_{\mathrm{RE}}$ are unnecessary for consideration here but can be found elsewhere [2]. Importantly, $\mathcal{H}_{\mathrm{CF}} \gg \mathcal{H}_{\mathrm{RE}}$ and $\mathcal{H}_{\mathrm{CF}}$ is separable into $N$ single electron Hamiltonians (where $N$ is the number of electrons). Thus, at a first level of approximation only $\mathcal{H}_{\mathrm{CF}}$ is applicable and the energy of an atom is specified by the sum of the energy of each individual electron [2]. This naturally leads to electron configurations defined as $nl^{n_e}$ where $n$ is the principle quantum number (the electron shell), $l$ the orbital angular momentum sometimes referred to as subshell (denoted by letters $s = 0$, $p = 1$, $d = 2$, $f = 3$, etc. ) and $n_e$ is the number of electrons in that subshell. As an example, lithium with three electrons has the ground state configuration $1s^2 2s^1$.

In general, two more effects can now be considered to alter the energy of these configurations, $\mathcal{H}_{\mathrm{RE}}$ and $\mathcal{H}_{\mathrm{SO}}$. The last term here is the spin-orbit interaction. Thus, the full $\mathcal{H}_{\mathrm{multi-e}}$ is

$$\mathcal{H}_{\mathrm{multi-e}} = \mathcal{H}_{\mathrm{CF}} + \mathcal{H}_{\mathrm{RE}} + \mathcal{H}_{\mathrm{SO}}. \tag{1.8}$$

$L$-$S$ coupling applies when $E_{\mathrm{CF}} \gg E_{\mathrm{RE}} \gg E_{\mathrm{SO}}$ [2]. The residual electrostatic interaction acts on the energy levels from the central field approximation to cause splitting. This causes each individual electron's orbital and angular momenta to couple and form total versions ($\boldsymbol{L} = \sum \boldsymbol{l_i}$ and $\boldsymbol{S} = \sum \boldsymbol{s_i}$). This may be alternatively stated as $l_i$ and $s_i$ no longer being good quantum numbers while $L$ and $S$ are as they ($\hat{L^2}$, $\hat{L_z}$, $\hat{S^2}$ and $\hat{S_z}$) commute with $\mathcal{H}_{\mathrm{RE}}$ [2]. Finally, the spin-orbit interaction further splits these energy levels defined by $S$ and $L$ causing these angular momenta to couple. $\hat{L_z}$ and $\hat{S_z}$ no longer commute with the Hamiltonian. Total angular momentum $J$, with values $J = |L+S|, |L+S-1|, ..., |L-S|$, is formed in an energy splitting known as fine structure [1, 2]. These electronic energy levels are described by a term symbol

$$^{2S+1}L_J, \tag{1.9}$$

and the ground state is predicted by applying Hund's rules [1, 2, 5]:

1. Firstly, $S$ is maximised.

2. Secondly, $L$ is maximised.

3. Lastly, from the allowed values of $J$, the maximal value is chosen if the orbital subshell is less than half full and the minimal value if it is more than half full.

The first and second of these rules may be rationalised by considering that they minimise the Coulombic repulsion in the atom [1]. The last minimises the spin-orbit energy though can be violated if some other energy scale in the atom dominates this. An example of this often occurs for transition metals due to the Coulomb potential of the ions in a crystal lattice that surrounds the transition metal. This is known as the crystal field and causes the phenomenon called orbital quenching [1, 3]. This results in $L = 0$ and $J = S$ [1].

It is therefore clear that the $L$-$S$ coupling scheme may not be valid should the spin-orbit interaction exceed the strength of the residual electrostatic interaction. The spin-orbit interaction is greater for heavier elements [2] suggesting that $L$-$S$ coupling problems may arise towards the bottom of the periodic table. However, it is important to note that for the opposite condition, $E_{\mathrm{SO}} \gg E_{\mathrm{RE}}$, which leads to the $jj$ coupling scheme it is also required for $E_{\mathrm{RE}}$ to be small as well as the atom to be heavy [2]. For these situations, magnetic measurements may be made (as well as others such as spectroscopy) to identify which scheme (if either) is better obeyed.

Importantly, condensed matter magnetism has been shown to arise from the angular momenta of electrons. Succinctly, in order for an atom or ion to possess a magnetic moment it must also posses a non-zero $J$ (though this does not preclude a system displaying some magnetic properties which is discussed later). This requirement can be translated into the question, "Are there unpaired electrons?" which is typically asked of newly synthesised materials. As such, it is a very useful predictive tool for whether a system should show some form of magnetism. Violation of this (i.e. magnetic properties without unpaired electrons) likely indicates that the model of the system needs modification.

From a practical standpoint, the magnetic moment of individual atoms and ions is generally not measured during an experiment though local probes (such as $\mu$SR which is discussed in Section 2.3) can investigate this. Typically, the bulk property of magnetisation, $M$, the magnetic moment per unit volume will be measured [1, 4]. The precise method of magnetisation measurement is detailed in Chapter 3 but it is important to note that in the absence of some form of communication between moments no spontaneous, non-zero magnetisation can be present to be detected. Simply put, non-trivial bulk behaviour requires cooperation. As such, we first consider this case of isolated moments lacking communication/interaction: trivial bulk behaviour. Even considering just a classical sys-

tem it is clear that with no mechanism for cooperation or a preferred direction, moments will point randomly in all directions. Since one mole of a substance contains Avogadro's Number worth of molecules ($N_{\mathrm{A}} = 6.02 \times 10^{23}\ \mathrm{mol}^{-1}$) in real samples there will be enough magnetic moments that they will cancel one another's magnetic field and $M = 0$. To generate a non-zero magnetisation an external magnetic field must be applied to create an energetically favourable direction as described by Eq. 1.5. The only resistance to alignment are the thermal fluctuations of the moments. When other effects are allowed, such as interactions between moments and the crystal lattice, these can also resist alignment.

In fact, as shown in more detail elsewhere [1, 4], the dependence of the magnetisation of such a system with total angular momentum, $J$, on magnetic field, $B$, can be found by considering the partition function for the energy levels in a magnetic field,

$$Z = \sum_i \exp\{-E_i/k_{\mathrm{B}}T\} = \sum_{J_z=-J}^{J} \exp\{J_z g_J \mu_{\mathrm{B}} B/k_{\mathrm{B}}T\}. \tag{1.10}$$

The applied magnetic field defines the unique $z$-axis simplifying Eq. 1.5 to $E = g_J \mu_{\mathrm{B}} J_z B$. Magnetisation follows from the relation,

$$M = -\frac{\partial E}{\partial B} = n k_{\mathrm{B}} T \frac{\partial \ln Z}{\partial B}, \tag{1.11}$$

leading to the bulk magnetisation,

$$M = n g_J \mu_{\mathrm{B}} \langle J_z \rangle = n g_J \mu_{\mathrm{B}} J B_J(y). \tag{1.12}$$

$n$ is the number of spins (or atoms possessing non-zero $J$) per unit volume and $B_J(y)$ is the Brillouin function defined as

$$B_J(y) = \frac{2J+1}{2J} \coth\left(\frac{2J+1}{2J} y\right) - \frac{1}{2J} \coth \frac{y}{2J}, \tag{1.13}$$

where $y = g_J \mu_B JB/k_B T$. This function describes a monotonically increasing magnetisation with increasing applied magnetic field up to a maximal value known as the saturation magnetisation, $M_S = n g_J \mu_B J$ [1, 4]. A value of saturation magnetisation will exist for any magnetic condensed matter system, even in the forthcoming cases in which communication between moments exists. This is sensible to note given that this quantity is essentially describing the net degree of alignment of a material's individual moments with the applied field. Conceptually it is clear that eventually a magnetic field will be reached at which all moments are aligned with the applied field and any further increase will not yield an increased magnetisation.

It is also useful to consider the property called magnetic susceptibility, $\chi$, in isolated systems. This arises to relate the magnetic fields $\boldsymbol{B}$ and $\boldsymbol{H}$ to one another

$$\boldsymbol{B} = \mu_0(1+\chi)\boldsymbol{H} = \mu_0(\boldsymbol{H} + \boldsymbol{M}), \tag{1.14}$$

i.e. $\boldsymbol{B}$ consists of two components, an externally applied field, $\boldsymbol{H}$, and material contribution, $\boldsymbol{M}$ [1]. Discussion here is relegated to so called linear media in which $\boldsymbol{H}$ and $\boldsymbol{M}$ are linearly related by $\chi$, so that

$$\boldsymbol{M} = \chi \boldsymbol{H}. \tag{1.15}$$

While susceptibility will be discussed in more detail in Chapter 3 when $y \ll 1$ (at small magnetic fields and low temperatures) the Brillouin function may be simplified yielding $B_J(y) \simeq \frac{(J+1)y}{3J}$ and the susceptibility is described by

$$\chi = \frac{M}{H} \approx \frac{\mu_0 M}{B} = \frac{n\mu_0 \mu_{\text{eff}}^2}{3k_B T}, \tag{1.16}$$

which is the well known Curie's law [1, 4, 6] with $\mu_{\text{eff}} = g_J \mu_B \sqrt{J(J+1)}$. Helpfully, since $\mu_B \sim 10^{-24}$ JT$^{-1}$ and $k_B \sim 10^{-23}$ JK$^{-1}$ this condition is normally

fulfilled except at particularly low temperatures and/or high magnetic fields [1]. Generally, when measuring magnetic susceptibility low magnetic fields should always be employed to ensure the linear relation of Eq. 1.15 with lower fields making this more likely.

The magnetic state of matter described by Eqs. 1.12 and 1.16 is known as paramagnetism. As stated previously, this corresponds to independent, isolated magnetic moments. However, a paramagnetic phase should be found in all materials containing non-zero $J$ at some point in their phase diagram. This is due to thermal fluctuations such that even in the presence of interactions between moments or anisotropies due to the crystal lattice there will be some high temperature at which they are completely overcome by thermal fluctuations (assuming they do not melt before entering this phase).

Finally, before considering the interactions between moments other forms of magnetism that may exist without a permanent magnetic moment of atoms are presented. These are exceptions to the requirement of unpaired electrons.

The first of these is diamagnetism which is a form of magnetism possessed by all matter containing electrons (paired or unpaired) [1, 3, 6]. While paramagnetism shows a positive susceptibility (meaning moments align with the applied magnetic field) diamagnetism is a negative susceptibility (the resultant magnetisation opposes the applied field). Qualitatively (and classically) it can be thought of as a result of Lenz's law causing an atom's electrons to oppose an external magnetic field. Proper treatment is quantum mechanical yielding a susceptibility from first-order perturbation theory of

$$\chi = -n\frac{e^2\mu_0}{6m_e}\sum_{i=1}^{Z}\langle r_i^2\rangle, \tag{1.17}$$

where $Z$ the number of electrons and $r_i$ is the radial distance of electron $i$ from the nucleus (a spherically symmetric atom has been assumed) [1, 3]. Unlike paramagnetism, diamagnetism is a negative susceptibility and has no tempera-

ture dependence. This term is often ignored as diamagnetism is usually a much weaker effect than paramagnetism [1, 6] and is only considered in cases where paramagnetism is absent (such as filled shell atoms), when great precision is needed or if it is a particularly strong effect (such as in the phenomenon of superconductivity which will be discussed in due course).

Additionally, despite earlier discussion suggesting that a paramagnetic (positive) susceptibility should only occur for $J \neq 0$ a paramagnetic effect may still be observed when $J = 0$. As with many effects originating in quantum mechanics, the difficultly in exactly solving problems leads to the use of (generally) reasonable approximations. In perturbation theory there is indeed no *first* order energy shift if $J = 0$, however, second order effects may lead to a small, temperature independent term known as Van Vleck paramagnetism [1, 6]

$$\chi = 2\frac{N}{V}\mu_{\mathrm{B}}^2 \sum_n \frac{|\langle 0|(L_z + g_s S_z)|n\rangle|^2}{E_n - E_0}. \tag{1.18}$$

Finally, previous discussion has considered localised electrons which are more convenient to visualise for describing many magnetic phenomena. Metallic systems may display a form of paramagnetism known as Pauli paramagnetism. This may be simplistically derived with respect to an electron gas [1, 3]. The electron band consists of equal numbers of up and down electrons in the absence of an applied magnetic field. As an external field is applied the up part of the band drops in energy while the down part decreases in energy causing a population transfer from down part to up part. Thus, a spin imbalance is created and a positive susceptibility is obtained of the form,

$$\chi \approx \mu_0 \mu_{\mathrm{B}}^2 g(E_{\mathrm{F}}), \tag{1.19}$$

where $E_{\mathrm{F}}$ is the Fermi energy and $g(E_{\mathrm{F}})$ is the density of states at the Fermi energy [1]. For the isotropic, spherical Fermi surface of the $3$-D electron gas this

reduces to

$$\chi \approx \frac{3n\mu_0\mu_{\mathrm{B}}^2}{2E_{\mathrm{F}}}, \tag{1.20}$$

though the density of states for other systems may be employed. Notably, this is only valid for low temperatures ($k_{\mathrm{B}} \ll E_{\mathrm{F}}$) where only electrons near the Fermi level can contribute. It is a small effect when compared to Eq. 1.16 as only the imbalance electrons of the electron band are involved whereas in a localised electron system each moment holding electron contributes. Again, this form of paramagnetism is temperature independent [1].

## 1.3 The Interaction of Magnetic Moments

As the temperature of a magnetic system containing some form of magnetic interaction between moments is lowered eventually thermal effects can become weaker than the energy scales of magnetic interaction. At this point it can enter a new magnetic phase characterised by these interactions that may show a form of magnetic order. An obvious candidate for this magnetic interaction is the dipole interaction between two magnetic moments:

$$E = \frac{\mu_0}{4\pi r^3}\left[\boldsymbol{\mu_1}\cdot\boldsymbol{\mu_2} - \frac{3}{r^2}(\boldsymbol{\mu_1}\cdot\boldsymbol{r})(\boldsymbol{\mu_2}\cdot\boldsymbol{r})\right], \tag{1.21}$$

where $\boldsymbol{r}$ is the position vector of $\boldsymbol{\mu_2}$ from $\boldsymbol{\mu_1}$ [1, 3, 5]. However, given that atomic moments are of the order of $\mu_{\mathrm{B}}$ and atomic separations are of the order of $1$ Å the energy of the classical dipole interaction is of the order of $1$ K. Thus, the dipole interaction cannot be responsible for any magnetic phases above a few kelvin and can be ignored in many cases [1, 5].

Instead quantum mechanics must be used to derive the interactions collectively known as exchange interactions. These interactions ultimately originate from the electrostatic interaction between electric charges, and are due to the requirement for Fermionic wavefunctions to be antisymmetric with respect to

the exchange of two electrons [1, 5, 6]. Using a two electron system as an example, the total wavefunction must be antisymmetric overall. This may be achieved by making the spatial part symmetric/antisymmetric ($\phi_{\mathrm{S}}/\phi_{\mathrm{AS}}$) and the spin part antisymmetric/symmetric ($\chi_{\mathrm{AS}}/\chi_{\mathrm{S}}$), recovering the familiar singlet,

$$\Psi_{\mathrm{Sing}} = \frac{1}{\sqrt{2}}[\psi_a(\boldsymbol{r}_1)\psi_b(\boldsymbol{r}_2) + \psi_a(\boldsymbol{r}_2)\psi_b(\boldsymbol{r}_1)]\chi_{\mathrm{AS}} = \phi_{\mathrm{S}}\chi_{\mathrm{AS}}, \tag{1.22}$$

and triplet,

$$\Psi_{\mathrm{Trip}} = \frac{1}{\sqrt{2}}[\psi_a(\boldsymbol{r}_1)\psi_b(\boldsymbol{r}_2) - \psi_a(\boldsymbol{r}_2)\psi_b(\boldsymbol{r}_1)]\chi_{\mathrm{S}} = \phi_{\mathrm{AS}}\chi_{\mathrm{S}}. \tag{1.23}$$

The spatial and spin parts of the overall wavefunction themselves are symmetric or antisymmetric combinations of the products of the single electron wavefunctions [1]. This is shown explicitly for the spatial part with single electron wavefunctions, $\psi$, in the above equations. The electrostatic energy for each state depends on only the spatial parts of the wavefunctions. However, the antisymmetry requirement of fermions means that the spatial part and therefore the energy is influenced by the spin part demonstrating how charge can influence magnetic moment alignment. For the two electron case, total spin, $S$, may be $1$ (triplet) or $0$ (singlet) and can be visualised as the spins being aligned or anti-aligned respectively. Thus, depending on which of $\phi_{\mathrm{AS}}$ and $\phi_{\mathrm{S}}$ are lower in energy the two spins (and therefore magnetic moments) may preferentially align or anti-align. There can be an energetic preference for ferromagnetic coupling between magnetic moments (alignment) or anitferromagnetic coupling (anti-alignment).

This interaction between two spins (or more generally two angular momenta) can be modelled in a Hamiltonian of the form,

$$\mathcal{H} = \mathcal{J}\boldsymbol{J_1} \cdot \boldsymbol{J_2}, \tag{1.24}$$

where $\mathcal{J}$ is known as the exchange strength or the exchange integral [1, 3–6].

In the two electron example this is equal to the energy difference between the triplet and singlet states, $\mathcal{J} = E_{\mathrm{Trip}} - E_{\mathrm{Sing}}$ [1, 6]. It is important to note that the exchange strength can be defined differently such that the prefactor of $\boldsymbol{J_1} \cdot \boldsymbol{J_2}$ is $-\mathcal{J}$ or $-2\mathcal{J}$ [1]. This means care must be taken when comparing quoted values. In the formalism used above, $\mathcal{J} > 0$ leads to antiferromagnetism being energetically favoured and $\mathcal{J} < 0$ leads to ferromagnetism. This interaction may be generalised to a $N$ electron system summing Eq. 1.24 for each unique electron pair,

$$\mathcal{H} = \sum_{i>j}^{N} \mathcal{J} \boldsymbol{J_i} \cdot \boldsymbol{J_j}. \tag{1.25}$$

While this may be the most full expression it is often simplified by assuming the exchange interaction for a given moment decreases with distance. In the forthcoming considered cases of exchange this is true (and is also true of the aforementioned dipole interaction). Therefore, only the closest magnet moments interact strongly (the nearest neighbours) with the interaction between more distant moments neglected or considered as a perturbation [1]. This allows the above sum to be drastically reduced to be over nearest neighbours only. It should be noted that the above depicts Heisenberg interactions between magnetic moments which may point in any direction in space. There also exists the XY model where moments are confined to the $xy$-plane and the Ising model where moments are confined to one direction (the $z$-axis) [1, 3, 6]. It is also worthwhile to note that $\mathcal{J}$ is typically non-trivial to calculate [1].

For the case of this thesis a number of exchange mechanisms are outlined below for the purpose of considering their strengths and signs. As this interaction involves individual electron wavefunctions combining it is clear that in a compound an important factor will be the degree of overlap between electron orbitals to form molecular orbitals [5]. Therefore a dependence on both spatial extent and orientation of the magnetic orbitals would be expected. This provides

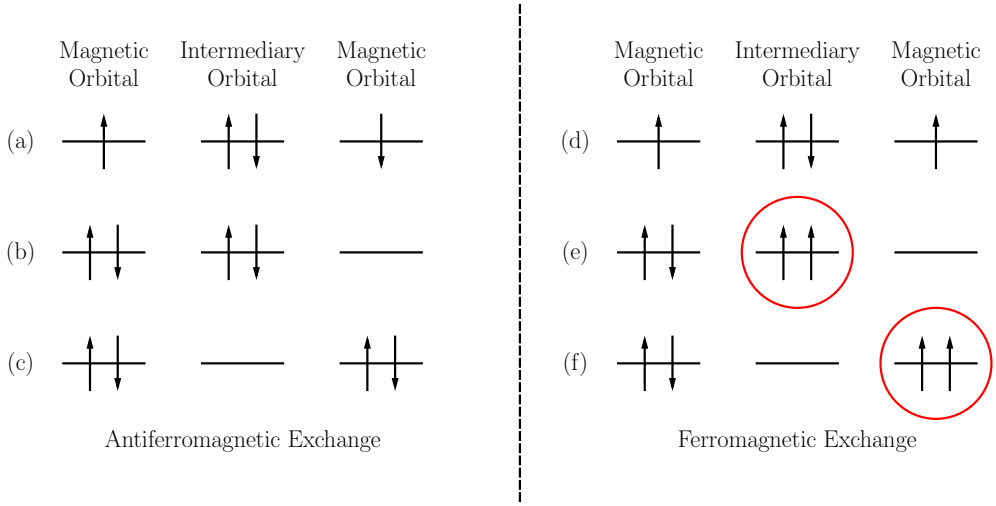



Figure 1.2: Basic example of the superexchange mechanism for antiferromagnetically coupled spins on the magnetic sites ((a), (b) and (c)) and ferromagnetically coupled spins ((d), (e) and (f)). (a) shows the antiferromagnetic ground state while (b) and (c) are excited states where electron hopping has taken place. (d) shows the ferromagnetic ground state while red circles in the excited states (e) and (f) indicate where hopping has resulted in the violation of the Pauli Exclusion Principle.

justification to the use of a nearest neighbour only Hamiltonian as more distant moments have less overlap and a weaker interaction. Therefore this suggests that a direct interaction between adjacent magnetic orbitals would be a clear culprit for magnetic interactions. However, this is an unsatisfactory explanation due to the requirement of good overlap of orbitals. Given that higher $L$ orbitals such as the $f$ orbitals of the lanthanides tend to be more contracted (resulting in worse orbital overlap) this suggests that direct exchange may be weak. An indirect exchange mechanism must be responsible for magnetic interactions leading to bulk order [1].

A common exchange mechanism in magnetic oxides and molecular magnets is known as superexchange [1, 3, 6]. Instead of via direct overlap between magnetic orbitals exchange proceeds through the non-magnetic, filled orbitals of an intermediary (a common example being the $p$ orbital of a bridging oxygen). The inclusion of an intermediary allows this form of communication to be longer ranged and it typically leads to antiferromagnetic interaction [1, 6]. Consider

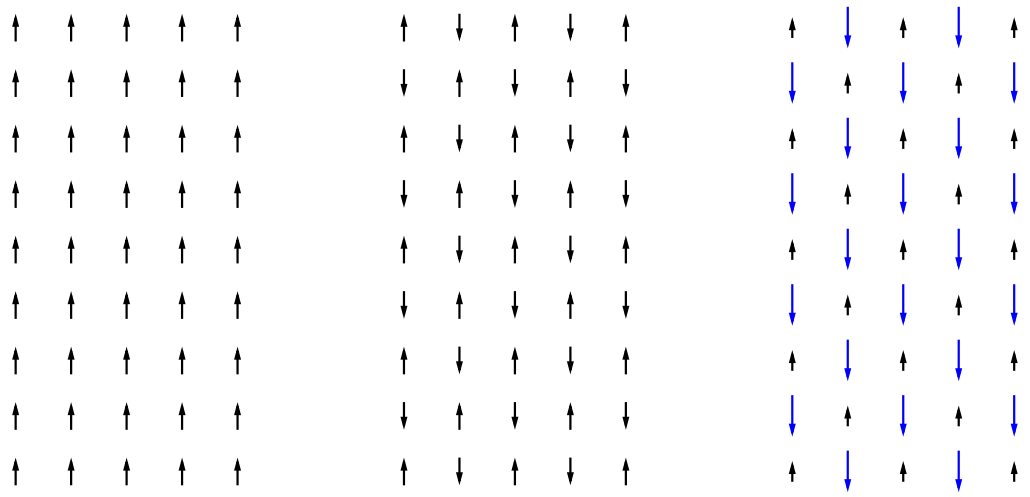
two singly occupied magnetic orbitals bridged by a fully occupied $p$ orbital. If the electrons can hop to and from the magnetic orbitals via the intermediary energy may be lowered [1, 6]. This is analogous to the energy of an electron trapped in a box when the size of the box is increased [1]. Since a hop does not flip the spin this simple example requires antiferromagnetic alignment between magnetic orbitals. This is illustrated in the left panel of Fig. 1.2 ((a)–(c)) where the possible excited state hopping is shown. For the considered example ferromagnetic coupling is also shown to violate Pauli's Exclusion Principle in the right panel of Fig. 1.2 ((d)–(f)). Superexchange can promote ferromagnetic interaction if the involved magnetic orbitals are different such as different $d$ orbitals of which only one of those involved in exchange is occupied [1]. It is therefore clear given the anisotropic nature of all but $s$ orbitals that an important factor affecting the strength of superexchange (and therefore $\mathcal{J}$) is the angle of the magnetic–intermediary–magnetic orbital bond [1].

Evidently as metals, featuring non-localised conduction electrons, can display magnetism there must be an alternative explanation to superexchange. This comes in the form of the RKKY interaction which has an exchange strength,

$$\mathcal{J}_{\mathrm{RKKY}} \propto \frac{\cos(2k_{\mathrm{F}}r)}{r^3}, \tag{1.26}$$

for a spherical Fermi surface where $k_{\mathrm{F}}$ is the Fermi wave number [1]. The origin of this interaction comes from a localised magnetic moment causing spin-polarisation of nearby conduction electron which in turn can polarise their nearest neighbours and so forth [1, 3]. An important feature of Eq. 1.26 is the inclusion of a cosine which causes $\mathcal{J}_{\mathrm{RKKY}}$ to oscillate between ferromagnetic and antiferromagnetic communication with distance.

Other forms of indirect exchange exist such as double exchange which utilises orbitals of magnetic atoms of different oxidation states and the Dzyaloshinky-Moriya interaction which involves the spin-orbit interaction [1, 3, 6]. However,



(a) Ferromagnetic Order (b) Antiferromagnetic Order (c) Ferrimagnetic Order

Figure 1.3: A 2-D square lattice populated by magnetic moments to demonstrate ferromagnetic order ((a)), antiferromagnet order ((b)) and ferrimagnetic order ((c)). Different sized arrows and colours for (c) indicate different magnetic moments of different magnitude.

understanding of superexchange and the RKKY interaction are satisfactory for considering the materials studied herein.

## 1.4 Order and Frustration

With magnetic interactions now allowed between moments cooperative behaviour can occur at low temperatures; magnetic order can be observed. This order can be ferromagnetic or antiferromagnetic in nature or indeed a mixture of the two leading to more exotic states.

Ferromagnetism occurs when exchange encourages magnetic moments to align. It can very easily be visualised as a regular array (a crystal lattice) of arrows representing magnetic moments. When moments order ferromagnetically, all the arrows point in the same direction as shown in Fig. 1.3(a) for a 2-D lattice. This suggests a spontaneous magnetisation when a compound enters the ferromagnetic state in the absence of an applied magnetic field [1].

In considering the susceptibility of a ferromagnet, the presence of interactions are taken into account by defining a molecular field which is a result of a moment's magnetic neighbours, $\boldsymbol{B}_{\mathrm{MF}} = \lambda \boldsymbol{M}$ [1, 6]. $\lambda$ is a constant parametrising

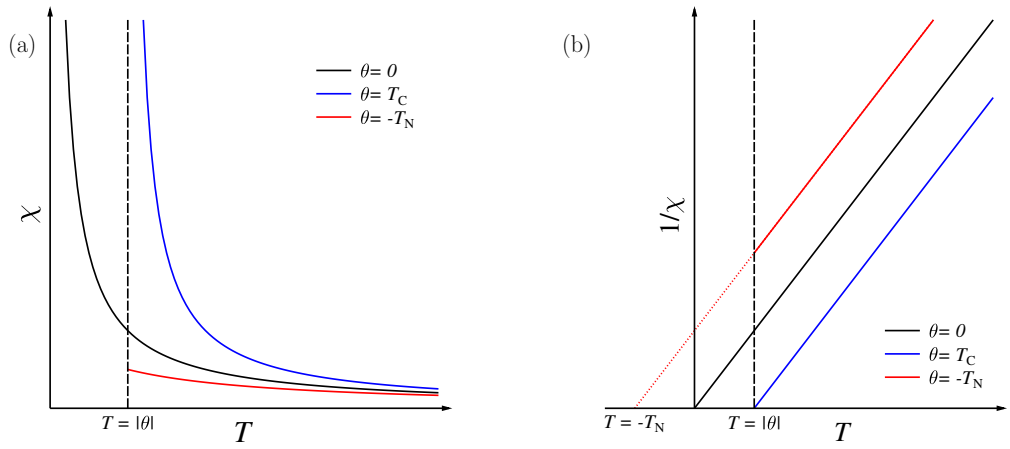



Figure 1.4: (a) The Curie-Weiss law demonstrated for paramagnets ($\theta = 0$), ferromagnets ($\theta = T_{\mathrm{C}}$) and antiferromagnets ($\theta = -T_{\mathrm{N}}$). Each corresponds to the same curve with the asymptote shifted to the appropriate value of $\theta$. $T_{\mathrm{C}} = T_{\mathrm{N}}$ for comparison. (b) The Curie-Weiss law plotted as $1/\chi$ vs. $T$ demonstrating that this obtains a linear plot with $x$-axis intercept at $T = \theta$.

the size of the molecular field assuming it is related to the sample magnetisation. It is positive for a ferromagnet and is related to the exchange integral [1, 6]. It is important to note this is a mean field approach which assumes each moment experiences the same molecular field and so does not perform well in the vicinity of the critical temperature ($T_{\mathrm{C}}$) of ferromagnetism due to the presence of fluctuations [1]. Nonetheless, this approach allows Curie's law to be altered to

$$\chi = \frac{C}{T - \theta}, \tag{1.27}$$

where $C$ is the Curie constant encompassing the various constants of Eq. 1.16 and $\theta$ is the Weiss temperature which is equal to the ferromagnet's critical temperature, $T_{\mathrm{C}}$ [1, 6]. This is the Curie-Weiss law and is specifically valid in the paramagnetic region of a material at high temperatures ($T > T_{\mathrm{C}}$). By looking at the form of this equation it is clear that this represents the ordinary Curie's law but with the asymptote moved from $T = 0$ K to $T_{\mathrm{C}}$ ($= \theta$), i.e. the curve has been shifted right. This is depicted in Fig. 1.4(a) and is replotted as $1/\chi$ vs. $T$ in Fig. 1.4(b).

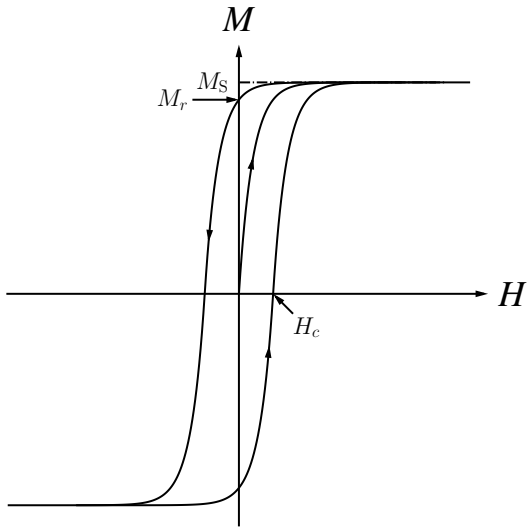



Figure 1.5: A pictorial representation of a magnetic hysteresis loop indicating both the remanent magnetisation, $M_r$, coercive field, $H_C$, and saturation magnetisation, $M_S$. Arrows on loop indicate the magnetic field sweep direction. Note only the initial up sweep starts with zero magnetisation at zero applied field. All subsequent sweeps follow the outer loops unless the sample is demagnetised by heating above $T_C$.

Many ferromagnets do not show a spontaneous magnetisation for $T < T_C$ due to the formation of domains, driven by the energetic cost of demagnetisation fields. Within each domain moments are ferromagnetically aligned but between domains their net magnetisations do not align [1, 6]. This yields an overall zero net magnetisation reducing demagnetising energy, although there is an energy cost for domain wall formation. Applying a magnetic field can restore a single domain state [1, 6].

Should a ferromagnet also contain anistropy with energetic preferences for moments to point in specific crystallographic directions it can also show a distinct response when the magnetic field is swept up and down known as a hysteresis loop [1]. This is so called because of the presence of hysteresis in $M$ between up and down sweeps of the magnetic field leading to the distinct features shown in Fig. 1.5 of a remanent magnetisation, $M_r$, and coercive field, $B_c$. The former is the non-zero magnetisation now found at zero applied magnetic field and the later the applied field required to reach zero magnetisation [1]. $M_r$ in zero field

is not the equilibrium state of the system and if left this will decay to the $M = 0$ state with multiple domains [6]. This hints at slow dynamics related to domain walls discussed in Chapter 3. The origin of this anisotropy can be found by considering the lattice of the specific ferromagnet.

Antiferromagnetism, due to the anti-alignment of neighbouring moments, is necessarily more complicated than ferromagnetism. A basic picture of antiferromagnetism is to consider the crystal lattice to be constructed of two, interpenetrating sublattices. Within each sublattice moments are ferromagnetically aligned but between them they are antiferromagnetically coupled resulting in no net magnetisation since all moments are equal [1, 6]. An example of this is shown in Fig. 1.3(b) on a $2$-D lattice. The susceptibility of an antiferromatically coupled system can also be solved considering a molecular field due to exchange between neighbouring moments though this retains the same problems as the molecular field approach for ferromagnets [1, 3, 6]. Here, $\lambda$ is again used to parameterise the molecular field but is negative for antiferromagnets. Helpfully, this leads to the Curie-Weiss law (Eq. 1.27) with $-\theta$ replaced by $T_{\mathrm{N}}$, the critical temperature for an antiferromagnetic transition called the Néel temperature [1]. Like the ferromagnetic case, this is simply Curie's law with the asymptote shifted to $T = -T_{\mathrm{N}}$. Since this is strictly valid for $T > T_{\mathrm{N}}$ the form of $\chi(T)$ below $T_{\mathrm{N}}$ differs with a dependence on the orientation of the applied field to the alignment axis [1, 6]. The high temperature ($T > T_{\mathrm{N}}$) form of the Curie-Weiss law for an antiferromagnet is shown in Fig. 1.4(a) and is contrasted with the ferromagnetic and paramagnetic case. Fig. 1.4(b) compares these systems for $1/\chi$ vs. $T$ demonstrating that each yields a straight line with an $x$-axis intercept (projected in the case of an antiferromagnet) at $T = \theta$.

Further complexity can be introduced when considering that for an antiferromagnetic state it simply requires an equal number of up and down moments in the system and this can be accomplished in several ways. The common type

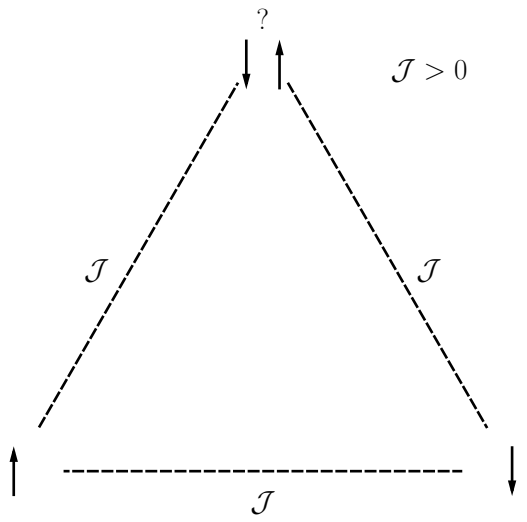



Figure 1.6: The classic example of frustration on a triangular lattice. An equal spin has been placed on each vertex with an equal antiferromagnetic exchange, $\mathcal{J}$, between each. The antiferromagnetic requirements between the lower magnetic moments have been satisfied but the upper moment is equally unsatisfied by an up or down orientation.

discussed here is known as type G order [1] though depending on the type of lattice it is possible that some ferromagnetic coupling is mixed in due to differences exchange strength.

Related to antiferromagnetism is ferrimagnetism. Also showing antiferromagnetic coupling between neighbouring moments, the simplest picture of ferrimagnetism is analogous to antiferromagnetism with two sublattices antiferromagnetically coupled but with unequal moments on each sublattice [1, 5, 6]. Normally, this can be assumed to be due to different magnetic ions on each sublattice but other variations can occur such as multiple types of magnetic ion occurring on each sublattice [6]. A simple schematic of ferrimagnetism is shown in Fig. 1.3(c). Due to each sublattice being different this can lead to a complicated temperature dependence and these compounds not following the Curie-Weiss law [1].

While other forms of order exist (see for example Ref. [1]) we instead con-

sider the case of competing exchanges and the problem of frustration. The classic example of magnetic frustration is the antiferromagnetic triangular lattice. This consists of an equilateral triangle with a magnetic site at each vertex. Between each site is an equal, antiferromagnet exchange. Clearly, exchange can be satisfied between two of the magnetic moments but the third has equal energy to point up or down. It is frustrated as shown in Fig. 1.6. A similar example of a frustrated lattice is the kagomé lattice [1, 7]. Interest in frustrated systems is due to the large number of unsatisfied states they may possess. This translates into a potential energy surface with no global minimum but many shallow and similar minima leading to metastability [7]. As such, frustrated systems can show hysteresis effects and slow magnetic relaxation [1]. A particular frustrated system of interest is spin glasses (which also feature randomness) but as the slow dynamic properties are the focus of this thesis the system is considered in detail in Chapter 3

## 1.5 Superconductivity

While this thesis focuses primarily on magnetism, superconductivity is considered in its a.c. response in Chapter 3 and as a feature coexisting with the magnetism of the $Li_xFe_{1-x}(OH)Fe_{1-y}Se$ family of compounds in Chapter 5. Thus, the basic concepts of this phenomenon are detailed (briefly) here.

Superconductors (or rather compounds with a superconducting phase) are typified by the property of zero electrical resistivity, $\rho = 0$ [8, 9]. This suggests an infinite conductivity, $\sigma$, and is clearly an attractive property for various practical applications [10, 11]. Above a critical temperature, $T_{\mathrm{C}}$, a superconductor is in the normal state with a finite resistivity. As temperature is lowered a phase transition occurs at $T_{\mathrm{C}}$ to the superconducting state with a sharp drop of $\rho$ to zero [8]. Therefore, testing a material for superconductivity appears to be a task for electrical transport. However, the determination of a zero resistivity is not

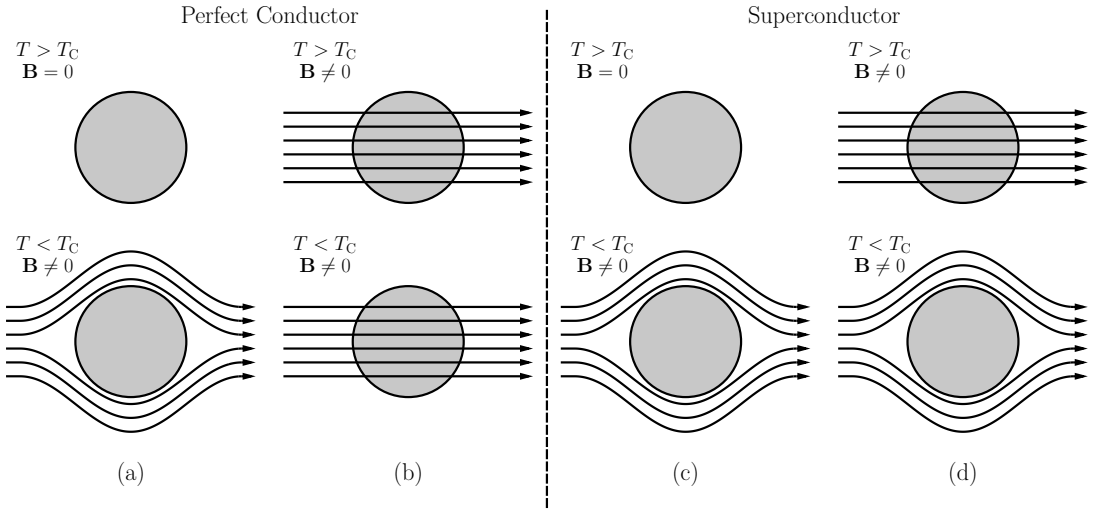



Figure 1.7: Illustration of cooling a perfect conductor below $T_C$ in the absence of an applied magnetic field followed by applying an external field ((a)) and performing the same procedure with an external field applied before cooling ((b)). Illustration of cooling a superconductor below $T_C$ in the absence of an applied magnetic field followed by applying an external field ((c)) and performing the same procedure with an external field applied before cooling ((d)). Both (c) and (d) result in the expulsion of magnetic flux known as the Meissner-Ochsenfeld effect.

necessarily a simple task [8].

Helpfully, superconductors show the further effect of the Meissner-Ochsenfeld effect (sometimes simply called the Meissner effect) [8, 9]. This is the observation that superconductors expel an applied magnetic field and contrasts with the behaviour of a system showing only $\rho = 0$ [8, 9]. Consider the case of a perfect conductor (defined with $\rho = 0$ below $T_C$) and superconductor above $T_C$ in the normal state. If no external magnetic field is applied, the systems cooled below $T_C$ and a field now applied both a perfect conductor and superconductor will not show any internal magnetic flux (see Figs. 1.7(a) and (c)). However, if the external field is applied first before cooling through $T_C$ the response of each system will now be different. The perfect conductor will continue to allow flux penetration as for the normal state (Fig. 1.7(b)) while the superconductor will expel the magnetic field so as to allow no flux penetration (Fig. 1.7(d)) [8, 9]. Thus a superconductor shows both perfect conductivity and perfect diamagnetism.

This perfect diamagnetism of superconductors may be expressed as a susceptibility of $\chi = -1$ (in SI units) signifying a complete opposition to the applied magnetic field. From the definition of susceptibility (Eq. 1.15) this means $M = -H$. As such, superconductors represent a unique class of materials with strong diamagnetism that certainly cannot be ignored. In fact, since susceptibility is a relatively easier property to measure compared to resistivity due to it being a contactless technique it is often used as evidence for a compound being a superconductor [8].

Strictly, susceptibility should only be measured in the limit of small measurement field. At larger magnetic fields the superconducting phase breaks down and the system is driven into the normal state. This may proceed in two ways splitting superconductors into type I and type II superconductors [8, 9]. Type I superconductors show a single critical field, $H_{\mathrm{c}}$, marking a sharp phase transition between superconducting and normal phases. Type II superconductors show two critical fields. For $H < H_{\mathrm{c1}}$ the system is superconducting, for $H_{\mathrm{c1}} < H < H_{\mathrm{c2}}$ the system is in a mixed state in which magnetic flux partially penetrates the sample and for $H_{\mathrm{c2}} < H$ the sample is in the normal state. In the mixed state, magnetic flux penetrates the sample in the form of vortices: small regions of circulating current surrounding a normal core through which flux lines travel [8]. Each vortex carries a single flux quantum [9] and is arranged in what is known as the Abrikosov flux lattice [8, 9].

The origin of superconductivity can be attributed to a pairing mechanism occurring between electrons resulting in Cooper Pairs [8, 9]. Via this mechanism, pairs can behave as bosons and condense into a ground state with a gap between ground state and excitations allowing the flow of current without scattering ($\rho = 0$) [8]. BCS theory can explain this pairing with electron-phonon interactions [8]. However, the high $T_{\mathrm{C}}$ superconductors do not obey BCS theory suggesting an alternative pairing mechanism not involving the lattice [8].

It is worthwhile to note that the transition from superconducting to normal state in type I superconductors may not be as sharp as implied for real samples. This is due to real samples having a physical shape. Thus they show demagnetising fields which originate from the divergence of magnetisation at the sample surface [1]. This field opposes the applied field defined by the equation,

$$\boldsymbol{H}_D = -N_{\mathrm{D}}\boldsymbol{M}, \tag{1.28}$$

where $N_{\mathrm{D}}$ is the demagnetising tensor. In general $N_{\mathrm{D}}$ can be diagonalised to show a demagnetising factor for each of the system's principal axes but is a complicated function of the sample shape except for special cases such as a sphere [1]. For superconductors this can actually cause a system to show $\chi < -1$ requiring adjustment for sample shape [8]. In type I superconductors the magnetic field at the lateral edges of the sample, $H_{\mathrm{e}}$, can be related to the applied field, $H$, by,

$$H_{\mathrm{e}} = \frac{H}{1 - N_{\mathrm{D}}}, \tag{1.29}$$

where $D$ is the demagnetisation factor [9]. Thus $H_{\mathrm{e}}$ may exceed $H_{\mathrm{c}}$ even if $H < H_{\mathrm{c}}$. This causes an intermediate state for $H_{\mathrm{C}}(1 - D) < H < H_{\mathrm{C}}$ in which the sample splits into lamina of superconducting and normal regions in contrast with the flux line penetration of type II superconductors [9].

# Chapter 2

# Non-magnetometry Techniques

## 2.1 Introduction

Various experimental techniques have been employed to characterise the magnetic properties of the materials detailed in this thesis. Particular focus has been placed on a.c. magnetometry (and necessarily d.c. magnetometry) and this will be the subject of Chapter 3. Herein other complementary techniques are discussed in terms of both basic theory of the technique and the practicalities of measurement.

## 2.2 Heat Capacity

Heat capacity or specific heat, $C$, is a very important property of a material. It may be defined simply by the equation

$$C = \lim_{\mathrm{d}T \to 0} \frac{\mathrm{d}U}{\mathrm{d}T}, \tag{2.1}$$

where $\mathrm{d}U$ is the change in internal energy of the system and $\mathrm{d}T$ is the associated temperature change [12, 13]. During a measurement, $\mathrm{d}U = \mathrm{d}Q$, which is the heat entering or exiting the system. It may be defined as $C_{\mathrm{V}}$, the heat capacity at constant volume, or $C_{\mathrm{P}}$, the heat capacity at constant pressure [14, 15]. The

latter of these has been measured in this thesis. Heat capacity essentially quantifies the capacity of a material to store thermal energy and it is related to the entropy of the system by the equation $S(T) = \int_0^T (C/T)\mathrm{d}T$. This shows that heat capacity can be very useful in monitoring phase transitions in which a change in entropy will occur.

Three properties of a material may contribute to the total heat capacity of a material: that of the lattice, that of itinerant electrons (should the system be metallic) and that of magnetism. Thus, in order to examine the magnetic contribution to the specific heat a strategy of measurement and modelling must be designed to eliminate non-magnetic contributions.

An ever present contribution to heat capacity is that of the crystal lattice (without which there is no crystal). Two models are typically used to explain the observed behaviour of the lattice. These historically arose due to a desire to explain why heat capacity followed the Dulong-Petit law at high temperatures (a constant of $C = 3Nk_\mathrm{B}$) but deviated at low temperatures to a $T^3$ law [14, 15]. Einstein's attempt to solve this considered each atom to be a quantum harmonic oscillator of energy $\hbar\omega_\mathrm{E}(n + 1/2)$ (where $\omega_\mathrm{E}$ is the Einstein frequency) yielding a heat capacity of

$$C = \frac{3N\hbar^2\omega_\mathrm{E}^2}{k_\mathrm{B}T}\frac{e^{\hbar\omega_\mathrm{E}/k_\mathrm{B}T}}{(e^{\hbar\omega_\mathrm{E}/k_\mathrm{B}T} - 1)^2}, \tag{2.2}$$

where $N$ is the number of atoms in the solid [14, 15]. While reducing to the required $3Nk_\mathrm{B}$ at high temperatures this does not reduce to the experimentally observed $T^3$ behaviour at low temperatures. To reproduce this low temperature behaviour collective vibrational modes of the crystal (phonons) must be considered. This approach yields the Debye model (not to be confused with the Debye model of a.c. techniques discussed in Chapter 3) with a heat capacity of

$$C = 9\frac{N}{V}k_\mathrm{B}\left(\frac{T}{\theta_\mathrm{D}}\right)^3\int_0^{\theta_\mathrm{D}/T}\frac{x^4e^x}{(e^x - 1)^2}\mathrm{d}x, \tag{2.3}$$

where $\theta_{\mathrm{D}} = \hbar\omega_{\mathrm{D}}/k_{\mathrm{B}}$ is the Debye temperature and $x = \hbar\omega/k_{\mathrm{B}}T$ [14–16]. This model assumes phonon dispersion to be linear up to a cut off value, $\omega_{\mathrm{D}}$ [14–16]. This is clearly an approximation with the greatest validity at low energies and temperatures. Furthermore, this can only approximate acoustic phonons; those whose frequencies go to zero at zero wavenumber ($k = 0$) [16]. Optical phonons which show a relatively constant, non-zero dispersion can be roughly approximated by the single frequency Einstein model. $\theta_{\mathrm{D}}$ sets the temperature scale with a $T^3$ term recovered at low temperature ($T \ll \theta_{\mathrm{D}}$) and the Dulong-Petit law recovered at high temperatures ($T \gg \theta_{\mathrm{D}}$) [14–16].

This treatment has dealt only with a lattice of atoms. If the system is metallic with conduction electrons these can also contribute to the heat capacity of the system. Indeed, use of the Sommerfeld model produces an electronic contribution at low temperatures to the heat capacity of the form

$$C_{\mathrm{elec}} = \frac{\pi^2 n}{2}\frac{k_{\mathrm{B}}^2 T}{E_{\mathrm{F}}}, \tag{2.4}$$

where $n$ is the number density of electrons and $E_{\mathrm{F}}$ is the Fermi energy [14–16]. Here, $E_{\mathrm{F}}$ sets the temperature scale with low temperature defined as $k_{\mathrm{B}}T \ll E_{\mathrm{F}}$. Helpfully, most metals fulfil this low temperature condition during experimental conditions ($T < 300$ K) owing to large Fermi energies [16].

Thus, the non-magnetic contribution to heat capacity is often initially fit to,

$$C = \gamma T + \beta T^3, \tag{2.5}$$

where $\gamma$ is known as the Sommerfeld coefficient and $\beta = (12/5)\pi^4 k_{\mathrm{B}}(N/V)(1/\theta_{\mathrm{D}}^3)$ is the Debye constant. If the system is insulating $\gamma = 0$ and only the $T^3$ term is required. Importantly, the above equation incorporates the low temperature expansion of the Debye model so may not always fit the studied system. This can prompt the inclusion of additional terms such as Einstein modes to account

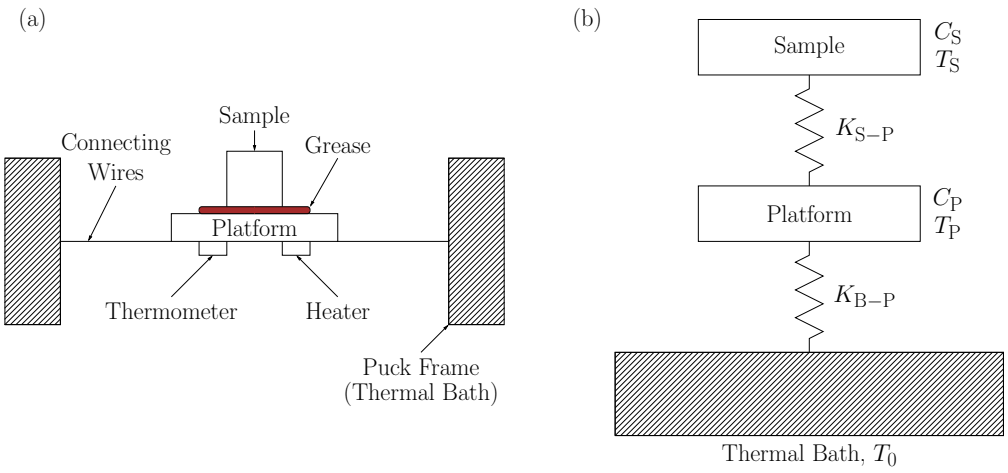



Figure 2.1: (a) Schematic of PPMS heat capacity puck for measurements. A cap is placed on the top half of this assembly for both protection and to act as a thermal shield. (b) Simplified representation of the thermal flow during thermal-relaxation calorimetry measurement in a PPMS.

for optical phonons [17].

Practical measurements of heat capacity detailed in this thesis were performed using a Quantum Design Physical Property Measurement System (PPMS). In addition to measuring the heat capacity of a solid in zero applied magnetic field this system was also capable of applying a steady d.c. magnetic field of up to $\mu_0 H_{\mathrm{d.c.}} = 14$ T. The system consists of a measurement platform with a thermometer and heater attached. The sample is placed on the platform with a thin layer of Apiezon-N grease (other greases can be used at high temperatures [18]) to both secure the sample and ensure good thermal contact. This is held at the centre of a PPMS puck by eight thermally conducting wires that function both as electrical contact to the platform heater and thermometer and as a well known thermal connection to the puck body. The puck body functions as a thermal bath. This set-up is depicted in Fig. 2.1(a). Thermal contact via exchange gas ($^4$He in a PPMS) is minimised during an experiment by measuring under high vacuum and a thermal shield partially covers the platform to prevent heating from sample space surfaces. This also helps physically protect the platform and wires from damage. A separate thermometer measures puck temperature. While

the measurement of samples detailed here remained below $100\ \mathrm{K}$ the PPMS is capable of measuring heat capacity over its whole accessible temperature range (2–$400\ \mathrm{K}$ [18]) though special consideration has to be given for $T > 200\ \mathrm{K}$ which will be briefly discussed later [19–21].

During measurements, the puck and sample are cooled or heated to some temperature, $T_0$, which is the bath/puck temperature, where it is held to ensure good stability. A known power ($P(t) = P_0$) is then applied to the heater increasing the platform (and sample) temperature to $T = T_0 + \Delta T$ after which the power is ceased ($P(t) = 0$) and the temperature is monitored as it relaxes back to $T = T_0$ [13, 22]. A factor affecting the increase and decay of temperature during this heating and cooling period is the thermal conductance of the wires connecting the puck frame (thermal bath) to platform, $K_{\mathrm{B-P}}$. Also important is the thermal conductance between platform and sample mediated by grease, $K_{\mathrm{S-P}}$, resulting in the two equations to describe the temperature of the platform and sample:

$$C_{\mathrm{P}}\frac{\mathrm{d}T_{\mathrm{P}}}{\mathrm{d}t} = P(t) - K_{\mathrm{B-P}}(T_{\mathrm{P}} - T_0) + K_{\mathrm{S-P}}(T_{\mathrm{S}} - T_{\mathrm{P}}) \tag{2.6}$$

and

$$C_{\mathrm{S}}\frac{\mathrm{d}T_{\mathrm{S}}}{\mathrm{d}t} = -K_{\mathrm{S-P}}(T_{\mathrm{P}} - T_{\mathrm{S}}), \tag{2.7}$$

where subscripts P and S refer to Platform and Sample respectively [13, 18, 22–24]. The thermal flow is shown graphically in Fig. 2.1(b). In ideal conditions, the platform and sample are in very good thermal contact ($K_{\mathrm{B-P}} \ll K_{\mathrm{S-P}}$) resulting in $T_{\mathrm{S}} \approxeq T_{\mathrm{P}}$ [13]. With $\Delta T = P(t)/K_{\mathrm{B-P}}$ (which allows $K_{\mathrm{B-P}}$ to be determined during heating) only one equation describing the heat capacity of the combined sample and platform system is required [13, 22, 24],

$$(C_{\mathrm{S}} + C_{\mathrm{P}})\frac{\mathrm{d}T_{\mathrm{P}}}{\mathrm{d}t} = -K_{\mathrm{B-P}}(T_{\mathrm{P}} - T_0) + P(t). \tag{2.8}$$

This results in a simple exponential decay for the cooling period,

$$T_{\mathrm{P}} = T_0 + \Delta T e^{-t/\tau}, \tag{2.9}$$

where $\tau = (C_{\mathrm{S}} + C_{\mathrm{P}})/K_{\mathrm{B-P}}$ [13, 22–25]. Thus, if $\Delta T$ is kept small enough such that thermal conductances and heat capacities remain constant then the heat capacity can be derived.

If $K_{\mathrm{B-P}}$ and $K_{\mathrm{S-P}}$ take similar values solving these equations is more difficult [24, 25]. The experimental cooling response becomes the sum of two exponential decays with more complicated relationships between the time constants $\tau_1$ and $\tau_2$ and sample and platform heat capacities [18, 22, 24]. Quantum Design software utilises a curve-fitting model to the single relaxation model and so called Two-Tau model to allow heat capacity to be extracted [13, 18, 23]. Importantly, Quantum Design software actually fits both the single relaxation time and Two-Tau Model for each measurement and determines the deviation from data for both selecting the best model for each measurement. Furthermore, several heating/cooling cycles can typically be performed for each measurement as well as repeats of that measurement to improve accuracy. A coupling constant, $100 \times K_{\mathrm{S-P}}/(K_{\mathrm{S-P}} + K_{\mathrm{B-P}})$, is also quoted for each measurement which describes the quality of the coupling of the sample to the platform [18].

Regardless of model used, a general background measurement of the heat capacity of the grease and platform is initially made called the addenda [18]. Since there is no sample only the single relaxation time model is required for fitting. This can then be subtracted during sample measurements to obtain sample-only heat capacity [18].

As stated, care needs to be taken for $T > 200$ K due to the Apiezon-N grease

used for thermal contact between platform and sample. The grease used for this purpose must have an extremely reproducible heat capacity for the temperature range for which it is used. Apiezon-N grease shows several anomalies for $200 \leq T \leq 300$ K so ideally a different grease must be used for higher temperatures [19–21].

## 2.3 $\mu$SR

The technique known as muon spin rotation or relaxation ($\mu$SR) utilises the $S = 1/2$ muon (specifically $\mu^+$) [1, 26, 27]. With a charge of $+e$ this particle clearly possesses a magnetic moment which (due to its mass of $207m_\mathrm{e}$) is intermediate between $\mu_\mathrm{B}$ and $\mu_\mathrm{N}$ [1, 26, 27]. This may interact with the magnetic moments of matter. Being positively charged means it is also attracted to areas of high electron density bringing it into the vicinity of the magnetic moment carrying electrons. The usefulness of the $\mu^+$ particle comes from its short lifetime ($\tau_\mu = 2.2$ $\mu$s) and the fact one of its decay products is a positron [1, 26, 27],

$$\mu^+ \rightarrow e^+ + \nu_e + \bar{\nu}_\mu.$$

Importantly, the produced positron has a tendency to be emitted parallel to the parent muon's spin [1, 26]. This angular distribution is shown for the most highly energetic positrons in Fig. 2.2(a). Thus, if enough muons are planted into a sample and the emitted positron direction analysed statistically this yields a method of determining the muon's spin immediately prior to decaying. Additionally, muons are implanted uniformly in a sample meaning any detected response will be proportional to the volume fraction that corresponds to that magnetic feature with no spatial information being obtained [1].

Now consider the case where there is some uniform internal field (such as a single domain ferromagnetic) or an applied external field. Assuming the muon's spin is initially anti-parallel to its momentum and the magnetic field perpendic-

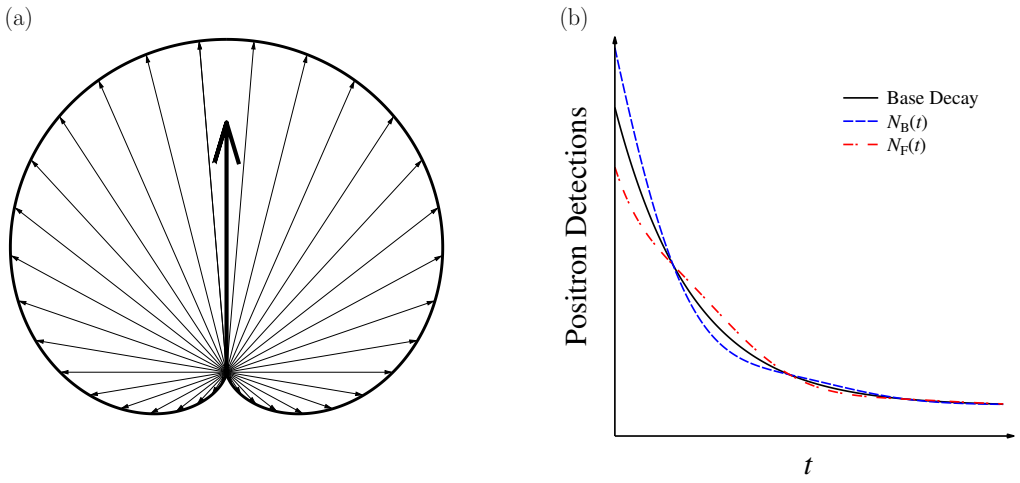



Figure 2.2: (a) Angular distribution of most highly energetic emitted positrons based on initial muon spin direction (up here) from Ref. [1]. (b) Idealised number of positron detections in forward and backward detectors, $N_{\mathrm{F}}(t)$ and $N_{\mathrm{B}}(t)$, as well as the base, non-oscillating decay.

ular to this, upon entering the sample and experiencing the magnetic field the muon's spin will undergo Larmor precession [1, 26, 27]. If it decays immediately the emitted positron is more likely to be detected in a rear detector (number of detections defined as $N_{\mathrm{B}}(t)$) and if it survives long enough to execute a $\pi$ rotation the positron is more likely to be detected in a forward detector (number of detections defined as $N_{\mathrm{F}}(t)$). Both $N_{\mathrm{B}}(t)$ and $N_{\mathrm{F}}(t)$ should be a sum of an exponential decay ($\exp(-t/\tau_\mu)$) and a sinusoidal oscillation (with $\pi$ phase difference between $N_{\mathrm{F}}(t)$ and $N_{\mathrm{B}}(t)$) as is shown in Fig. 2.2(b). Thus, the oscillatory part can be extracted using the asymmetry function,

$$A(t) = \frac{N_{\mathrm{B}}(t) - N_{\mathrm{F}}(t)}{N_{\mathrm{B}}(t) + N_{\mathrm{F}}(t)}, \tag{2.10}$$

allowing the frequency of muon precession to be determined [1, 26, 27]. The angular frequency of Larmor precession is $\omega_\mu = \gamma_\mu B$ where the gyromagnetic ratio of the muon is $\gamma_\mu = g_e/2m_\mu$ [1, 26, 27]. This allows the magnetic field, $B$, to be calculated demonstrating the muon's ability to act as a tiny magnetometer. Furthermore, with the intermediate mass of the muon it is sensitive enough to

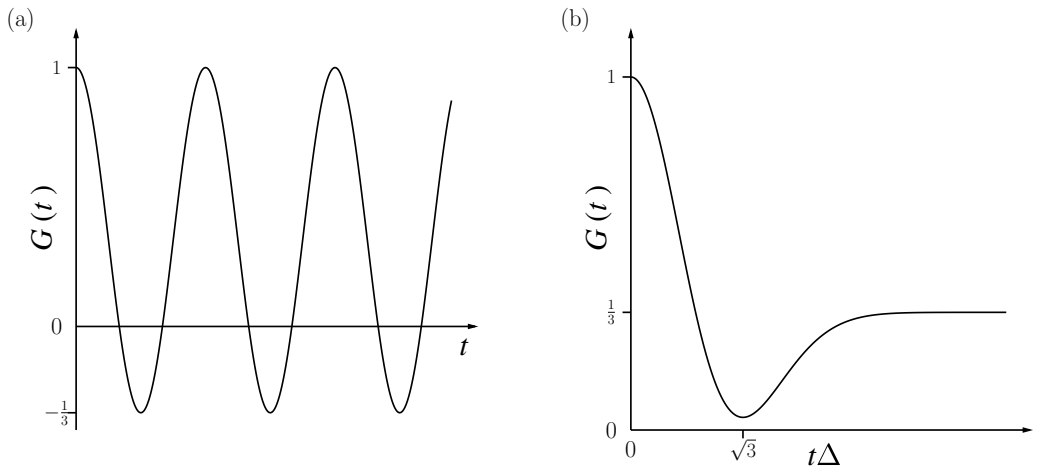



Figure 2.3: (a) Normalised asymmetry for a $\mu$SR experiment following Eq. 2.12 in which the muon encounters differently orientated magnetic fields of the same value, $B$. (b) Normalised asymmetry following the Kubo-Toyabe function (Eq. 2.13) assuming the field distribution the muon encounters is Gaussian. Important features are marked.

detect a magnetic field of as small as $\sim 10^{-5}$ T [26]. As a result, it is sometimes necessary for magnets to be used to null the Earth's magnetic field in order for a true zero field experiment to be performed [1].

$\mu$SR may also be applied to study systems with random or very short range order and dynamic moments. In these cases, there may be many different muon sites with different local magnetic fields and field orientations. First consider the zero applied field case in which each muon encounters a differently orientated internal magnetic field, the situation of random fields in the studied system or a polycrystalline sample with differently orientated grains. The normalised decay asymmetry, $G(t)$, with angle $\theta$ between spin and magnetic field is

$$G(t) = \cos^2\theta + \sin^2\theta\cos(\gamma_\mu B t), \tag{2.11}$$

which averaged across all directions assuming no preferential direction yields [26, 27]

$$G(t) = \frac{1}{3} + \frac{2}{3}\cos(\gamma_\mu B t). \tag{2.12}$$

An oscillatory part remains (as shown in Fig. 2.3(a)) indicating the presence of magnetic order in the system since the muons experience random orientations of the static internal field. Thus, a simple question to ask in $\mu$SR experiments is, "Are there wiggles in the asymmetry?" If instead the field (while static) is not uniform and represented by a Gaussian distribution of width $\Delta/\gamma_\mu$ centred at zero then the normalised asymmetry yields [26, 27],

$$G(t) = \frac{1}{3} + \frac{2}{3}e^{-\Delta^2 t^2/2}(1 - \Delta^2 t^2). \tag{2.13}$$

Essentially, different encountered internal fields result in the superposition of different frequency oscillations yielding an asymmetry with no oscillatory part [26]. Instead, the above result of Kubo and Toyabe shows a distinctive dip at $t = \sqrt{3}/\Delta$ and at long times tends to $1/3$ [26, 27]. This is shown in Fig. 2.3(b) with both these features indicated.

This assumes that the magnetic field is constant for the muon's lifetime. Let a dynamic system be described by correlation frequency, $\nu_\mathrm{c}$. The rough range of $\nu_\mathrm{c}$ that muons can probe is $\sim 10^5 - 10^{12}$ Hz (though this is system dependent as it relies on the interaction between muon and magnetic field so is very much a rule of thumb) [27]. Firstly, consider the regime $\nu_\mathrm{c} t \ll 1$. Here, the fluctuations of magnetic moments (and therefore internal magnetic fields) is very slow on the scale of the muon's lifetime such that each muon experiences an essentially static magnetic field. Thus, these 'slow' fluctuating magnetic moments in a $\mu$SR experiment would obtain the above Kubo-Toyabe function (Eq. 2.13) [27]. At the other extreme where $\nu_\mathrm{c} t \gg 1$ (the motional-narrowing limit) the muon experiences many different local fields before it decays. In order to model this, the muon can be considered to be hopping between different muon sites with

different local fields at each site corresponding to the possible fluctuations. The muon hopping rate is $\nu_{\mathrm{c}}$. This yields an exponentially decaying asymmetry,

$$G(t) = e^{-\lambda t}, \tag{2.14}$$

where $\lambda = 2\Delta^2/\nu_{\mathrm{c}}$ [27]. Clearly, no oscillations can be observed nor the dip and distinct $1/3$ tail of Eq. 2.13. For intermediate correlation frequencies it can be expected for Eq. 2.13 to morph to Eq. 2.14 as frequency is increased [26].

In the case of slow muon hopping (or low correlation frequency) an important effect is a change in the $1/3$ tail of the zero-field Kubo-Toyabe function. As $\nu_{\mathrm{c}}$ increases from zero but remains very small a pronounced depression in the long time value of the tail is observed, providing a way of examining slow dynamics [26].

Muon experiments may also be performed in an applied magnetic field typically referred to as the transverse field (when the field is perpendicular to the initial muon spin direction) and longitudinal field (when the field is applied parallel to the initial muon spin). The transverse field alignment has somewhat fallen out of favour due to the utility of the longitudinal alignment [28]. It may still be employed in the measurement of frequency shifts, phase separation in magnetic systems and investigating field distributions [28]. Longitudinal fields offer an interesting opportunity in that they may help to differentiate from a distribution of static internal fields as described or fluctuating internal fields [26]. For randomly orientated static fields the external field, $H_0$, causes the muons to precess around both internal and external fields enhancing the $1/3$ tail of the zero-field Kubo-Toyabe function to greater values [26]. In very large $H_0$ this actually overpowers any internal fields and prevents reorientation of the muon spin such that the asymmetry function is held near unity [26]. For fluctuating moments a longitudinal magnetic field shows a smaller effect, causing the exponential relaxation to slow down ($\lambda$ decreases) [29].

Finally, a brief note is made of the production of muons for $\mu$SR experiments and a limit on time resolution. While muons may be detected from cosmic rays this does not provide anywhere near the appropriate flux for a practical measurement [1, 26]. Utilising a synchrotron or cyclotron, high energy proton beams can be fired into a target to produce pions

$$p + p \rightarrow \pi^+ + p + n,$$

which may subsequently decay into muons and muon-neutrinos [1, 26],

$$\pi^+ \rightarrow \mu^+ + \nu_\mu.$$

Usefully, the neutrino must have its spin antiparallel to its momentum [1, 26]. Thus, if the $\pi^+$ is prepared at rest the $\mu^+$ and $\nu_\mu$ must have equal and opposite momentum and due to the properties of the neutrino so too must their spin [1, 26]. This allows spin polarised $\mu^+$ beams to be produced.

During an experiment it is clearly important to record the time between a muon implanting in the sample and the detection of the resultant positron. In the continuous wave set up, only one $\mu^+$ is allowed to enter the sample at a time to prevent the overlap of time windows and ambiguity to the parent $\mu^+$ of a detected positron [26]. This may be achieved with a low muon arrival rate or a deflector to effectively lock off the sample until a muon has decayed [26]. Alternatively, a large number of $\mu^+$ may be implanted in the sample at the same time via a pulsed muon beam [26]. Thus, only the pulse arrival time needs to be recorded and each positron detection measured relative to this. While this allows a greater rate of measurements this does have a disadvantage of decreasing the time resolution of the experiment due to the finite time width of the muon pulse [26]. Therefore, a pulsed muon beam is not ideal should very fast relaxation be under study.

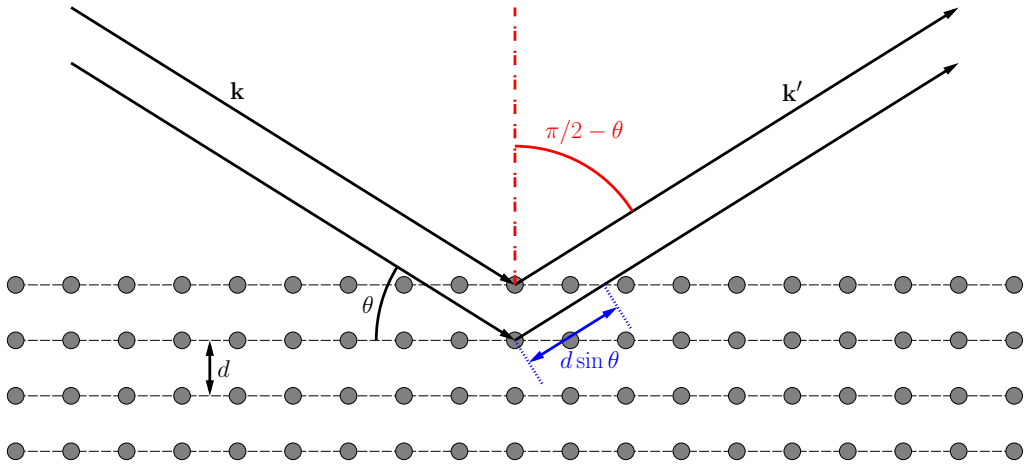



Figure 2.4: Bragg scattering from planes in a crystal. Incident radiation or particles arrive with wavevector $\boldsymbol{k}$ and after scattering leave with wavevector $\boldsymbol{k}'$. Both $\boldsymbol{k}$ and $\boldsymbol{k}'$ make an angle $\pi/2-\theta$ with the plane normal. Interplane distance is $d$ and the path difference between particles or radiation scattering of adjacent layers is $d\sin\theta$.

An issue that may complicate $\mu$SR is the question of the muon stopping site. Several of these may exist requiring complex data analysis to extract key physics. In addition, it can be asked if the muon (which enters the sample with a large energy of $\sim 4\,\mathrm{MeV}$) is only measuring regions of a sample it has damaged during its slowing down process. However, due to the there being a threshold energy for vacancy production, only the initial part of the muon's path in the sample will be damaged [26]. Thus, the muon is still able to propagate further into the sample (assumed to be $\sim 1\ \mu\mathrm{m}$) and decay in (and measure) an undamaged region [26].

## 2.4 Scattering

While scattering measurements are not presented in this thesis, the materials which I will describe in subsequent chapters have typically been characterised by a scattering technique. Thus, this section aims to briefly show the basics of scattering so that the origin of these results can be understood. A much more complete introduction to scattering can be found in Ref. [14].

A useful starting point is Bragg's Law of diffraction. This assumes radiation or particles with wavevector $\boldsymbol{k}$ incident on a plane constructed of a regular array of atoms with distance, $d$, between planes can scatter with constructive interference governed by

$$2d\sin\theta = n\lambda. \tag{2.15}$$

Here $\lambda$ is the wavelength of the incident radiation or particle, $n$ is the order of diffraction and $\frac{\pi}{2} - \theta$ is the angle between the plane normal and incidence (Fig. 2.4) [14]. This equation makes clear that by scanning over a sample all possible interplane distances can be extracted allowing the microscopic structure of the investigated system to be derived. This produces a diffraction pattern with a series of peaks known as Bragg peaks [1, 14]. If the sample is a powder the obtained pattern is considerably simpler due to the random orientation of grains [14]. A single crystal diffraction pattern is more complicated due to the greater amount of information obtained from the ability to change crystal orientation.

While Eq. 2.15 quantifies when constructive interference (and therefore a diffraction pattern) will be obtained, it does not explain the intensities of such a pattern nor why scattering occurs. For this a short foray into the crystal and reciprocal lattice is required.

A crystalline solid can be described structurally as a combination of a lattice and basis. The lattice is an infinite set of regular points in space all separated by an integer sum of linearly independent primitive lattice vectors [14, 16]. This allows a translation vector, $\boldsymbol{T}$, to be defined as

$$\boldsymbol{T} = n_1\boldsymbol{a}_1 + n_2\boldsymbol{a}_2 + n_3\boldsymbol{a}_3, \tag{2.16}$$

where $n_i$ are any integers and $\boldsymbol{a}_i$ are the primitive lattice vectors. This means if any point $\boldsymbol{r}$ on the lattice is changed to $\boldsymbol{r} + \boldsymbol{T}$ an identical point has been

reached. Mathematically this means that points $\boldsymbol{r}$ and $\boldsymbol{r}'$ are identical if $\boldsymbol{r} = \boldsymbol{r}' + \boldsymbol{T}$ and is true of any property of the lattice that depends on position (such as electrostatic potential energy) [16]. The basis is the atom or collection of atoms that when coupled with the lattice forms the crystal structure [16]. The unit cell can be defined as a unit of space that can be repeated to recreate the crystal structure [14, 16]. For a given crystal many different unit cells can be defined with those containing the minimum volume (and so one lattice point) known as the primitive unit cell [14, 16].

Just as the crystal lattice is spanned by primitive lattice vectors, the $k$ space reciprocal lattice is spanned by primitive reciprocal lattice vectors, $\boldsymbol{b}_j$, allowing a definition of the general reciprocal lattice vector to describe a point on the reciprocal lattice

$$\boldsymbol{G} = m_1\boldsymbol{b}_1 + m_2\boldsymbol{b}_2 + m_3\boldsymbol{b}_3, \tag{2.17}$$

where $m_j$ are integers [14]. This ensures the relation

$$\exp\{i\boldsymbol{G}\cdot\boldsymbol{T}\} = 1 \tag{2.18}$$

holds when the lattice vectors obey $\boldsymbol{a}_i \cdot \boldsymbol{b}_j = 2\pi\delta_{ij}$, where $\delta_{ij}$ is the Kronecker delta [14, 16]. The reciprocal lattice is in fact the Fourier transform of the real space lattice with the $k$ space version of the unit cell being the Brillouin zone [14, 16]. The first Brillouin zone (surrounding a lattice point at its origin) is defined such that it encompasses any $\boldsymbol{k}$ that lies closer to this first lattice point than the next nearest [14]. Furthermore, it retains the same periodic property as the real space lattice that the wavevector is unchanged by the reciprocal lattice vector, $\boldsymbol{k} = \boldsymbol{k}' + \boldsymbol{G}$ [14, 16]. The use of the Brillouin zone is very important for various phenomena in addition to scattering such as band theory [14, 16].

A final point to make in regards to the reciprocal lattice is that the vector $\boldsymbol{G}$

may define the distance between lattice planes. This is accomplished using Miller indices $h$, $k$ and $l$ [14, 16]. A lattice plane may be defined by these indices based on where it cuts the real space lattice vectors, $\boldsymbol{a}_1/h$, $\boldsymbol{a}_2/k$ and $\boldsymbol{a}_3/l$ normally written as $(hkl)$ with reciprocal lattice vector $\boldsymbol{G} = h\boldsymbol{b}_1 + k\boldsymbol{b}_2 + l\boldsymbol{b}_3$ [14, 16]. This is an extremely useful result since the interplane distance, $d_{hkl}$, is directly related to this reciprocal lattice vector [14],

$$d_{hkl} = \frac{2\pi}{|\boldsymbol{G}|}. \tag{2.19}$$

This can be used to help derive the crystal structure from a diffraction pattern.

Returning to the problem of scattering in crystals incident radiation or particles scattering off a crystalline sample can be stated as a change in wavevector after exiting the sample, $\boldsymbol{k} \neq \boldsymbol{k}'$, where the prime indicates the exiting radiation or particle wavevector. Fermi's golden rule may be used to find the transition rate from state $\boldsymbol{k}$ to $\boldsymbol{k}'$ [14],

$$\Gamma(\boldsymbol{k}', \boldsymbol{k}) = \frac{2\pi}{\hbar} |\, \langle \boldsymbol{k}'|V|\boldsymbol{k}\rangle \,|^2 \delta(E_{\boldsymbol{k}'} - E_{\boldsymbol{k}}), \tag{2.20}$$

where $V(\boldsymbol{r})$ is the periodic potential in the sample. The delta function encodes the requirement of conservation of energy on scattering (i.e. $|\boldsymbol{k}| = |\boldsymbol{k}'|$ and scattering is elastic). The matrix element is the quantity of interest defined as

$$\begin{aligned}\langle \boldsymbol{k}'|V|\boldsymbol{k}\rangle &= \int \mathbf{d}\boldsymbol{r} \frac{\exp\{-i\boldsymbol{k}'\cdot\boldsymbol{r}\}}{\sqrt{L^3}} V(\boldsymbol{r}) \frac{\exp\{i\boldsymbol{k}\cdot\boldsymbol{r}\}}{\sqrt{L^3}} \\ &= \frac{1}{L^3}\int \mathbf{d}\boldsymbol{r} \exp\{-i(\boldsymbol{k}'-\boldsymbol{k})\cdot\boldsymbol{r}\} V(\boldsymbol{r}).\end{aligned} \tag{2.21}$$

Here $L$ is the linear size of the crystal and $1/L^3$ serves as a normalisation factor [14]. Now the periodic nature of the potential (and lattice) may be used by defining $\boldsymbol{r}$ to be some point in the unit cell and $\boldsymbol{r}'$ that point translated by the

translation vector, $\boldsymbol{r} = \boldsymbol{r}' + \boldsymbol{T}$. Thus the integration may be broken into a sum of integrations for each possible $\boldsymbol{T}$ over only the unit cell. Since the potential is periodic this also means $V(\boldsymbol{r}) = V(\boldsymbol{r}' + \boldsymbol{T}) = V(\boldsymbol{r}')$ and yields

$$\begin{aligned}\langle \boldsymbol{k}'|V|\boldsymbol{k}\rangle &= \frac{1}{L^3}\sum_{\boldsymbol{T}}\int_{\text{unit cell}} \mathbf{d}\boldsymbol{r}' \exp\{-i(\boldsymbol{k}'-\boldsymbol{k})\cdot(\boldsymbol{r}'+\boldsymbol{T})\}V(\boldsymbol{r}'+\boldsymbol{T}) \\ &= \frac{1}{L^3}\left[\sum_{\boldsymbol{T}}\exp\{-i(\boldsymbol{k}'-\boldsymbol{k})\cdot\boldsymbol{T}\}\right]\left[\int_{\text{unit cell}} \mathbf{d}\boldsymbol{r}' \exp\{-i(\boldsymbol{k}'-\boldsymbol{k})\cdot(\boldsymbol{r}')\}V(\boldsymbol{r}')\right].\end{aligned} \tag{2.22}$$

The left term in brackets is zero unless $\boldsymbol{k}' - \boldsymbol{k} = \boldsymbol{G}$ due to Eq. 2.18. This is known as the Laue condition and is equivalent to Bragg's law [14].

The right term in brackets of the above equation is called the structure factor,

$$S(\boldsymbol{G}) = \int_{\text{unit cell}} \mathbf{d}\boldsymbol{r}' \exp\{i\boldsymbol{G}\cdot\boldsymbol{r}'\}V(\boldsymbol{r}'), \tag{2.23}$$

which is proportional to the square root of scattering intensity, $\sqrt{I}$ [14]. Thus, this controls the strength of scattering and has different dependences for different types of scattering.

For neutron scattering, the incident neutrons scatter primarily from nuclei resulting in the scattering potential of Eq. 2.23 depending upon the atomic form factor [14]. This is proportional to the nuclear scattering length, $b_j$, and is atom dependent, depending in a complex way on the particular configuration of the nucleus [1, 14].

X-rays scatter from electrons and therefore the appropriate scattering potential is the electron density [14]. Therefore the form factor of electrons is roughly proportional to atomic number Z (i.e. number of electrons in an atom), with high Z atoms scattering more strongly than low Z atoms [14]. This means that x-ray scattering has difficulty detecting hydrogen or differentiating between atoms

with similar electron densities [14]

A final note on scattering relates to the fact that neutrons possess a magnetic moment (despite lacking a charge). This is due to the three moment possessing quarks that constitute a neutron [30]. With a magnetic moment, neutrons can scatter from the magnetic moments in a crystal. However, given the treatment of this section it is clear that Bragg peaks (due to magnetism) will only exist if those moments are periodic in their orientation [1, 14]. This means that neutrons can detect long range magnetic order such as ferromagnetism or antiferromagnetism but will have difficulty resolving magnetic states for which moments are ordered only over short range [1, 14]. Furthermore, when neutron scattering can detect magnetic order it can also elucidate the type of magnetic structure (such as the type of antiferromagnetic order) [1].

# Chapter 3

# D.C. and A.C. Magnetometry

## 3.1 Introduction

The measurement of d.c. magnetic susceptibility is commonly used to characterise a newly discovered magnetic material in addition to x-ray scattering to derive crystal structure. Such a measurement can allow the elucidation of various magnetic properties of materials such as the presence of a phase transition, the magnetic moment of a material or simply the sign of magnetic exchange as discussed in Sections 1.2 and 1.4 [1]. However, implicit in the discussion up to this point has been the assumption that the sample properties remain effectively static, so that there is no measurable dynamic response. This assumption can be restated in terms of the dynamics being much faster, or slower, than the experimental timescale. While this assumption holds in many cases, there are many classes of material where it does not. In such cases, much useful information can be gained by employing a.c. magnetic susceptibility, a technique which utilises a periodic magnetic field rather than a static d.c. magnetic field. A.c. magnetic susceptibility has found application in various areas such as molecular magnetism [31, 32], ferromagnetism [33] and superconductivity [34, 35] and may be used to help differentiate between different types of slow relaxation [31, 36, 37] and derive energy barriers for that relaxation [31–33].

This chapter aims to review the practical measurement of magnetometry but primarily highlights the technique of a.c. magnetometery. It forms the bulk of a review paper co-authored with S. J. Blundell [38] which has been accepted for publication in *J. Phys. Condens. Matter*. A theoretical approach to modelling data is adopted before introducing various classes of material and discussing their a.c. response.

## 3.2 D.C. Magnetic Susceptibility

Magnetic susceptibility was previously defined by Eq. 1.15 assuming a linear relationship between $M$ and $H$. Strictly, this should be in the limit of vanishing $H$ to ensure such a relationship holds. It can be defined as a differential susceptibility

$$\chi = \frac{\partial M}{\partial H}. \tag{3.1}$$

Given that typically $\chi \ll 1$ Eq. 1.14 reduces to $B \simeq \mu_0 H$ and this allows susceptibility to be defined as

$$\chi \simeq \lim_{B \to 0} \frac{\mu_0 M}{B}. \tag{3.2}$$

These equations apply to both d.c. and a.c magnetic susceptibility. However, in a real experiment it is not possible to apply a vanishing field. The measured signal is proportional to a finite applied field. Thus a real experiment measures

$$\chi_{\text{exp}} = \frac{\delta M}{\delta H} \simeq \mu_0 \frac{\delta M}{\delta B}, \tag{3.3}$$

where $\delta B = \mu_0 \delta H$ is a finite applied magnetic field. For a d.c. measurement, $\delta B$ is a small, static d.c. magnetic field and the resulting magnetisation $\delta M$ is recorded. A simplistic view of $\chi$ may identify it as the near zero applied magnetic field gradient of the $M$ versus $H$ curve, although this may not be strictly true in non-paramagnetic systems such as ferromagnets.

In a real d.c. susceptibility measurement the magnetisation of a sample is

measured as a function of temperature on warming twice. Initially, the sample is cooled in zero applied magnetic field to the minimum measurement temperature before applying the measurement field ($\delta B$) and measuring while temperature is increased. This is the zero field cooled (ZFC) sweep and corresponds to the system taken out of steady state conditions. Following this, the sample is cooled in the measurement field ($\delta B$) and the warming measurement repeated. This yields the field cooled (FC) sweep and corresponds to the system in the steady state. Thus, measurement of FC and ZFC sweeps can give an indication of the presence of slow magnetic relaxation, but the relevant timescale that is being probed depends on the rate at which both the magnet can be swept and a measurement can be made.

D.c. magnetic measurements made in this thesis were performed using a Quantum Design Magnetic Property Measurement System (MPMS). This allowed measurements in the range $1.8 \leq T \leq 300$ K and in applied magnetic fields up to $\mu_0 H_{\mathrm{d.c.}} = 7$ T. The samples (powders in this thesis) were placed inside gelatin capsules which were fixed inside drinking straws. These were attached to the end of a brass rod which was inserted into the MPMS. A motor allowed the sample to be moved in and out of a detector.

Magnetometers work on the basis of a voltage induced in a detection coil due to a changing magnetic flux (Faraday's law) [1]. Thus $V \propto \mathrm{d}M/\mathrm{d}t$. The method of achieving this changing flux varies between magnetometers [1] with the MPMS physically moving the sample through three sets of detector coils [39]. These consist of a pair of central coils with oppositely wound coils above and below [39]. This results in a distinct voltage response of the assembly when the sample completes a full translation through all coil sets resembling a $\sin(x)/x$ function. Great sensitivity is achieved in the MPMS through the use of superconducting quantum interference devices (SQUIDs) [39]. This is a superconducting ring containing two Josephson junctions that acts as a quantum interferometer

[1, 8]. This is coupled inductively to the circuit containing the detection coils in a MPMS [39] and allows very sensitive measurements to be made [1, 8].

## 3.3 A.C. Magnetic Susceptibility

In a.c. magnetic susceptibility, a time varying, sinusoidal magnetic field ($H_{\mathrm{a.c.}}$) is applied to the system. Simultaneously, a static, d.c. magnetic field ($H_{\mathrm{d.c.}}$) may also be applied. Thus the field $H$ inside the sample is given by

$$H = H_{\mathrm{d.c.}} + H_{\mathrm{a.c.}} \cos(\omega t), \tag{3.4}$$

where $\omega$ ($= 2\pi\nu$) is the frequency of the oscillating magnetic field. The above is the situation where d.c. and a.c. fields are parallel which is the most commonly encountered. The oscillating response of the magnetisation is recorded ($M_{\mathrm{a.c.}}$) and the a.c. susceptibility is then defined by

$$\chi_{\mathrm{a.c.}} = \frac{M_{\mathrm{a.c.}}}{H_{\mathrm{a.c.}}}. \tag{3.5}$$

### 3.3.1 Three characteristic regimes

If the studied system's magnetic properties are characterised by some relaxation time, $\tau$, then its response may be split into three regimes based on the relative sizes of $\omega$ and $1/\tau$.

1. $\omega \ll 1/\tau$: The first of these regimes corresponds to the d.c. limit in which the studied system responds essentially instantaneously to the a.c. field and d.c. susceptibility is obtained ($\chi_{\mathrm{a.c.}} \approx \chi_{\mathrm{d.c.}}$). This is an equilibrium response and the moments are able to exchange energy with the lattice. This results in a measurement of what is therefore called the isothermal susceptibility, $\chi_T$ [31]. Given the increased sensitivity that may be achieved due to measuring an oscillating response, a.c. susceptibility in this regime may be

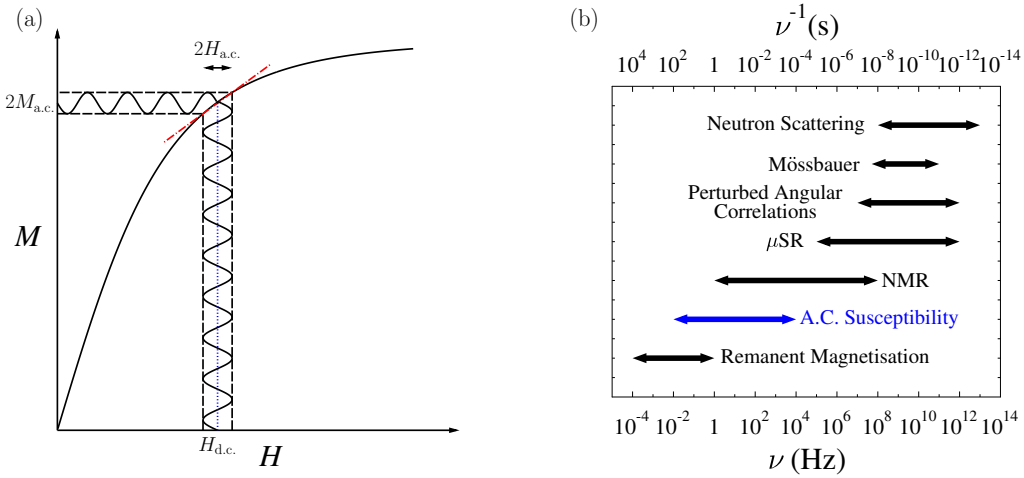



Figure 3.1: (a) Graphical demonstration of the use of a.c. magnetic susceptibility for measurement of the gradient of a magnetisation curve. The red dashed line demonstrates the gradient being measured and the blue dotted line shows the applied d.c. magnetic field which can be changed to allow different parts of the magnetisation curve to be investigated. (b) Comparison of approximate frequency ranges available to various experimental techniques. Information gathered from Refs. [27, 40, 41]. Note that (following Eq. 3.24) $\chi''$ has a maximum when $\omega\tau = 1$ and so this occurs at $\tau = \nu^{-1}/2\pi$ and the factor of $1/2\pi$ should not be forgotten.

useful in studying systems where dynamics are not being considered but the signal is weak. Furthermore, when using susceptibility as a measurement of the gradient of $M$ versus $H$, the ability to apply a d.c. magnetic field allows different regions of the $M$ versus $H$ curve to be probed as shown in Fig. 3.1(a).

2. $\omega \gg 1/\tau$: The second regime occurs when the perturbing field oscillates too quickly for the magnetic moments of the system to respond. Thus the system does not have time to equilibrate and exchange energy with the lattice. The obtained susceptibility is known as the adiabatic susceptibility, $\chi_S$ [31].

3. $\omega \approx 1/\tau$: The intermediate regime, in which the frequency of the oscillating magnetic field is comparable to the timescale of the magnetic relaxation of the system, offers a much more complex response. In this regime there may be some phase lag (and therefore dissipation) when the pertur-

bation is slightly faster or slower than the natural frequency of the system. Thus, the response is reported in two parts: in-phase and out-of-phase (or real and imaginary) components respectively, $M'_{\text{a.c.}}$ and $M''_{\text{a.c.}}$, with corresponding susceptibility, $\chi'_{\text{a.c.}}$ and $\chi''_{\text{a.c.}}$. The imaginary component relates to dissipation in the system. The a.c. magnetic susceptibility may be written as a complex number

$$\chi_{\text{a.c.}} = \chi'_{\text{a.c.}} + i\chi''_{\text{a.c.}}, \tag{3.6}$$

which at low/high frequency must reduce to the real value ($\chi''_{\text{a.c.}} = 0$) of $\chi_T/\chi_S$. For brevity, the subscript "a.c." will be neglected from this point onward. The choice of the sign of the imaginary part of the susceptibility in Eq. 3.6 is a matter of convention. In some treatments, the complex susceptibility is defined instead as $\chi' - i\chi''$, which will be adopted later in this chapter. In considering the basis of the a.c. response it is convenient to initially use the convention of Eq. 3.6 which will be shown to recover the same real and imaginary components in due course.

Ideally, when choosing a technique to examine dynamic behaviour frequencies that allow the probing of all three regimes should be available. Fig. 3.1(b) shows a comparison of several experimental techniques demonstrating both that a.c. magnetic susceptibility probes the lower frequency region and overlap does exist between techniques which can be taken advantage of should a system's characteristic time be at the edge of the available region.

Descriptions of slow magnetic relaxation observed by a.c. susceptibility typically make use of what is known as the generalised Debye model. This has found application in various systems including single-molecule magnets [31], spin glasses [37] and ferromagnets [33]. This model was originally derived and applied to dielectric systems [42–44] though has been shown to arise by considering dispersion and absorption in dielectric or magnetisable materials [45] and via thermodynamic considerations of paramagnetic salts [46]. Indeed, it has

been noted that various forms of dispersion phenomena lead to similar equations [43] suggesting that a more overarching view of the frequency-dependent response of magnetic systems may be achieved. To this end, in the following slow magnetic relaxation is considered within the framework of linear response theory which is shown to lead to the ideal Debye model.

### 3.3.2 Linear response theory

As described in Ref. [15], an arbitrary system will show a generalised displacement, $x(t)$, as a result of a generalised force, $f(t)$. The value of $x$ at time $t$ is then given by

$$x(t) = \int_{-\infty}^{\infty} \chi(t - t')f(t')\mathrm{d}t', \tag{3.7}$$

where $\chi(t - t')$ is a generalised response function. This relation is a convolution and hence it can written as a product,

$$\tilde{x}(\omega) = \tilde{\chi}(\omega)\tilde{f}(\omega), \tag{3.8}$$

by using the Fourier transform of $x(t)$, $\chi(t)$ and $f(t)$, explicitly defined as

$$\tilde{x}(\omega) = \int_{-\infty}^{\infty} e^{-i\omega t}x(t)\mathrm{d}t; \tag{3.9}$$

$$x(t) = \int_{-\infty}^{\infty} \frac{1}{2\pi}e^{i\omega t}\tilde{x}(\omega)\mathrm{d}\omega. \tag{3.10}$$

To simplify notation, tildes are dropped on Fourier transforms from this point onward and they are written as $x(\omega)$, $f(\omega)$, $\chi(\omega)$, etc. Furthermore, it is assumed that $\chi(t-t') = 0$ for $t < t'$ which is an assumption that the response cannot occur before the force (causality). This allows the definition $\chi(t) = g(t)\theta(t)$ where $\theta(t)$ is the Heaviside step function.

It is required that the function $g(t) = \chi(t)$ for $t > 0$, but use of the Heaviside

function places no constraints on $g(t)$ for $t < 0$. Therefore, $g(t)$ may be made odd and set as $g(t) = -\chi(|t|)$ for $t < 0$. Therefore, $g(\omega)$ is imaginary. This yields

$$\chi(\omega) = \frac{1}{2\pi}\int_{-\infty}^{\infty} \theta(\omega' - \omega)g(\omega)\mathrm{d}\omega'. \tag{3.11}$$

Substituting the Fourier transform of the Heaviside function ($\theta(\omega) = \pi\delta(\omega) - i/\omega$) results in

$$\chi(\omega) = \frac{1}{2}g(\omega) - \frac{i}{2\pi}P\int_{-\infty}^{\infty} \frac{g(\omega')}{\omega' - \omega}d\omega' = \chi'(\omega) + i\chi''(\omega), \tag{3.12}$$

where $\chi'$ and $\chi''$ are the real and imaginary parts of $\chi(\omega)$ and P indicates that the Cauchy principal value is taken to avoid a singularity. It should be noted that this equation means that

$$i\chi''(\omega) = \frac{1}{2}g(\omega) \tag{3.13}$$

since $g(\omega)$ has been defined to be imaginary and

$$\chi'(\omega) = P\int_{-\infty}^{\infty} \mathrm{d}\omega' \frac{\chi''(\omega')}{\pi(\omega' - \omega)}. \tag{3.14}$$

At $\omega = 0$ Eq. 3.14 reduces to

$$\pi\chi'(0) = P\int_{-\infty}^{\infty} \mathrm{d}\omega' \frac{\chi''(\omega')}{\omega'}. \tag{3.15}$$

The quantity $\chi'(0)$ is called the static susceptibility.

### 3.3.3 The damped harmonic oscillator

A useful initial example of this approach is the damped harmonic oscillator. The equation of motion for this system is

$$m\ddot{x} + \alpha\dot{x} + kx = f, \tag{3.16}$$

where $m$ is the mass, $\alpha$ is the damping constant and $k$ is the spring constant. The resonant frequency is defined as $\omega_0^2 = k/m$ and the damping as $\gamma = \alpha/m$. Rearranging and taking the Fourier transform yields,

$$\frac{1}{m} f(\omega) = (-i\omega)^2 x(\omega) - i\omega\gamma x(\omega) + \omega_0^2 x(\omega), \tag{3.17}$$

which under further rearrangement and use of Eq. 3.8 gives

$$\chi(\omega) = \frac{x(\omega)}{f(\omega)} = \frac{1}{m}\left[\frac{1}{\omega_0^2 - \omega^2 - i\omega\gamma}\right]. \tag{3.18}$$

This is a complex function and the real and imaginary parts are plotted in Fig. 3.2(a). The imaginary part $\chi''(\omega)$ is given explicitly by

$$\chi''(\omega) = \frac{\omega\gamma/m}{(\omega^2 - \omega_0^2)^2 + (\omega\gamma)^2}. \tag{3.19}$$

The static susceptibility is $\chi'(0) = 1/m\omega_0^2 = 1/k$, and integration of the above shows that the sum-rule in Eq. 3.15 is satisfied. This is shown in Fig 3.2(b). Additionally, a plot $\chi''$ against $\chi'$ in an Argand diagram is shown in Fig 3.2(c) for future reference.

If the second order derivative (inertial) term is removed from the equation of motion (i.e. setting the generalised mass to zero) this yields

$$\alpha\dot{x} + kx = f. \tag{3.20}$$

Following the same procedure as above the response function can be found as

$$\chi(\omega) = \frac{1/k}{1 - i\omega\tau}, \tag{3.21}$$

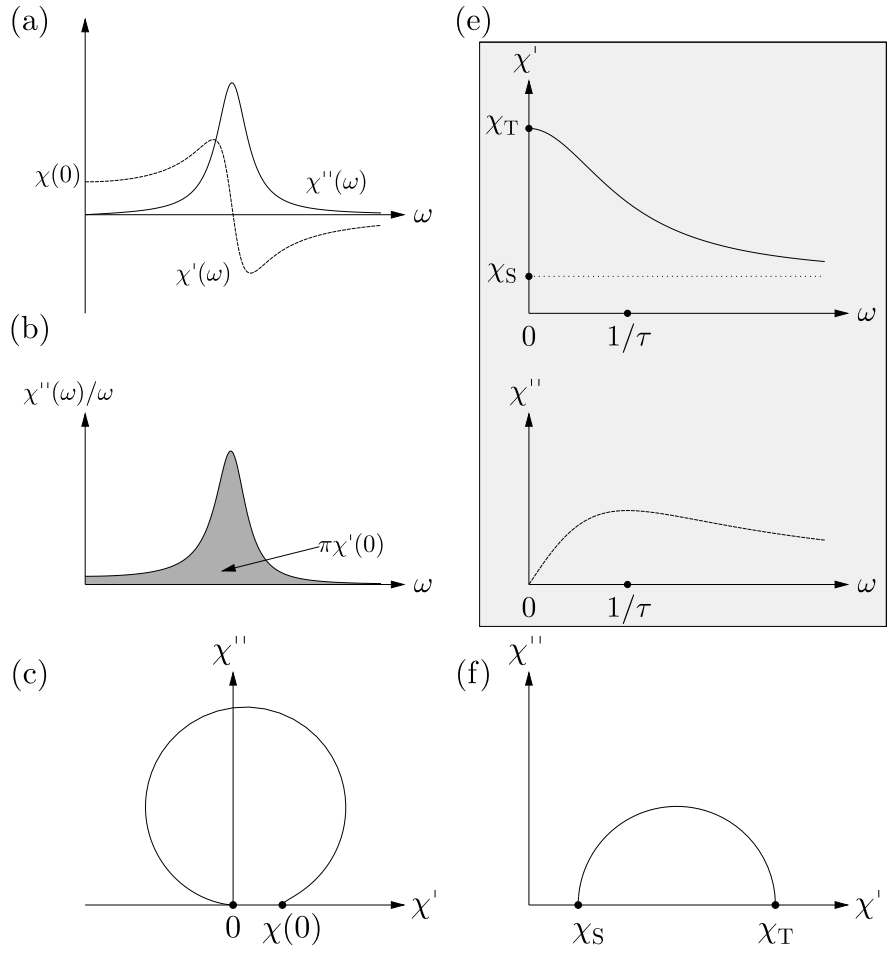



Figure 3.2: (a) The real and imaginary parts of $\chi$ as a function of $\omega$ for a damped harmonic oscillator. (b) Illustration of Eq. 3.15 for the damped harmonic oscillator. (c) The same curves as in panel (a) but plotted in an Argand diagram (or Cole-Cole plot). (e) The real and imaginary parts of $\chi$ as a function of $\omega$ for the model with no inertial term (Eq. 3.20). Note the horizontal axis is a linear scale. The maximum in $\chi''$ occurs when $\omega\tau = 1$, i.e. at $\omega = 1/\tau$. (f) The same curves as in panel (e) but plotted in an Argand diagram (or Cole-Cole plot).

where $\tau = \alpha/k$. This yields real and imaginary parts

$$\chi'(\omega) = \frac{1/k}{1+\omega^2\tau^2};$$
$$\chi''(\omega) = \frac{\omega\tau/k}{1+\omega^2\tau^2}. \tag{3.22}$$

Typically, an adiabatic response is included, $\chi_S$, resulting in

$$\chi(\omega) = \chi_S + \frac{1/k}{1-i\omega\tau}. \tag{3.23}$$

Therefore, for a.c. susceptibility this expression becomes

$$\chi'(\omega) = \chi_S + \frac{(\chi_T - \chi_S)}{1+\omega^2\tau^2};$$
$$\chi''(\omega) = \frac{(\chi_T - \chi_S)}{1+\omega^2\tau^2}\omega\tau, \tag{3.24}$$

where $\chi_T = \chi_S + 1/k$. The above equations recover the necessary high and low frequency limits stated earlier, namely $\chi_S = \chi(\infty)$ (the adiabatic susceptibility) and $\chi_T = \chi(0)$ (the isothermal susceptibility). These equations are plotted in Fig. 3.2(e) as a function of $\omega$ on a linear scale. They are presented on a logarithmic scale in Fig. 3.3(a) and (b) as the $\alpha = 0$ curves. Perhaps the most important feature of these equations is the maximum of $\chi''$ which occurs at $\omega\tau = 1$ providing a convenient method to extract the relaxation time of a system. Furthermore, the solution to Eq. 3.20 with $f = 0$ ($\tau \geq 0$) is given by

$$x(t) = x(0)e^{-\frac{t}{\tau}} \tag{3.25}$$

and describes a relaxation process with a single relaxation time. For a magnetic system, $x(t)$ is $M(t)$ and so describes an exponential decay of magnetisation. Therefore, if a magnetic system is found to show an exponential decay of magnetisation it can be expected that the dynamics can be described by Eq. 3.24. If

$\chi''$ is plotted against $\chi'$ in the Argand diagram, a characteristic semicircular form is produced as shown in Fig. 3.2(f).

### 3.3.4 Dielectric relaxation

The model this treatment has arrived at (Eq. 3.23 and Eqs. 3.24) is completely analogous to the well-known expression for dielectric relaxation described in the Debye model [44]. For Debye's treatment, the generalised displacement becomes the electric polarisation, $P(t)$, and the generalised force is an electric field, $E(t)$ (just as in magnetism they are $M(t)$ and $H(t)$ respectively). Conventionally, the Debye model is reported as a relative permittivity, $\epsilon(\omega) = 1 + P(\omega)/(\epsilon_0 E(\omega))$, rather than an electric susceptibility. Thus, the Debye model is

$$\epsilon' = \epsilon_\infty + \frac{\epsilon_S - \epsilon_\infty}{1+\omega^2\tau^2}; \epsilon'' = \frac{\omega\tau(\epsilon_S - \epsilon_\infty)}{1+\omega^2\tau^2}, \tag{3.26}$$

where $\epsilon_S$ is the static permittivity and $\epsilon_\infty$ is the permittivity in the high-frequency limit. These are the isothermal permittivity and adiabatic permittivity in the language adopted.

Much work in magnetic a.c. susceptibility has borrowed from dielectric relaxation where it is conventional to write the complex susceptibility as

$$\chi(\omega) = \chi_S + \frac{\chi_T - \chi_S}{1+i\omega\tau}, \tag{3.27}$$

The sign difference in the denominator occurs due to the previously mentioned differing convention of complex susceptibility (which is defined as $\chi_{\text{a.c.}} = \chi' - i\chi''$ for the above equation). Importantly, both Eqs. 3.23 and 3.27 yield the same real and imaginary parts. It should be noted that the Debye model fails to model short times (and therefore high frequencies) and so violates the sum rule that $\int_0^\infty \omega\chi''(\omega)\,\mathrm{d}\omega$ should remain finite [47]. This is clear at high frequencies since $\chi''$ drops off as $1/\omega$ rather than $1/\omega^2$ which would be required to satisfy this sum

rule. In dielectrics the integration is over $\omega\epsilon'' \propto f(\omega)$ where $f(\omega)$ is the oscillator strength with the resultant integration being equal to the number of electrons per unit volume [48]. This is an expression of the Thomas–Reiche–Kuhn sum rule [49, 50]. Therefore, modifications may be required if a.c. susceptibility is performed at very high frequencies where the modelling of the Debye model becomes unsatisfactory [47] which may be achieved, for example, using time-domain terahertz spectroscopy [51].

### 3.3.5 A range of relaxation times

It is important to stress by beginning with linear response theory this shows that many dispersive phenomena may be described by the same equations, namely the Debye model. The only assumption made has been that the variable of interest (i.e. magnetisation or polarisation) decays according to an exponential decay. It has simply been assumed that there is a slowly relaxing "entity" that relaxes with a single time scale. This fact also demonstrates the limitations of this model because it is restricted to isolated relaxing entities; interactions between those entities would modify equation 3.20. Indeed it is an acknowledged problem that the ideal process predicted for non-interacting electric dipoles [42, 43, 52] is rarely obtained [42, 53]. Similarly, in the case of magnetism, the limit of completely non-interacting magnetic moments also seems unlikely to be encountered due to the rich realm of cooperative effects, though it might not necessarily be a bad approximation for systems such as superparamagnets [1] or single-molecule magnets [31] (discussed in Section 3.4.1).

Several approaches have been employed in order to account for the additional complexities of real systems. One approach has been to introduce a spread of relaxation times using a phenomenological parameter $\alpha$. This is called the generalised Debye model

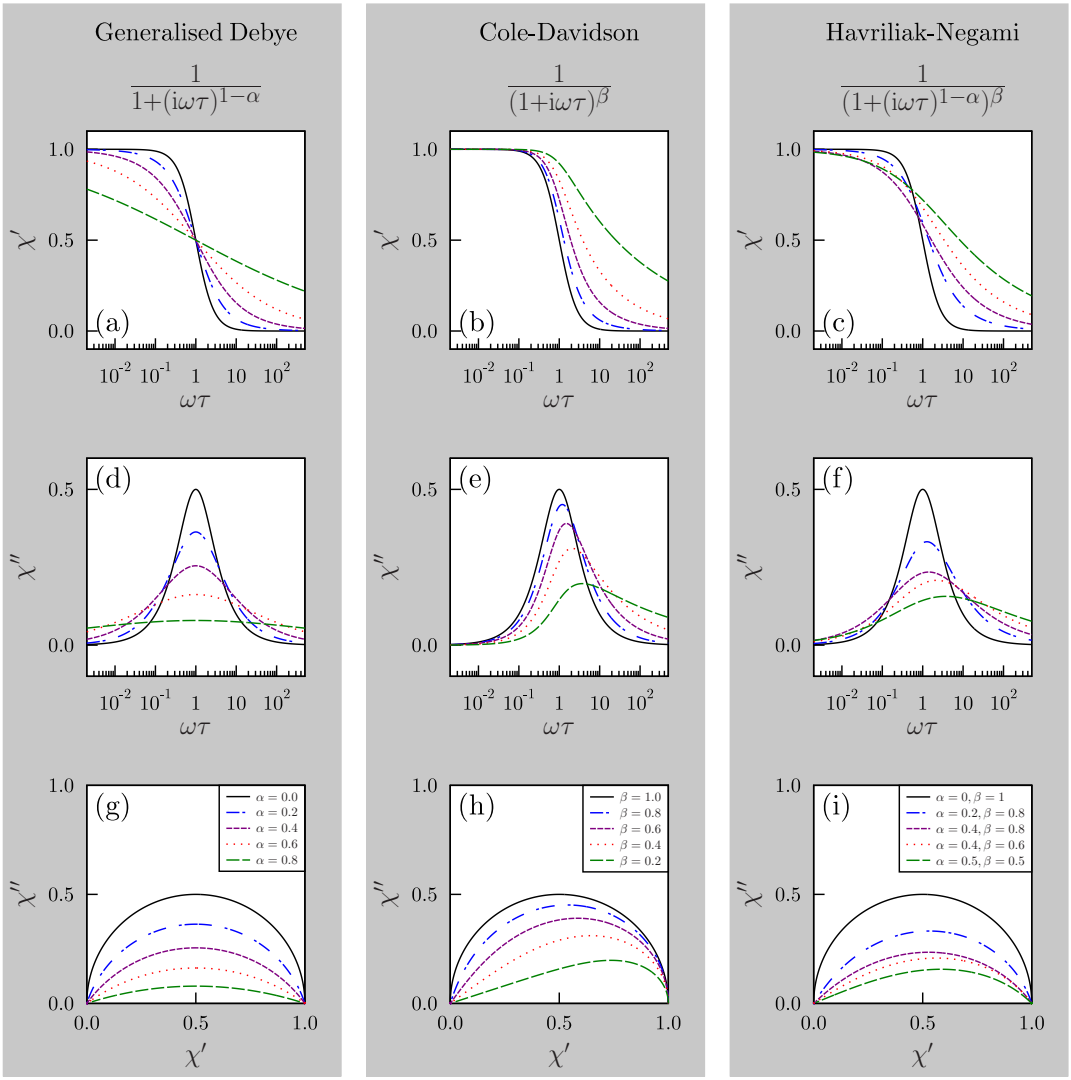



Figure 3.3: Example real ((a)-(c)) and imaginary ((d)-(f)) parts of the a.c. response and the Cole-Cole plots ((g)-(i)) for the a.c. magnetic susceptibility interpretation of the Generalised Debye ((a),(d) and (g)), Cole-Davidson ((b), (e) and (h)) and Havriliak-Negami ((c), (f) and (i)) models. These plots assume $\chi_S = 0$ and $\chi_T = 1$. At the head of each column is $y(\omega)$ for each model defined as $\chi(\omega) = \chi_S + (\chi_T - \chi_S)y(\omega)$.

$$\chi(\omega) = \chi_S + \frac{\chi_T - \chi_S}{1 + (i\omega\tau)^{1-\alpha}}, \tag{3.28}$$

where $0 \leq \alpha \leq 1$ [31, 43]. $\alpha = 0$ corresponds to no spread of relaxation times and recovers the ideal Debye model. This modification (shown in Figs. 3.3(a) and (d)) is successful in describing slowly relaxing electric [43] and magnetic systems [31, 32, 54, 55]. An alternative approach is known as the Cole-Davidson model (shown in Figs. 3.3(b) and (e)) [56] which instead places an exponent $\beta$ on the entire denominator as follows:

$$\chi(\omega) = \chi_S + \frac{\chi_T - \chi_S}{(1 + i\omega\tau)^{\beta}}. \tag{3.29}$$

In the study of dielectric systems these equations are sometimes combined to produce the Havriliak-Negami equation

$$\chi(\omega) = \chi_S + \frac{\chi_T - \chi_S}{[1 + (i\omega\tau)^{1-\alpha}]^{\beta}}, \tag{3.30}$$

which (by virtue of introducing two fitting parameters) can improve the agreement with data from real systems [57, 58]. However, the introduction of additional fitting variables risks overparameterisation and so does not necessarily indicate that the system is being accurately modelled. Plots of this model with various parameter values are shown in figures 3.3(c) and (f).

It is important to remember that the above alterations to the Debye model (Eq. 3.28–3.30) are all somewhat ad hoc adjustments introduced to improve agreement between real systems and theory. This has been accomplished by assuming a sole relaxation time no longer governs the system dynamics and modelling this effect with one or two parameters. The problem can be approached differently by, rather than slightly adjusting the ideal Debye model for a spread of relaxation times, first considering a magnet system with only two slowly relaxing magnetic entities. These correspond to relaxation times $\tau_1$ and $\tau_2$. The

total magnetisation of such a system will just be a sum of that of each entity. Therefore so too will be the susceptibility leading to

$$\chi = \chi_1 + \chi_2 = \chi_{S,1} + \frac{\chi_{T,1} - \chi_{S,1}}{1 + i\omega\tau_1} + \chi_{S,2} + \frac{\chi_{T,2} - \chi_{S,2}}{1 + i\omega\tau_2}. \tag{3.31}$$

If each entity has the same magnetic moment and $\eta$ is the fraction of the system composed of the first entity and $1 - \eta$ the fraction composed of the second entity this reduces to,

$$\chi = \chi_S + (\chi_T - \chi_S)\left(\frac{\eta}{1 + i\omega\tau_1} + \frac{1 - \eta}{1 + i\omega\tau_2}\right), \tag{3.32}$$

where it has been assumed each entity relaxes in an ideal Debye-like manner. A similar approach is used in Ref. [52], with a different definition of constants. As would be expected, Eq. 3.32 yields the superposition of two ideal Debye models with two maxima in $\chi''$ at $\omega = 1/\tau_1$ and $\omega = 1/\tau_2$ which should be easy to resolve if they are reasonable separated. Problems inherent to the ideal Debye model (such as the neglect of interactions) unfortunately remain. Simulations of Eq. 3.32 are shown in Fig. 3.4 (time constants separated by a factor of one hundred). From this plot the behaviour of the two coexisting relaxations can be clearly seen and that should one dominate (i.e. $\eta \gg 1 - \eta$ or vice versa) then only a slight distortion from the ideal Debye model is observed. Also shown in Fig. 3.4 is a Cole-Cole (or Argand) plot which is discussed in more detail in the next section. Notably, if $\tau_1$ and $\tau_2$ are not too dissimilar this can produce a Cole-Cole plot of a single asymmetric arc [52], bearing strong similarity to the arcs produced in Cole-Cole plots of the Cole-Davidson model (Fig. 3.3(h)).

A superposition of ideal Debye processes may be extended to an arbitrary number of coexisting relaxing times. Extending Eq. 3.32 in this way leads to

$$\chi(\omega) = \chi_S + (\chi_T - \chi_S)\sum \frac{\eta_n}{1 + i\omega\tau_n}, \tag{3.33}$$

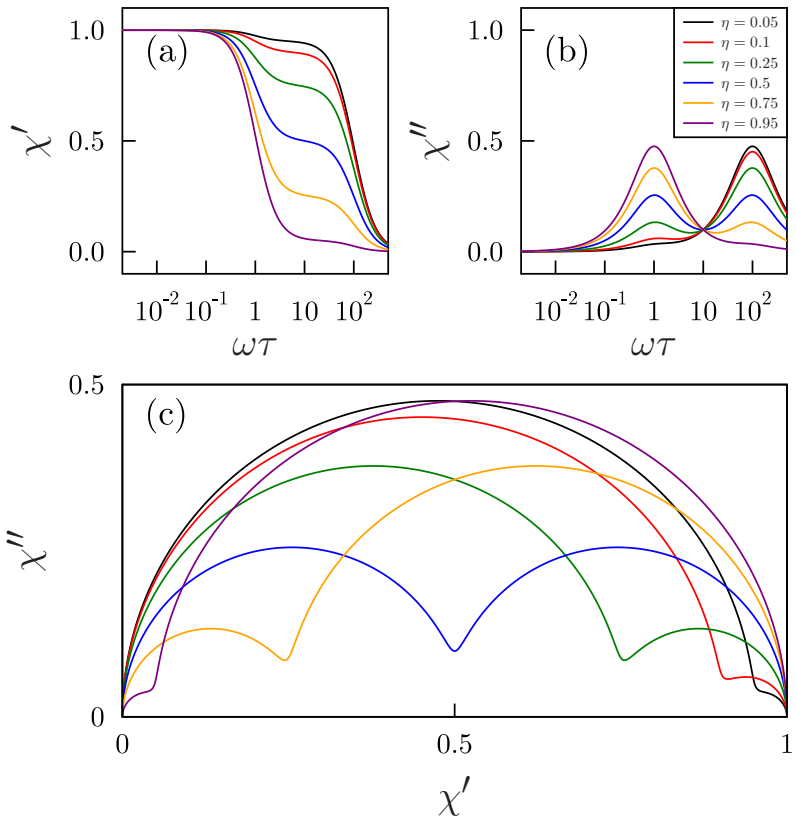



Figure 3.4: The real (a) and imaginary (b) parts of $\chi$ and the Cole-Cole plot (c) for a model using Eq. 3.32 with $\tau_1/\tau_2 = 100$ ($\tau_1 = \tau$, $\tau_2 = 0.01\tau$) and plotted for different values of $\eta$.

where $\eta_n$ is the proportion of the system with relaxation time $\tau_n$ and $\sum \eta_n = 1$. If the number of relaxation times is large, their distribution can be replaced by a continuous function and the summation may be replaced by an integration,

$$\chi(\omega) = \chi_S + (\chi_T - \chi_S) \int_{\tau_{\min}}^{\tau_{\max}} \frac{g(\tau)}{1 + i\omega\tau} d\tau, \tag{3.34}$$

with $g(\tau)$ as the distribution of relaxation times.

The form of $g(\tau)$ has yet to be determined and depends on the studied system. For a single relaxation time, $\tau_c$, the ideal Debye process must be recovered which can be accomplished for $g(\tau) = \delta(\tau - \tau_c)$. This is applicable to magnetic systems such as superparamagnets [1] and single-molecule magnets [31]. Various forms of distributions of relaxation times have been considered and are listed in Ref. [59], though in that work the distribution of relaxation times, $f(\ln(\tau))$, is defined in terms of the logarithm of the relaxation time, so that the integral in Eq. 3.34 is written as

$$\int \mathrm{d}\ln\tau \, f(\ln\tau)/(1 + i\omega\tau). \tag{3.35}$$

The two distributions can be related by $\tau^{-1} f(\ln\tau) = g(\tau)$.

In the case of the generalised Debye model the distribution function [60] is

$$g(\tau) = \frac{1}{2\pi\tau} \frac{\sin\alpha\pi}{\cosh\left((1-\alpha)\ln\left(\frac{\tau}{\tau_c}\right)\right) - \cos\alpha\pi}, \tag{3.36}$$

which is shown in Fig. 3.5(a) and (c) (the later as $f(\ln(\tau/\tau_c))$). As $\alpha$ decreases, $g(\tau)$ becomes more sharply peaked at the central value $\tau = \tau_c$ and becomes $g(\tau) = \delta(\tau - \tau_c)$ for $\alpha = 0$ as required. Fig. 3.5(c) demonstrates the distribution to be symmetric on a logarithmic scale.

Similarly, the distribution function, $g(\tau)$, for the Cole-Davidson model ($\chi(\omega) = \chi_S + (\chi_T - \chi_S)/((1 + i\omega\tau_c)^\beta)$) can be chosen as [56]

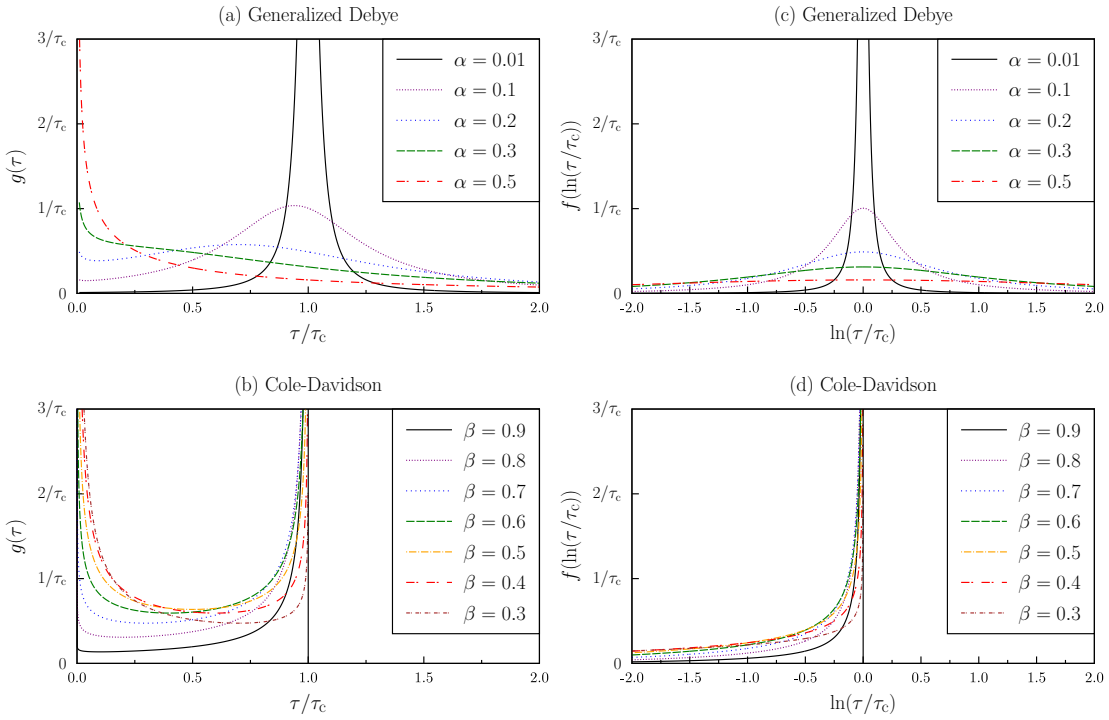



Figure 3.5: The form of $g(\tau/\tau_c)$ in (a) the generalized Debye model (plotted for different values of $\alpha$) and (b) the Cole-Davidson model (plotted for different values of $\beta$). (c) and (d) show the same distributions for the generalised Debye model and Cole-Davidson but plotted as a function of $f(\ln(\tau/\tau_c)) = \tau g(\tau)$.

$$g(\tau) = \begin{cases} \dfrac{\sin\beta\pi}{\pi}\dfrac{1}{\tau}\left(\dfrac{\tau}{\tau_c - \tau}\right)^{\beta} & \tau \leq \tau_c \\ 0 & \tau > \tau_c. \end{cases} \tag{3.37}$$

This function is plotted in Fig. 3.5(b) (as $g(\tau)$) and (b) (as $f(\ln(\tau/\tau_c))$). Here, $\tau_c$ represents the maximum cut-off relaxation unlike Eq. 3.36 in which it was the central peak. As $\beta \to 1$, the function becomes more strongly peaked at $\tau = \tau_c$ and recovers a delta function at $\beta = 1$ when the Cole-Davidson model becomes the ideal Debye model.

Importantly, while both Eqs. 3.36 and 3.37 can recover their respective models when used in Eq. 3.34 neither has an obvious physical basis. Thus they simply indicate that data can be accounted for by that particular distribution. They do not explain why that particular distribution arises or rule out some other set of processes that could, in principle, model the data equally well.

### 3.3.6 The Cole-Cole plot

The most often used method for evaluating how well experimental data fits a model of slow relaxation or comparing between models is the Cole-Cole (or Argand) plot. This has been briefly mentioned in previous sections. A Cole-Cole plot of $\chi''$ vs. $\chi'$ [31, 43] for an ideal Debye process ($\alpha = 0$ in the generalised Debye model or $\beta = 1$ for the Cole-Davidson model) yields a semicircle with the flat side on the $x$-axis (already shown in Fig. 3.2(f)). Introducing a spread of relaxation times as for the generalised Debye model causes the semicircle to distort and sink below the $x$-axis. The angle such an arc makes with the $x$-axis being $(1-\alpha)\pi$ (as shown in Appendix A). This is shown in Fig. 3.3(g) while Figs. 3.3(h) and (i) show similar plots for the Cole-Davidson and Havriliak-Negami models. If a set of these arcs at various temperatures is available a fit may be made to the generalised Debye model using the relation between $\chi''$ and $\chi'$ of

$$\chi'' = -\left(\frac{\chi_{\mathrm{T}} - \chi_{\mathrm{S}}}{2}\tan\frac{\pi\alpha}{2}\right) \pm \sqrt{\left(\frac{\chi_{\mathrm{T}} - \chi_{\mathrm{S}}}{2}\tan\frac{\pi\alpha}{2}\right)^2 + (\chi' - \chi_{\mathrm{S}})(\chi_{\mathrm{T}} - \chi')}. \quad (3.38)$$

From this the parameter $\alpha$ can be extracted (see e.g. [55]). Eq. 3.38 can be derived from Eq. 3.28, as shown in Appendix A.

If sufficient data are not available over a large enough frequency range to perform a satisfactory fit it is possible to extract $\alpha$ using the angle the data makes with the $x$-axis in the Cole-Cole plot [43]. This requires sufficient near $x$-axis (i.e. near zero $\chi''$) data. Thus, Cole-Cole plots can help test the applicability of the generalised Debye model to a system though deviations from this exist and have been noted for dielectrics [42]. As an example, the Cole-Davidson model (Eq. 3.29) shows a non-symmetric arc in a Cole-Cole plot with one side elongated

[56] (see Fig. 3.3(h)).

An ideal a.c. susceptibility experiment would involve measurement of $\chi'$ and $\chi''$ over a large frequency range so that the condition $\omega\tau = 1$ is satisfied for every important relaxation process at that particular temperature. This would be repeated for a number of temperatures allowing $\tau(T)$ for each important process to be tracked. In practice, only a small set of particular frequencies are obtained as temperature is varied due to equipment constraints (such as the long length of time associated with a single frequency measurement). If the relaxation time of the system does indeed vary with temperature ($\tau(T)$), then for a certain frequency the condition $\omega\tau(T) = 1$ may be satisfied at some temperature [31]. Assuming $\chi_T$ and $\chi_S$ vary slowly in this temperature region, a peak will occur in a plot of $\chi''$ vs. $T$ when this condition is satisfied, for a particular $\omega$, thereby allowing $\tau(T)$ to be modelled [31, 32, 61–63].

### 3.3.7 A.C. Susceptometer

Here the workings of an a.c. susceptometer are briefly discussed with further details available in [34, 40, 64, 65]. While the d.c. susceptometer of Section 3.2 requires the physical movement of the sample to produce a changing flux, an a.c. susceptometer may induce a changing flux (and therefore a voltage in the detection coils) with the a.c. magnetic field [40, 64]. A typical apparatus is shown in Fig. 3.6 comprised of d.c. magnet coils, a.c. excitation coils (providing the a.c. field) and a pair of oppositely wound detection coils [34, 40, 65]. The sample resides at the centre of one of these detection coils and the opposite winding allows the signal from the empty coil to null detected voltage not due to the sample [34]. Additional coils may be present depending on the set-up to improve measurements [40, 65, 66]. The Quantum Design PPMS fitted with an AC Measurement System (ACMS) option used for measurements of samples in this thesis operated in this manner. Similarly, a.c. measurements performed in an MPMS also operated on the same principle except the detection coils are two

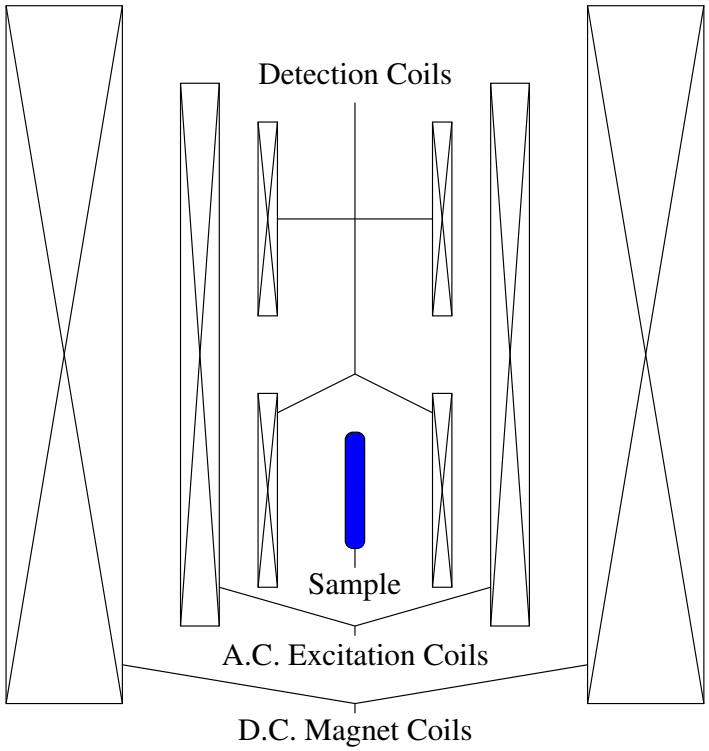



Figure 3.6: Schematic sketch of the coil set up for an a.c. susceptometer based on systems detailed in Refs. [34, 40].

of the three coil sets used for d.c. magnetometry as detailed in Section 3.2 [41]. For both of these systems samples were mounted in gelatin capsules analogous to d.c. measurements. The PPMS provides a.c. excitation frequencies of $10 \leq \nu \leq 10000$ Hz [40] while the MPMS provides frequencies of $0.001 \leq \nu \leq 1000$ Hz [41].

A lock-in amplifier can be used to detect the sample signal and resolve the in-phase ($\chi'$) and out-of-phase ($\chi''$) components [34, 66]. Care must be taken to account for any additional phase differences introduced by electronics, coil heating that may affect thermometry at low temperatures [40] and problems associated with mechanical vibration [65].

When discussing the physical apparatus used to measure a.c. susceptibility it is useful to recall the problem of demagnetising factors. In SI units, the intrinsic susceptibility $\chi$ is related to the experimentally measured susceptibility $\chi_{\rm exp}$ by $\chi^{-1} = \chi_{\rm exp}^{-1} - N_{\rm D}$, where $N_{\rm D}$ is the demagnetising factor. This is a straightforward

(if often ignored) correction for d.c. measurements but in a.c. yields a mixing of real and imaginary parts [67]

$$\chi' = \frac{\chi'_{\rm exp} - N_{\rm D}([\chi'_{\rm exp}]^2 + [\chi''_{\rm exp}])}{(1 - N_{\rm D}\chi'_{\rm exp})^2 + (N_{\rm D}\chi''_{\rm exp})^2} \tag{3.39}$$

$$\chi'' = \frac{\chi''_{\rm exp}}{(1 - N_{\rm D}\chi'_{\rm exp})^2 + (N_{\rm D}\chi''_{\rm exp})^2}. \tag{3.40}$$

Fortunately, these expressions are again only important when $\chi_{\rm exp}$ is large so can often be neglected in most encountered situations.

## 3.4 Application to real experimental systems

The models outlined in previous sections can describe a wide range of slowly relaxing phenomena. This section aims to provides some examples of various systems for which a.c. susceptibility is a useful tool as well as a discussion of the origin of the slow relaxation in each system. Both Sections 3.4.1 and 3.4.2 are particular important for the following Chapters 4 and 5 in which these types of materials are studied.

### 3.4.1 Superparamagnets and Single-Molecule Magnets

Superparamagnets and single-molecule magnets (SMMs) are arguably the simplest systems exhibiting slow magnetic relaxation and so are excellent example systems to begin discussing. Superparamagnets are magnetic particles of sufficiently small size such that multiple magnetic domains cannot form [1, 31]. Thus, they are single domain particles. SMMs (sometimes called zero-dimensional molecular magnets) are a subset of the greater class of molecular magnets [1, 68]. An SMM consists of a core cluster of metal ions possessing magnetic moments held together by organic ligands. Fig. 3.7(a) shows an example SMM molecule called $Ni_{12}$ which consists of twelve $Ni^{2+}$ ions and has a $S = 12$ ground state. No strong structural links exist in crystals of these compounds allowing each to be considered as isolated and intermolecular exchange

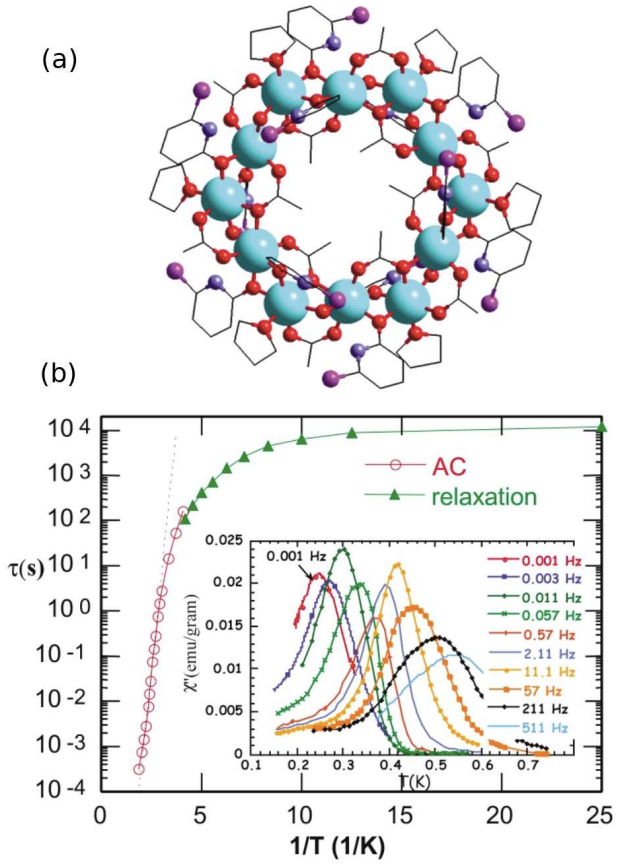



Figure 3.7: (a) The single molecule magnet $Ni_{12}$ (chemical formula $[Ni_{12}(chp)_{12}(O_2CMe)_{12}(H_2O)_6(THF)_6]$, where chp = 6-chloro- 2-pyridonate). (b) $1/\tau$ against $1/T$ measured from a.c. susceptibility (red circles) or relaxation (green triangles); inset: $\chi''(T)$ at 10 frequencies. Adapted from Ref [71].

largely neglected [68]. This leads to these compounds sometimes being referred to as zero–dimensional magnets. Intramolecular exchange between magnetic ions in the core metal cluster produces a net "giant spin" ground state (such as the $S = 12$ ground state in $Ni_{12}$), so that each molecule can be considered as a single, giant magnetic moment to an approximation [31, 69, 70]. Thus SMMs can be considered as (approximately) single molecule superparamagnets and would be expected to display superparamagnetic behaviour. Furthermore, the moments in both superparamagnets and SMMs are well isolated from each other and therefore are good candidates for exhibiting slow relaxation of the kind described by the Debye model.

Clearly, the slowly relaxing magnetic entities for these systems are the large

moments but in order to relax slowly there must be another feature causing a sluggishness to their reorientation. In both systems this arises from uniaxial anisotropy (i.e. they contain a magnetic easy axis) making it energetically favourable for moments to align along a specific axis. For superparamagnets, this uniaxial anisotropy arises from magnetocrystalline anisotropy or shape anisotropy and can be described by an energy density $\mathcal{E}$ given by

$$\mathcal{E} = K \sin^2 \theta, \tag{3.41}$$

where $K$ is a constant describing the anisotropy energy density and $\theta$ is the angle made with the easy axis by the single domain moment [1, 72]. If $K > 0$, energy is minimized when the moment is aligned parallel or anti-parallel with the easy axis. Therefore, the potential energy diagram of the magnetic moment is a symmetric double well with an energy barrier separating the parallel and anti-parallel configurations. For SMMs, the anisotropy results from a zero field splitting parameter, $D > 0$, leading to a Hamiltonian $\mathcal{H}$ of the form

$$\mathcal{H} = -DS_z^2 + E(S_x^2 - S_y^2) + g\mu_{\mathrm{B}}\boldsymbol{B} \cdot \boldsymbol{S}, \tag{3.42}$$

where $\boldsymbol{S}$ is the spin operator, $S_z$ is its component along the $z$-axis, $S_{x/y}$ is its component along the $x/y$-axis, $E$ is an additional anisotropy term, $g$ is the g-factor and $\boldsymbol{B}$ is the magnetic field [31, 68–70]. The term premultiplied by $E$ introduces a medium and hard axis and is essentially a higher order term that is initially set to zero in this discussion [31]. This also yields a symmetric double well potential energy diagram when $\boldsymbol{B} = 0$ and $E = 0$ (analogous to superparamagnets) and is shown in Fig 3.8(a). The quantized $+S$ and $-S$ states lie on opposite sides of an energy barrier of height (or activation energy) $E_{\mathrm{a}}$. It should be noted that in some papers the parameter $D$ is defined with opposite sign so the precise form of Eq. 3.42 should always be checked. Slow magnetic relaxation arises due to the

fact that to change orientations between parallel and anti-parallel to the easy axis the magnetic moments must overcome this energy barrier. If this process occurs thermally, the relaxation time $\tau$ can be described by an Arrhenius law

$$\tau(T) = \tau_0 \exp\left(\frac{E_\mathrm{a}}{k_B T}\right), \tag{3.43}$$

where $\tau_0$ is a constant [31]. This is temperature dependent and for SMMs is associated with the two-phonon Orbach process. In this process the spin system absorbs a phonon to an excited state before subsequently emitting a phonon of a different energy and relaxing to a different state on the other side of the energy barrier in Fig 3.8(a) [6, 31, 73].

A feature of SMMs is the blocking temperature, $T_\mathrm{B}$, which may be defined as follows. An experiment is performed at a specific frequency $\omega$, corresponding to a particular time constant $\tau_\mathrm{measure}$. As $\tau$ is temperature dependent ($\tau(T)$), when $T$ is lowered the magnetization changes from dynamic (at high $T$, where $\tau(T) \ll \tau_\mathrm{measure}$) to frozen (at low temperature $\tau(T) \gg \tau_\mathrm{measure}$). This occurs at $T_\mathrm{B}$ and depends entirely on the value of $\tau_\mathrm{measure}$ employed (thus $T_\mathrm{B}$ is frequency dependent). This is demonstrated in the inset of Fig. 3.7(b). Therefore, $T_\mathrm{B}$ marks the temperature for a specific measurement timescale below which relaxation is appreciably slow. A peak appears in $\chi''(T)$ which moves to lower temperatures as the measurement frequency decreases. From these $\chi''(T)$ peaks the relaxation time, $\tau(T)$, can be extracted as shown in Fig. 3.7(b).

Since each molecule of a SMM is identical (due to being single molecules) they do not suffer the problem of superparamagnetic particles of variable particle sizes leading to different relaxation times. Furthermore, as they are magnetically well isolated SMMs can be expected to be good realisations of the ideal Debye model. In real systems, a range of coexisting relaxation processes may exist resulting in a better model being the generalised Debye model with $\alpha \neq 0$ [31].

Fig. 3.9(a) and (b) shows example a.c. susceptibility for the single molecule

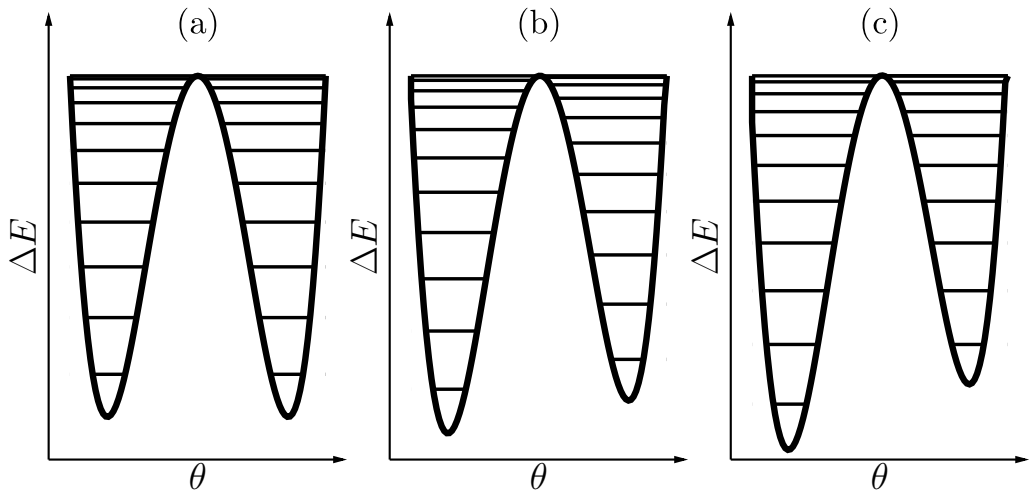



Figure 3.8: Potential energy diagram for a system described by the Hamiltonian $H = -DS_z^2$ with an externally applied magnetic field of $B = 0$ ((a)), $B = D/2g\mu_{\mathrm{B}}$ ((b)) and $B = D/g\mu_{\mathrm{B}}$ ((c)). Adapted from reference [68].

magnet $Co_2Dy$ [54]. It should be noted that Chapter 4 details a study of isostructural compounds with different $Ln^{3+}$ ions. Strictly this compound falls under the class of single ion magnets since only the rare earth ion possesses unpaired electrons and therefore a magnetic moment [54]. Frequency separation is evident in these plots indicating the presence of slow magnetic relaxation in this temperature range. Furthermore, Cole-Cole plots of this compound with fits to Eq. 3.38 yielded $\alpha$ in the range of $0.39$–$0.46$ for $6.5 < T < 9.0$ K [54]. It is clear that slow magnetic relaxation has been greatly enhanced by the application of a d.c. magnetic field yielding a series of peaks in real and imaginary parts shown in Fig. 3.9(b). In other words, $Co_2Dy$ shows field-induced slow magnetic relaxation.

The effect of a d.c. magnetic field in this compound is to close an alternate relaxation pathway, known as macroscopic quantum tunnelling or tunnelling of magnetisation [31, 69, 74]. This allows spins to tunnel through the energy barrier separating up and down orientations rather than relying on a thermal process over to jump over it [31, 68, 69, 74]. This is a faster relaxation process so can hide the slower thermal relaxation of an Arrhenius type process. For quantum tunnelling to occur in a system there must be an additional term

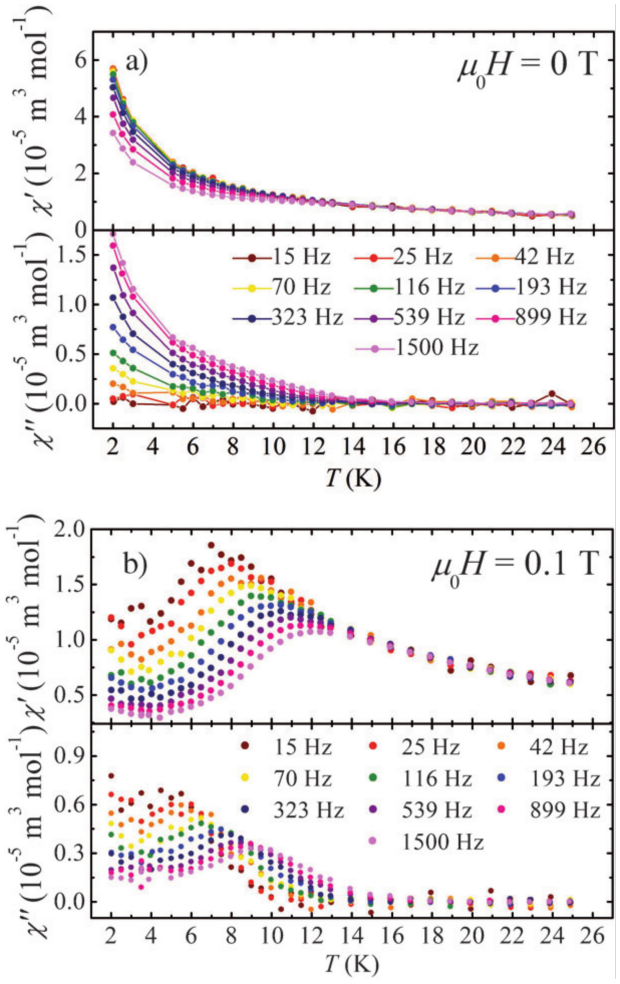



Figure 3.9: Results of a.c. susceptibility measurements on $[Co_2^{III}Dy(L)_2(\mu\text{-}O_2CCH_3)_2(H_2O)_3]\cdot NO_3\cdot MeOH\cdot 4H_2O$, known as $Co_2Dy$, in an a.c. magnetic field of $\mu_0 H_{\mathrm{ac}} = 0.4$ mT adapted from Ref. [54]. In the chemical formula, $LH_3$ = 2-methoxy-6-[2-(2-hydroxyethylamino)ethyliminomethyl]phenol. (a) The real and imaginary parts of a.c. susceptibility in a d.c magnetic field of $\mu_0 H_{\mathrm{dc}} = 0$ T. (b) The real and imaginary parts of ac susceptibility in a d.c magnetic field of $\mu_0 H_{\mathrm{dc}} = 0.1$ T.

in the Hamiltonian that does not commute with $S_z$ [31, 69]. This is achieved for non-zero $E$ in Eq. 3.42 [31, 69], though other higher-order terms can contribute, all depending on the relevant symmetries of the magnetic ions in the molecule [31]. Quantum tunnelling can take place when energy levels on either side of the energy barrier become degenerate and so is more likely at zero applied d.c. magnetic field and at higher fields corresponding to new energy levels being brought into degeneracy [68, 69, 74]. These tunnelling conditions can be observed by studying the magnetic hysteresis loop which breaks up into a series of steps at these specific fields when degeneracy is recovered and quantum tunnelling becomes more rapid [75]. Fig. 3.8(b) and (c) illustrates the effect of increasing an applied magnetic field (assumed parallel to the $z$-axis) where the degeneracy between up and down states is progressively broken and temporarily re-established between new levels. It would be expected for no tunnelling to occur in Fig. 3.8(b) but be allowed in figure 3.8(c). This is the effect occurring in Fig. 3.9(a) and (b) and other field-induced SMMs [54, 76–78].

The treatment of SMMs to this point has not gone into detail of the various processes that may lead to this spread of relaxation times (beyond quantum tunnelling). It is useful to consider the additional relaxation processes available to SMMs. Consider an SMM relaxing from initial energy level A to final level B (on the opposite side of the energy barrier). First a "direct" process may occur with a transition from A to B with the emission or absorption of a phonon of the energy difference between the two levels, $\delta = E_{\mathrm{B}} - E_{\mathrm{A}}$. This involves a coupling between the crystal field of the magnetic ion and the strain field produced by the phonon. The relaxation rate of the direct process is proportional to temperature (essentially because the number of phonons available at temperature $T$ scales with $T$). Additionally, as a one-phonon process, it is not very efficient since the density of states of these low-energy phonons is rather low.

Two-phonon processes utilise more abundant higher-energy phonons. These

involve a transition from first level A to an intermediate state C (of energy greater than A or B) by absorbing a phonon of energy $\Delta = E_{\mathrm{C}} - E_{\mathrm{A}}$. This is followed by the emission of a phonon of energy $\Delta - \delta$ transitioning to level B. This is an Orbach process with rate proportional to the Bose factor $(\exp(\Delta/k_{\mathrm{B}}T) - 1)^{-1}$ which is proportional to $\exp(-\Delta/k_{\mathrm{B}}T)$ if $\Delta \gg k_{\mathrm{B}}T$ (i.e. recovers the Arrenhius form in equation 3.43 with $E_{\mathrm{a}} = \Delta$). If the intermediate excited state is not real but virtual it is known as a Raman process.

The precise form assigned to the these various relaxation processes can depend on the magnetic ion involved (Kramers or non-Kramers) as well as the temperature and field regime studied. For example, studies of a trigonal prismatic mononuclear Co(II) complex and a mononuclear hexacoordinate Cu(II) complex found slow relaxation to be due to the sum of Orbach and quantum tunnelling processes, as well as direct and Raman phonon processes, and the data were fitted to an expression given by

$$\tau^{-1} = AH^2T + \frac{B_1}{1 + B_2H^2} + CT^n + \tau_0^{-1} \exp\left(\frac{-E_a}{k_BT}\right), \tag{3.44}$$

where $A$, $B_1$, $B_2$, $C$ and $n$ are constants and $H$ is the magnetic field [62, 63]. These correspond to direct, quantum tunnelling of magnetisation, Raman and Orbach processes respectively. Strictly this expression is true only for small d.c. magnetic fields which have not begun to recover the degeneracy requirement of quantum tunnelling between the $-S$ and $+S-1$ states. This clearly demonstrates that a.c. magnetic susceptibility may have a dependence on the applied magnetic field through its effect on $\tau$. Very often in the investigation of SMMs it is the Arrhenius type relaxation that is the relaxation of interest (in order to extract the height of the energy barrier, $E_{\mathrm{a}}$). Thus a d.c field and frequency study must be performed to identify the conditions needed to minimise contributions to $\tau^{-1}$ from those field-dependent parts [78–80].

These systems also provide a real example of the case of two $\tau$'s (as described

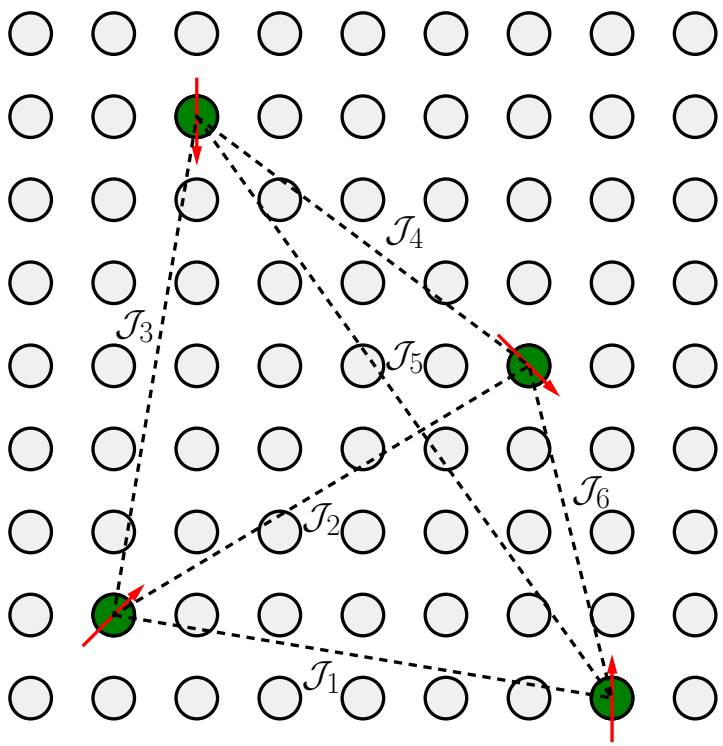



Figure 3.10: A schematic of a typical spin glass. A low concentration of spins have populated a non-magnetic 2-D square lattice. Due to their random locations the exchanges between each ($\mathcal{J}_i$ for $i = 1$ to $6$) are also random leading to frustration.

by equation 3.31). The molecule (Cp*)Er(COT) (where Cp* is $C_5Me_5^-$ and COT is $C_8H_8^{2-}$) features an Er(III) ion sandwiched between two carbon rings. Measurements of this compound revealed two separate sets of peaks appearing in $\chi''$ at different ranges of temperatures [81]. A.c. data were successfully modelled via a version of Eq. 3.31 incorporating the generalised Debye model [81]. The source of two separate $\tau$'s in this compound was suggested to be two separate conformations of (Cp*)Er(COT) [81]. Similarly, a mononuclear hexacoordinate Cu(II) complex was found to contain two $\tau$'s at low temperature which was suggested to be due to very weak intercluster interactions creating small oligomers (the discrete SMMs bonding together in "clumps") [63].

### 3.4.2 Spin Glasses

A spin glass can be formed if a non-magnetic lattice is populated with a dilute random distribution of magnetic atoms as shown in Fig 3.10. A typical example is the CuMn system in which magnetic Mn atoms replace Cu atoms at the few per cent level [37]. Cu is a metal and so the exchange interactions between the Mn atoms is mediated by the RKKY interaction through the conduction electrons [37]. As shown in Section 1.3, the RKKY interaction oscillates between ferromagnetic and antiferromagnetic with distance introducing frustration to the system. Therefore, spin glasses may be defined as random, mixed-interacting systems which, when temperature is lowered, undergo a freezing transition from a paramagnetic state to a metastable state known as the glass or frozen state lacking in any long range magnetic order [1, 37, 61, 82]. The glass state arises from competing interactions between individual magnetic moments and leads to a multidegenerate ground state [1, 37].

This multidegenerate ground state means that the system can adopt a number of equally favourable orientations, but upon freezing the system becomes stuck in one particular configuration. Slow relaxations arise as individual magnetic moments begin to reorient, creating additional frustrations and further reorientation of other magnetic moments. This process is very complex because each magnetic moment occupies a different environment and so may be frustrated in a different way (due to the random site distribution and random exchange). As the freezing temperature, $T_{\mathrm{f}}$, is approached from higher temperatures some moments begin to cease behaving independently and start to form growing clusters [1, 60]. A variety of size of clusters can coexist, leading to a wide distribution of relaxation times.

Early a.c. susceptibility measurements of spin glasses identified a distinctive cusp in the in-phase component, $\chi'$, at $T_{\mathrm{f}}$ [37, 61, 82]. Interpreting a spin glass as a collection of superparamagnetic clusters can allow the use of Eq. 3.34 which

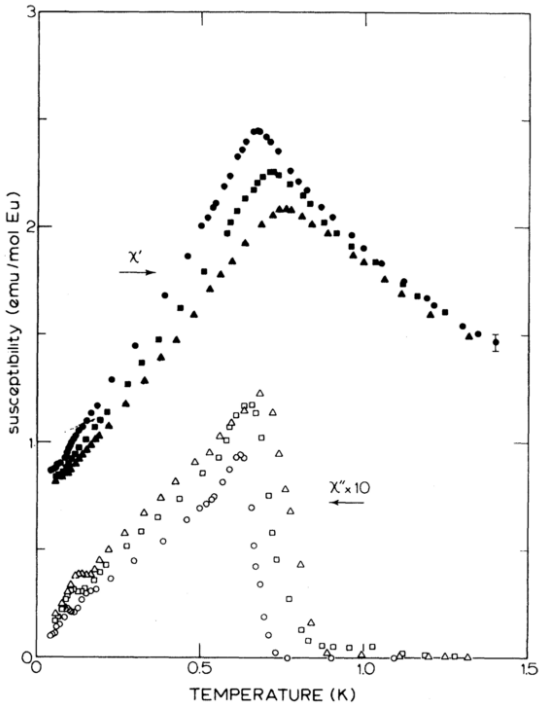



Figure 3.11: Example a.c. susceptibility of spin glass $(Eu_{0.2}Sr_{0.8})S$ at $\mu_0 H_{\mathrm{d.\,c.}} = 0$ T and $\mu_0 H_{\mathrm{a.\,c.}} = 0.01$ mT from Ref. [86]. Filled shapes correspond to $\chi'$ while empty refer to $\chi''$ with $\circ = 10.9$ Hz, $\square = 261$ Hz and $\triangle = 1969$ Hz.

explicitly incorporates a distribution of relaxation times in $g(\tau)$ [83], often assumed to be Gaussian [84] though this does not always hold [85]. In this interpretation, freezing occurs when a large proportion of the superparmagnetic clusters are below their respective $T_{\mathrm{B}}$. Sometimes data are fitted to Eq. 3.28 to crudely monitor the spread of relaxation times parameterised by $\alpha$ [37, 60]. This equates to assuming the distribution of relaxation times to be Eq 3.36. Each of these approaches aims to essentially alter a basic Debye relaxation. As shown previously, a Debye relaxation is appropriate for isolated relaxing entities which spin glasses are clearly not.

As an example, a.c. susceptibility data [86] for the spin glass $(Eu_{0.2}Sr_{0.8})S$ are shown in Fig. 3.11. The Cole-Cole plot of this data (Fig. 3.12) shows strongly depressed semi-circles suggesting a broad distribution of relaxation times. In fact, the broader the distribution of relaxation times the broader and more rounded the expected $\chi''$ peak. This peak occurs when the average relaxation time $\tau_{\mathrm{avg}}$ matches $\omega^{-1}$.

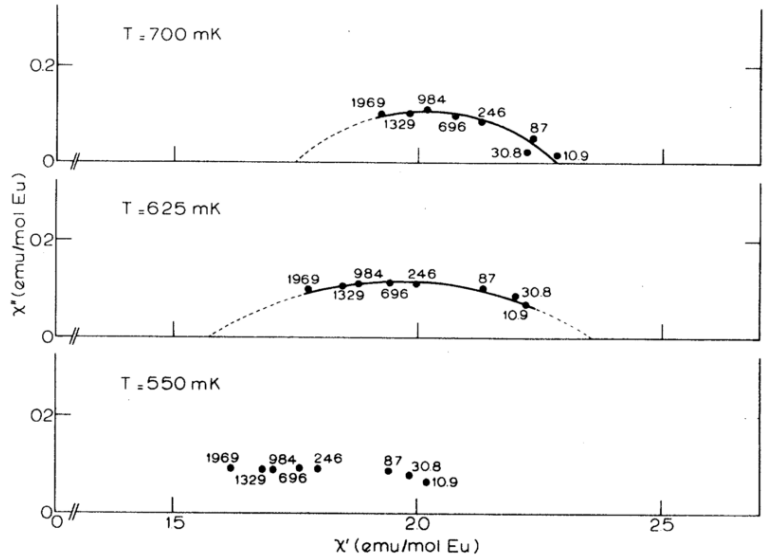



Figure 3.12: Cole-Cole plots of $(Eu_{0.2}Sr_{0.8})S$ at $\mu_0 H_{\mathrm{d.\,c.}} = 0$ T and $\mu_0 H_{\mathrm{a.\,c.}} = 0.01$ mT from Ref. [86]. Numbers in the plot correspond to a.c. drive frequencies. Dashed lines are projections of the data assuming it to be symmetric.

Since $\tau_{\mathrm{avg}}$ is temperature dependent, the form of $\tau_{\mathrm{avg}}(T)$ can be used to try to identify the type of relaxation. An initial attempt at modelling the temperature evolution $\tau_{\mathrm{avg}}(T)$ uses an Arrhenius expression which is sensible if the system were composed of superparamagentic clusters. However, this leads to unphysical values of the parameters $E_{\mathrm{a}}$ and $\tau_0$ [37, 82, 86]. In order to better account for the interacting nature of spin glasses the Vogel-Fulcher law may be used,

$$\tau = \tau_0 \exp\left(\frac{E_{\mathrm{a}}}{k_{\mathrm{B}}(T - T_0)}\right) \tag{3.45}$$

which is better suited to glass-like systems [82, 86, 87]. Here, $E_{\mathrm{a}}$ and $\tau_0$ remain the activation energy and characteristic relaxation time while $T_0$ is a new parameter that accounts for the interactions occurring between moments in a spin glass [32, 88]. It should be noted that $\tau$ may be modelled by further equations [32, 89]. The frequency dependence of the extracted freezing temperature (the temperature at which $\chi'$ takes its maximum) is given by $f = \mathrm{d}\ln T_{\mathrm{f}}/\mathrm{d}\ln\omega$ and

can therefore be studied by evaluating the quantity

$$f = \frac{\Delta T_{\mathrm{f}}}{T_{\mathrm{f}} \Delta(\ln(\omega))}. \tag{3.46}$$

This is equivalent to assuming $T_{\mathrm{f}} \propto \omega^{f}$. Spin glasses typically take a value between $0.001$ and $0.08$ (larger values are found for single molecule magnets [31, 37]) and thus $T_{\mathrm{f}}$ has a very weak frequency dependence, reflecting the broad distribution of relaxation times in spin glasses.

### 3.4.3 Spin Ice

Like spin glasses, spin ices show slow magnetic dynamics. However, while slow dynamics arise in spin glasses from frustration and randomness due to the disordered structure spin ices show only frustration with an ordered structure. Spin ice behaviour was first identified in certain rare-earth pyrochlores. Pyrochlores are a structural class of compounds with formula $A_2B_2O_7$ with rare earth A residing on the vertices of a network of corner-sharing tetrahedra [90, 91]. When A = Dy or Ho and B = Ti, the crystal field associated with the A cations exhibits strong Ising anisotropy that causes each A spin to lie along the line joining the centres of the two neighbouring tetrahedra which share the corner occupied by the A cation (these are the $\langle 111 \rangle$ directions). Each spin can lie parallel or antiparallel to this line. The dipolar interaction and weak antiferromagnetic superexchange results in an effective ferromagnetic interaction. This, in combination with the single-site anisotropy, results in a spin arrangement that requires each tetrahedron to satisfy $\sum_i \vec{S}_i = 0$. This is accomplished with two of the four tetrahedron spins pointing into the centre of the tetrahedron while the remaining two point out. This is similar to the proton rules of water ice [92, 93]. There are a large number of ways of satisfying this constraint and so this results in a degenerate ground-state configuration (lacking long-range order down to low temperatures) [90, 94].

A.c. magnetic susceptibility measurements on spin ice show an Arrhenius-like behaviour at high temperature well described by a single relaxation time (due to single ion processes and mixing with excited states) but on cooling the dynamics begin to freeze out [95]. The behaviour of spin ices can look very similar to spin glasses with a low temperature peak in d.c. susceptibility accompanied by a divergence between ZFC and FC sweeps (indeed both show a freezing temperature $T_{\mathrm{f}}$) [95]. This is expected as in both cases a slowing down of spin dynamics is occurring.

The features of spin ices that have garnered the most attention are their low temperature excitations. If a single spin flips the two-in, two-out constraint on the tetrahedra is broken creating a "three-in/one-out" and "three out/one in" pair of tetrahedra. This state can be considered as a monopole-antimonopole pair [94, 96] and further spin flips allow the monopole and antimonopole to separate, travelling through the lattice (the initial spin flip is said to have been "fractionalised"). Clearly the movement of these monopoles (as they require spin flips to move) can be the source of low-temperature slow magnetic relaxation in these compounds. In fact, an early description of spin ice magnetic relaxation by Ryzhkin [94] was formulated by exploiting the analogy with dielectric relaxation in water ice. This results in an a.c. susceptibility of the type described by the ideal Debye model. Further consideration of this approach can be found in the original article [94] and in [38].

As an example of slow magnetic relaxation in spin ices, the a.c. susceptibility of one of the most highly studied classical spin ices ($Dy_2Ti_2O_7$) is shown in Fig. 3.13. The low temperature set of peaks ($\sim 1$ K) in $\chi'$ match the freezing transition found in d.c. susceptibility. However, a.c. susceptibility reveals peaks in $\chi''$ at higher temperatures (up to $\sim 20$ K) measured at high $\omega$ [67, 95]. The arcs in the Cole-Cole plots in Fig 3.14 allow these data to be modelled and the average relaxation time $\tau(T)$ can be extracted, as shown in Fig. 3.15. This plot shows

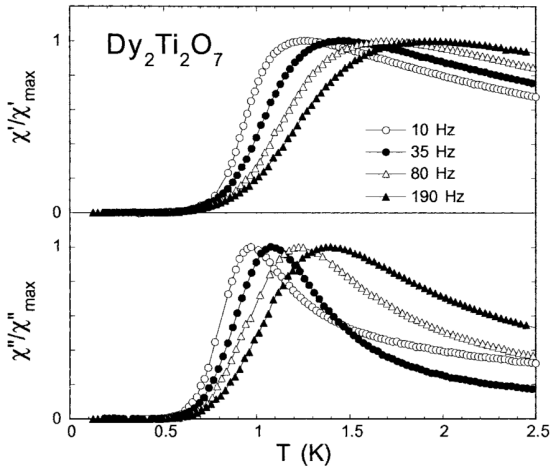



Figure 3.13: Results of low temperature a.c. susceptibility measurements on spin ice $Dy_2Ti_2O_7$ from Ref. [67] at $\mu_0 H_{\mathrm{d.\,c.}} = 0$ T and $\mu_0 H_{\mathrm{a.\,c.}} = 0.5$ mT.

three distinct regions: an increase of $\tau$ as decreases in the high-temperature region (associated with excitations to higher crystal field levels), a plateau (so temperature independent) region below $\sim 12$ K (associated with quantum tunnelling processes through the crystal field barrier) and finally a sharp increase at $\sim 2$ K (associated with monopole dynamics), explainable only by including the Coulomb interaction between charges [97].

### 3.4.4 Long Range Magnetic Order

All systems discussed up to this point have lacked long range magnetic order. However, slow magnetic relaxation can also be observed in systems with long range order if they contain some component which responds rather sluggishly. The pertinent question is: "What is the sluggish entity?" Consider first a ferromagnet in which each spin is coupled to a neighbour by an exchange constant $|\mathcal{J}|$. The dynamics of the spins occurs on a frequency scale given by $|\mathcal{J}|/\hbar$ which is far greater than the typical frequencies available in a.c. susceptibility (and hence spin waves are studied using neutron scattering, see Fig 3.1(b)). However, the already described ferromagnetic domains (specifically the inherently frustrated domain walls) are candidates for slow magnetic relaxation in the frequency range of a.c. magnetic susceptibility.

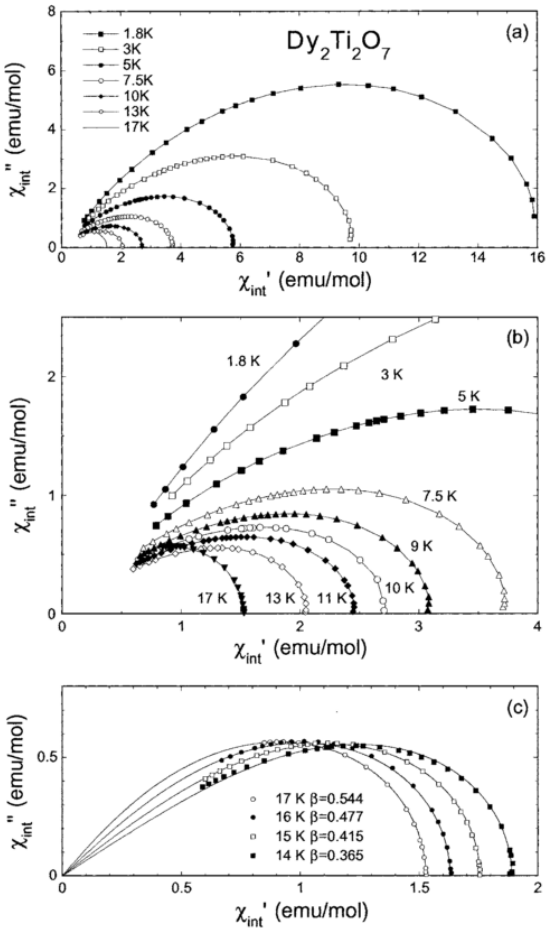



Figure 3.14: Cole-Cole plot of the frequency dependent feature of $Dy_2Ti_2O_7$ from Ref. [67]. Measurement parameters were $\mu_0 H_{\mathrm{d.\,c.}} = 0$ T and $\mu_0 H_{\mathrm{a.\,c.}} = 0.5$ mT and $\chi'_{\mathrm{int}}/\chi''_{\mathrm{int}}$ indicate $\chi'/\chi''$ corrected for demagnetising factor. (a) shows data over a wide temperature range. (b) shows data focused near the origin and (c) shows high temperature fits to the Cole-Davidson model (Eq. 3.29).

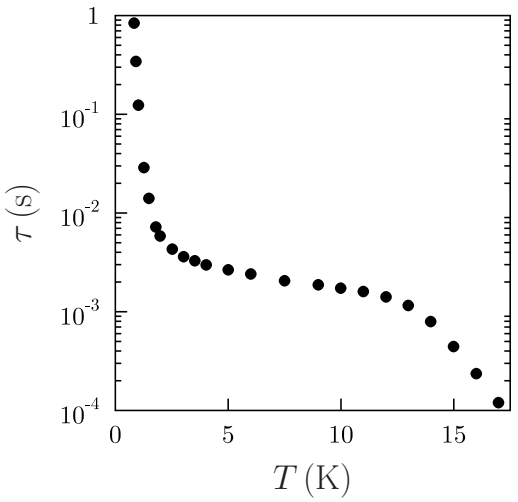



Figure 3.15: The extracted $\tau(T)$ of $Dy_2Ti_2O_7$ from the data of [95].

Domain walls in ferromagnets (and also ferrimagnets) are structures much larger than a single spin and so are more easily affected by a slowly oscillating magnetic field. This is sensible considering that domain walls are somewhat frustrated (due to being built of spins not entirely satisfying their exchanges) [1]. Thus they will have some characteristic timescale yielding a non-zero $\chi''$ detectable in a.c. measurements [32]. Various types of domain wall movement can be measured, including dynamic wall pinning and depinning, as well as domain structure reconstruction (which has been detected in a study of $Sm_2Fe_{17}$ [33]) and irreversible magnetisation rotation [32]. The Curie temperature $T_{\mathrm{C}}$ can be used as a rough estimate of the size of the magnetic exchange, and so for materials with high $T_{\mathrm{C}}$ (and hence large $J$) one may need very high frequencies (at the top of the range of frequencies available to a.c. susceptometers) in order to observe the frequency-dependent relaxation [32].

In antiferromagnets, a domain wall cannot be driven using an oscillating magnetic field (due to the anti-alignment of spins) and so there is not a mechanism for the moments to absorb energy. Thus an antiferromagnetic transition may be detected via a.c. susceptibility in $\chi'$ but will be absent in $\chi''$ showing no dissipation [32]. This does offer a method of differentiating between ferro/ferrimagnetism and antiferromagnetism using a.c. susceptibility.

### 3.4.5 Paramagnetism

A final magnetic system to consider is paramagnetism. In this state the magnetic moments are free to relax at a rate given by the spin-spin relaxation time which is very fast (i.e. $\approx 10^{-9} - 10^{-10}$ s) meaning that the system responds effectively instantaneously, at least on the timescales accessible to a.c. susceptibility [6, 31, 32]. Thus a paramagnet should not show slow relaxation and $\chi_{\mathrm{T}} = \chi_{\mathrm{S}}$ since the lattice is not involved. This sets $\chi'' = 0$ according to Eq. 3.24. The presence of a non-zero $\chi''$ can be indicative of a departure from paramagnetism. This statement is only true under zero applied d.c. magnetic field. The application of a

d.c. field creates a net magnetization and the possibility of spin-lattice relaxation due to direct phonon processes, which are of relaxation times accessible by a.c. susceptibility [31].

### 3.4.6 Superconductors

Despite the lack of a distinct magnetic moment, superconductors can show slow magnetic dynamics. This is associated with the mixed state of type II superconductors. Here the sluggishness is related to the Abrikosov flux lattice. If a current density $\boldsymbol{J}$ flows in a superconductor in a magnetic field $\boldsymbol{B}$ then a Lorentz force of density $\boldsymbol{J} \times \boldsymbol{B}$ acts on the flux lines. If these line vortices move at speed $\boldsymbol{v}_{\mathrm{L}}$, then a transverse electric field $\boldsymbol{E} = \boldsymbol{B} \times \boldsymbol{v}_{\mathrm{L}}$ is produced by Faraday's law. The movement of flux lines dissipates energy which can be modelled as a viscous drag force which balances with the $\boldsymbol{J} \times \boldsymbol{B}$ Lorentz force resulting in constant $\boldsymbol{v}_{\mathrm{L}}$. Thus, a non-zero electric field in a superconductor implies dissipation with work done of value $\boldsymbol{J} \times \boldsymbol{B} \cdot \boldsymbol{v}_{\mathrm{L}} = \boldsymbol{J} \cdot \boldsymbol{E}$. This means the electric field due to the movement of flux lines can be imagined as resulting from an effective resistivity, termed the flux-flow resistivity. The movement of these flux lines can be opposed by a pinning force produced by defects and inhomogeneities in the superconductor. Near these pinning centres, the superconducting order parameter is strongly depressed due to these defects making them ideal sites at which to locate a flux line. Pinning centres therefore exert an attractive interaction on the flux line. If the Lorentz force exceeds the pinning force, the flux lines can flow (known as flux flow). If the reverse is true, flux flow is forbidden, though there is a thermally activated process (known as flux creep) that can still occur. Both flux flow and flux creep lead to dissipation (because of the electric field associated with their movement) and therefore can contribute to a non-zero $\chi''$. Because of these processes, the a.c. response of type II superconductors is not solely dependent on frequency (an assumption that has been made for previous materials) but also depends on the strength of the d.c field and amplitude of the

a.c. field applied [34, 35, 98–103].

Several regimes can be considered when analysing the a.c. response of a type II superconductor. These are briefly mentioned here but more full descriptions can be found in [38]. Firstly, if a low amplitude a.c. field is applied with a larger d.c. field (such that $B_{\rm tot} \simeq B_{\rm d.c.}$) the flux lines can be found to be weakly pinned and the response due to their viscous motion is linear [35, 103]. This is the linear flux flow regime. When flux lines are no longer weakly pinned the a.c. response can be treated by considering the critical state (introduced by Bean [104]) in which the field gradient (related to the current density) takes its maximum value throughout the sample and the flux everywhere is on the point of slipping, though surface pinning can also be important [35, 103]. Here the response becomes nonlinear with an applied field $H(t) = H_{\rm a.c.}{\rm Im}({\rm e}^{i\omega t}) = H_{\rm a.c.}\sin\omega t$ yielding a magnetisation $M(t)$ of

$$\frac{M(t)}{H_{a.c.}} = \sum_{n=1}^{\infty} {\rm Im}(\chi_n {\rm e}^{i\omega t}), \tag{3.47}$$

where $\chi_n = \chi_n' - {\rm i}\chi_n''$ and $n$ represents the $n$th harmonic [98, 100–103]. Thus, $M(t)$ contains higher harmonics with the a.c. susceptibility considered up to this point ($\chi' - i\chi''$) being the first harmonic $\chi_1' - i\chi_1''$. Therefore, each harmonic may be extracted from

$$\chi_n' = \frac{1}{\pi H_{\rm a.c.}} \int_0^{2\pi} M(t)\sin(n\omega t)\,{\rm d}(\omega t) \tag{3.48}$$

$$\chi_n'' = -\frac{1}{\pi H_{\rm a.c.}} \int_0^{2\pi} M(t)\cos(n\omega t)\,{\rm d}(\omega t). \tag{3.49}$$

It should be noted that other conventions can be used (such as Appendix to [102]). The peak of $\chi''(T)$ can be associated with the irreversibility line of superconductors [98, 103, 105, 106]. In the linear regime there is a frequency dependence, but no dependence on the amplitude of $B_{\rm a.c.}$; in the critical state, the reverse is true but the critical current must be taken into account [103, 106].

The thermal activation of flux line motion was first treated by Anderson and Kim [107, 108] and models each pinning centre as a potential well of depth, $U$ [98, 99, 109]. $U$ depends on the spatial size of the pinned flux line (or bundle of flux lines) and the bulk critical field or critical current density [34]. The rate, $\nu$, at which a bundle may hop between pinning centres is given by

$$\nu = \nu_0 \exp\left[\frac{-(U-W)}{k_{\mathrm{B}}T}\right] - \nu_0 \exp\left[\frac{-(U+W)}{k_{\mathrm{B}}T}\right], \tag{3.50}$$

where $W$ is an adjustment to pinning potential height due to the Lorentz force acting on the pinned flux from the applied magnetic field and $\nu_0$ is a characteristic hopping rate [98, 99, 107–109]. The above equation represents forward and backward hopping between two wells which is either helped or hindered by the effect of the magnetic field. It can be rewritten as

$$\nu = \nu_0 \exp(-U/k_{\mathrm{B}}T) 2 \sinh(W/k_{\mathrm{B}}T), \tag{3.51}$$

where for $W \ll k_{\mathrm{B}}T$ this reduces to

$$\nu = 2\nu_0 \frac{W}{k_{\mathrm{B}}T} \exp(-U/k_{\mathrm{B}}T), \tag{3.52}$$

which looks like an Arrhenius law with a $1/T$-scaled prefactor [109]. The condition $W \ll k_{\mathrm{B}}T$ corresponds to the thermally activated flux flow regime. This is the situation of weakly pinned flux and can be observed at high temperatures with near constant applied magnetic fields (i.e. $B_{\mathrm{a.c.}} \ll B_{\mathrm{d.c.}}$) such that the current density does not vary greatly [109]. The opposite situation ($W \gg k_{\mathrm{B}}T$) is the flux creep regime in which the superconductor is in the critical state with $J \approx J_C$ [109]. Here the backward hopping term of Eq. 3.50 can be neglected due to the large $W$ [98, 99, 109] yielding a hopping rate

$$\nu = \nu_0 \exp\left[\frac{-(U-W)}{k_{\mathrm{B}}T}\right] \tag{3.53}$$

that is also of the Arrhenius form. The mechanism described above assumes an identical potential well at each pinning site though this is unlikely with the identification of the pinning sites as defects. A distribution of potential well heights is likely more realistic [100]. Nevertheless, as for SMMs and ferromagnets, $\chi''(T)$ can be measured at various frequencies in order to extract an effective activation energy (yielding $U$ or $U-W$, depending on the regime), as long as the amplitude of the d.c. and a.c. fields are appropriate for observing an Arrhenius dependence [99]. Moreover, the mutual repulsion of the vortices within a bundle of pinned vortices can also contribute to the breakdown of an Arrhenius type law at higher a.c. amplitudes [34].

In a typical frequency dependent a.c. measurement of a type II superconductor, $\chi'$ is expected to drop as temperature is lowered through $T_{\mathrm{c}}$ representing diamagnetic shielding while $\chi''$ should show a peak as temperature decreases (representing the point at which the a.c. magnetic field penetrates the centre of the sample) [35, 99, 106]. Both of these features are frequency dependent and have been observed in various type-II superconductors such as $(Ba_{0.6}K_{0.4})Fe_2As_2$ which can be seen in Fig. 3.16 [99] and $Na(Fe_{0.94}Ni_{0.06})_2As_2$ [98].

It is worth noting that a complicating factor in a.c. measurements of type II superconductors is due to the sample itself. Should the sample be polycrystalline (i.e. a powder or pellet) the diamagnetic drop of $\chi'$ with decreasing temperature can be considerably broader with a lower temperature hump while $\chi''$ can be dominated by a broad peak in addition to the much smaller peak below $T_{\mathrm{c}}$ we have associated with flux motion [34, 110–112]. In essence this is due to the sample showing two critical temperatures: one associated with the bulk superconductor (referred to as intrinsic peak) and one associated with coupling between grain boundaries (known as the lower coupling peak) [34, 110–112]. This means that the full diagmagnetic shielding of $\chi = -1$ cannot be reached at temperatures between these two $\chi''$ peaks [34, 110, 112]. It has been found

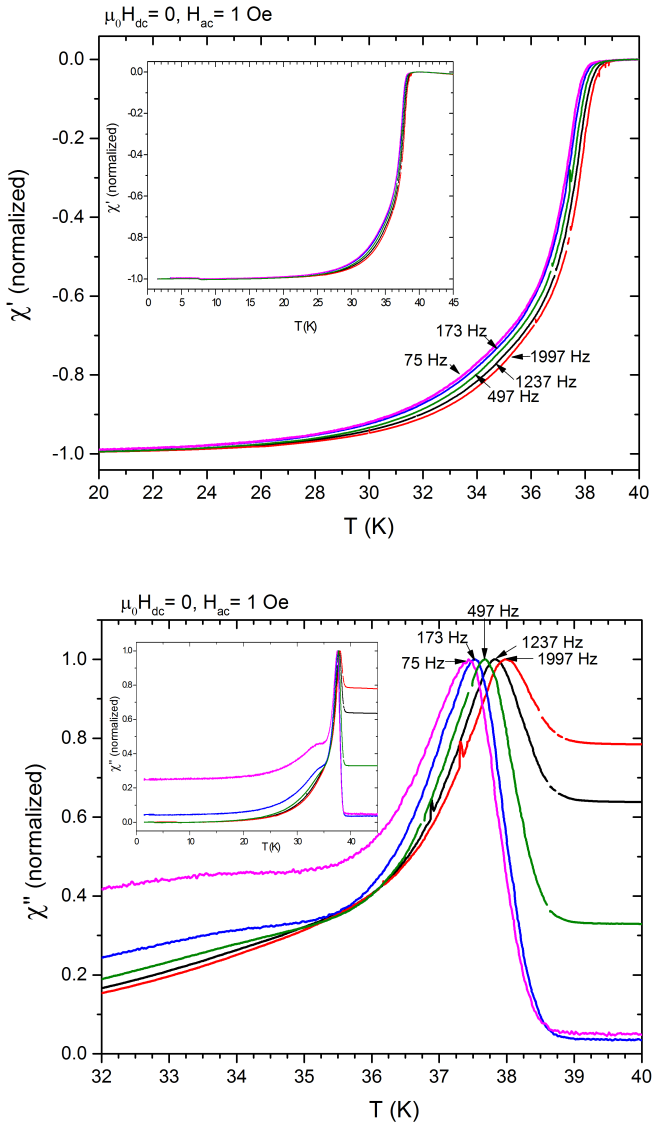



Figure 3.16: A.c. magnetic susceptibility of the superconductor $(Ba_{0.6}K_{0.4})Fe_2As_2$ from Ref. [99]. Upper/lower plot shows the real/imaginary parts of susceptibility with magnetic fields of $\mu_0 H_{\mathrm{d.\,c.}} = 0$ T and $\mu_0 H_{\mathrm{a.\,c.}} = 0.1$ mT focused on a temperature range around the frequency dependent portion of the data. Inset plots show the entire temperature range.

that this lower coupling peak is much more sensitive to the applied field than the intrinsic peak and in a high quality sample the two peaks may coincide for low measuring fields [112].

## 3.5 Conclusion

This section has served both to set out the principles of practical d.c. and a.c. magnetometry as well as provide an in depth discussion of the a.c. response from a theoretical background. The experimentally obtained a.c. response has subsequently been reviewed in various classes of compound demonstrating the utility of a.c. susceptibility in probing low frequency dynamics. While a powerful tool for identifying relaxation times and extracting energy barriers it has been shown that various systems can display very similar a.c. susceptibility profiles. Thus, like most measurement techniques, a.c. magnetic susceptibility must be employed with other complementary measurements.

# Chapter 4

# Studies of Two Families of Lanthanide-based Single-Molecule Magnets

## 4.1 Introduction

As stated in Chapter 3, single-molecule magnets show a rich a.c. magnetic response. Investigation of SMMs has, in part, been due to possible applications in information storage and quantum computing [113] and, in part, due to the academic interest of systems showing quantum effects [69, 113]. Their application to data storage is clear in light of their slow relaxing behaviour and analogy to superparamagnets described in Section 3.4.1. If $T_{\mathrm{B}}$ can be raised so that magnetisation is retained over long periods at everyday temperatures the small size of SMMs offers very dense information storage opportunities.

Therefore, a large research effort exists in the study of SMMs to raise the energy barrier to spin reorientation, $E_{\mathrm{a}}$. If the system is represented by the Hamiltonian shown in Eq. 3.42 (with $E = 0$ and $\boldsymbol{B} = 0$ for simplicity) then the height of the energy barrier is $E_{\mathrm{a}} = |DS^2|$ for integer $S$ and $E_{\mathrm{a}} = |D(S^2 - 1/4)|$ for half-integer $S$ [31, 69, 72, 114]. Total spin, $S$, is used in these definitions

rather than total angular momentum, $J$, since a great number of SMMs based on Mn and Fe have been studied [31, 69, 70, 113, 115] in which orbital quenching results in $L = 0$ and $J = S$. These relations are equally valid replacing $S$ with $J$. An obvious way to increase $E_{\mathrm{a}}$ is to increase one and/or both of its components, $S$ and $D$. However, it has been found that increasing $S$ often leads to a decrease of $D$ [70]. It is therefore important to synthesise and characterise new zero-dimensional molecular magnet families and examine why they do or do not display the slow magnetic relaxation of SMMs.

One approach to enhance $E_{\mathrm{a}}$ has been to utilise a larger number of magnetic ions in the core cluster in the hopes of enhancing the "giant spin" of each SMM [31, 70, 114]. However, to achieve high $S$ exchange between magnetic ions must be ferromagnetic but it is often the case that antiferromagnetic exchanges are also present complicating the system [31, 70, 72, 113]. It is clear that every additional magnetic ion introduced to a cluster adds ever increasing complex magnetic intracluster interactions (nearest neighbour and beyond). An alternative approach has been to not restrict synthesis to $d$ block transition metal but include the $4f$ block lanthanide ions [114, 116, 117]. As orbital quenching does not occur in these elements large total angular momentum, $J$, may be utilised in an effort to enhance $E_{\mathrm{a}}$. Furthermore, lanthanide ions may show high anisotropy which is also an attractive quality for SMM synthesis [114, 116, 117].

This chapter presents the magnetic characterisation of two families of lanthanide-based zero-dimensional magnets (referred to as the $Co_2Ln$ family and $Ni_4Ln_4$ family), some of which display slow magnetic relaxation. Work on the $Co_2Ln$ family was published in *Dalton Trans.*, 2016, **45**, 9235. Work on the $Ni_4Ln_4$ family was published in *Inorg. Chem.*, 2016, **55**, 8422. Magnetic measurements and analyses were performed in collaboration with J. Brambleby and P. A. Goddard. I would like to thank G. Stenning for use of the Quantum Design PPMS instrument in the Materials Characterisation Laboratory at the ISIS

Neutron and Muon Source.

## 4.2 The $Co_2Ln$ Family

A result of the large anisotropy and angular momenta associated with lanthanide ions means using them to construct SMMs can achieve slow magnetic relaxation with only a single metal ion possessing unpaired electrons [114, 117]. These single ion magnets (SIMs) are relatively easier to understand when compared with larger cluster SMMs since only one ion is responsible for their magnetic behaviour and so the giant spin formalism is correct. This removes any difficulties associated with the competing exchanges or temperatures where a single giant spin description breaks down.

The heterometallic trinuclear family $[Co_2^{III}Ln(L)_2(\mu\text{-}O_2CCH_3)_2(H_2O)_3]\cdot NO_3\cdot x\text{-}MeOH\cdot yH_2O$ for Ln = Gd ($x = 1$, $y = 1$), Tb ($x = 0$, $y = 2$), Ho ($x = 1$, $y = 1$) and Er ($x = 1$, $y = 1$) was characterised magnetically in order to elucidate the presence of any slow magnetic relaxation (or lack thereof). For brevity these compounds are referred to as $Co_2Ln$. In the chemical formula $LH_3$ is the multi-site compartmental ligand 2-methoxy-6-[2-(2-hydroxyethylamino)-ethyliminomethyl]phenol. Studies of other $3d$–$4f$ systems [118] have suggested that the inclusion of diamagnetic $3d$ ions may enhance SMM slow magnetic relaxation thus prompting the synthesis of this family with diamagnetic $Co^{3+}$ ions (as will be confirmed in the following d.c. magnetometry measurements). This work also functions as an extension to a previous study [54] which identified the Dy analogue as a SIM.

### 4.2.1 Experimental Methods

X-ray crystallography was performed using a Bruker SMART APEX CCD diffractometer equipped with an Oxford low-temperature attachment with further details found in Ref. [79]. D.c. magnetometry measurements were performed as detailed in Chapter 3 in a MPMS while a.c. magnetometry was performed in a

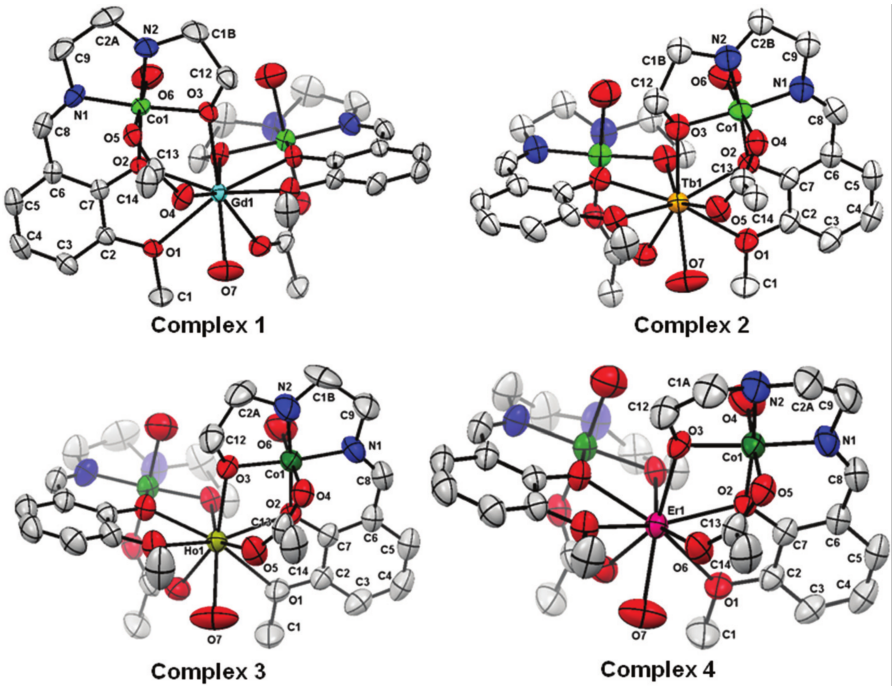



Figure 4.1: Structure of the $Co_2Ln$ family with Ln = $Gd^{3+}$ (1), $Tb^{3+}$ (2), $Ho^{3+}$ (3) and $Er^{3+}$ (4). Disordered parts, H atoms, anions and solvent molecules have been omitted for clarity. Gd = cyan, Tb = orange, Ho = yellow, Er = pink, Co = green, O = red, N = blue, C = light-grey.

MPMS and a PPMS. It was found to prevent sample movement during measurements powdered samples were required to be dispersed in Vaseline in standard gelatin capsules. Additionally, in order to avoid sample heating during measurements of the higher frequencies available in a PPMS a $45$ s wait time was included between each frequency in order to ensure temperature stability.

### 4.2.2 Synthesis and Structure

Synthesis and structural characterisation were performed by J. Goura, R. S. Narayanan, A. K. Bar and V. Chandrasekhar.

The synthesis of the $Co_2Ln$ family was performed by the sequential reaction of the ligand $LH_3$ (dissolved in methanol) with the appropriate lanthanide salt ($Ln(NO_3)_3{\cdot}H_2O$). This was then reacted with $Co(OAc)_2{\cdot}4H_2O$ and $Me_4NOH$ to yield the relevant $Co_2Ln$ compound as brown crystals to be measured via X-ray diffraction. For further detail of synthesis methods see Ref. [79].

Fig. 4.1 shows structural diagrams of each molecule found from single-crystal

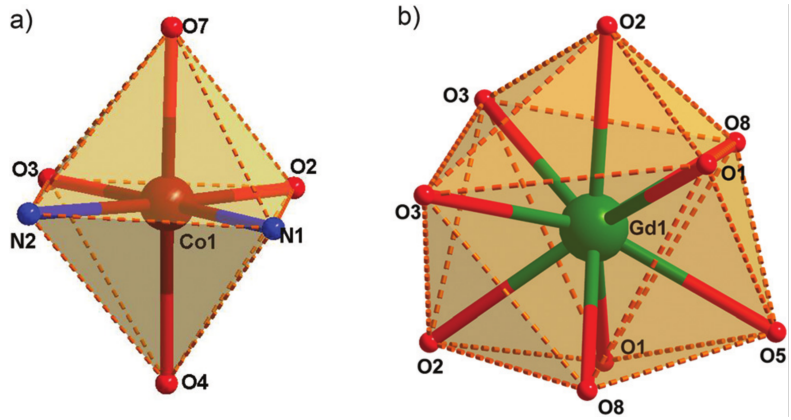



Figure 4.2: Example coordination environment for $Co_2Gd$ for each metal ion. (a) shows the distorted octahedron surrounding $Co^{3+}$ while (b) shows the distorted monocapped square anti-prism surrounding $Gd^{3+}$.

x-ray diffraction. These demonstrate that each complex is isostructural and that $Co_2Ln$ metallic core of each molecule consists of a bent geometry with different coordination environments between Co and Ln. Each molecule was found to be a monoclinic system with space group $C2/c$ with full details in Ref. [79]. Co can be observed to be coordinated in a distorted octahedron while Ln adopts a distorted monocapped square anti-prism coordination environment shown in Fig. 4.2 for $Co_2Gd$. This is particularly important for both $Co^{III}$ ions since they are expected to be in a $+3$ oxidation state. In an octahedral environment the ligand field splits the transition metal $t_{2g}$ and $e_g$ orbitals. For a $d^6$ transition metal with six outer electrons, if the effects of crystal field splitting are large compared to other energies (such as thermal energy) then the three lower $t_{2g}$ orbitals will be fully filled. Thus Co will be low spin. As a result each $Co^{III}$ ion will show zero angular momentum and all magnetic properties (beyond small diamagnetic effects) will be due to the $Ln^{III}$ ions. This is a requirement for heterometallic compounds such as the $Co_2Ln$ family to be SIMs rather than SMMs.

### 4.2.3 D.C. Magnetometry

Results of initial d.c. magnetometry measurements for each compound are shown in Fig. 4.3(a) and (b). The susceptibility results have been plotted as the product $\chi T$ since in the case of paramagnetic ions only Eq. 1.16 reduces to the constant,

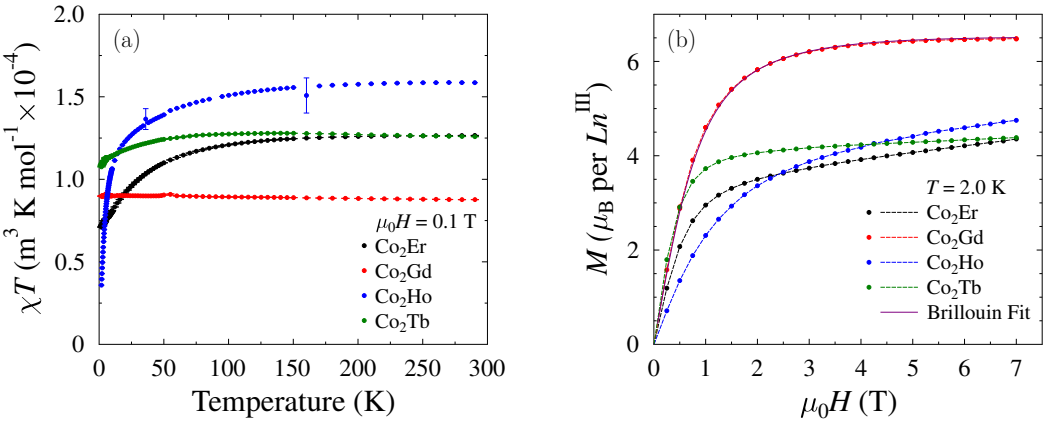



Figure 4.3: (a) The product of the molar susceptibility ($\chi = M/nH$ where $n$ is the number of moles of the sample) with $T$ vs. $T$. The applied magnetic field was $\mu_0 H_{\mathrm{d.c.}} = 0.1$ T and a ZFC sweep was performed. (b) $M$ vs. $\mu_0 H$ curves for each compound measured at $T = 2.0$ K. No hysteresis was detected between sweeping the magnetic field up or down thus only up sweeps are shown for clarity. A Brillouin fit to the $Co_2Gd$ $M$ v $H$ curve is also shown.

$$\chi T = \frac{N_{\mathrm{A}} \mu_0 \mu_{\mathrm{eff}}^2}{3 k_{\mathrm{B}}}, \tag{4.1}$$

where $N_{\mathrm{A}}$ is Avogadro's number (which equates to both the number of molecules per mole of a substance and for the $Co_2Ln$ family the number of magnetic moments per mole if only $Ln^{3+}$ contains unpaired electrons). Therefore, a perfectly paramagnetic compound shows a constant value of $\chi T$ as temperature is varied i.e. it is temperature-independent. This is directly proportional to $\mu_{\mathrm{eff}}^2$. Each compound shows a steady $\chi T$ for $T > 100$ K suggesting that each behaves as a paramagnet in this temperature range. Indeed the steady, high temperature $\chi T$ values for each compound lie within $10\%$ of the effective moment expected for only $Ln^{3+}$ ions with electron configurations and terms symbols $4f^7\ {}^8S_{7/2}$ ($Gd^{3+}$), $4f^8\ {}^7F_6$ ($Tb^{3+}$), $4f^{10}\ {}^5I_6$ ($Ho^{3+}$) and $4f^{11}\ {}^4I_{15/2}$ ($Er^{3+}$). This lends heavy support to the $Co^{3+}$ ions being in the low spin, $S = 0$ state and only the $Ln^{3+}$ ions possessing a magnetic moment. The slight variation from the expected $\mu_{\mathrm{eff}} = g_J \sqrt{J(J+1)}$ can be attributed to small diamagnetic effects from other parts of the molecules and errors in determining mass when dispersing the samples in Vaseline.

$Co_2Gd$ offers an excellent platform to further test the level of isolation of each molecule from one another. With half filled $f$-orbitals resulting in a ground state term symbol of ${}^8S_{7/2}$ with total orbital angular momentum of $L = 0$, free ion $Gd^{3+}$ shows a spherically symmetric electron distribution. The ability of lanthanide (or $f$ block) ions to possess a strong anisotropy arises from the interaction of the non-spherical electron distributions of the $f$ electrons and the crystal field created by the ligand environment [116]. Spherically symmetric $Gd^{3+}$ lacks this and therefore does not produce an anisotropy. Therefore it should show the behaviour of the $Co_2Ln$ family in absence of a non-zero $D$ with any deviation of $\chi T$ from a flat, horizontal line indicating a departure from paramagnetism and the presence of magnetic exchange between $Ln^{3+}$ ions. Intracluster exchange could also cause a deviation but this can be ruled out due to the $Co^{3+}$ ions being diamagnetic. Magnetic communication between $Ln^{3+}$ ions would suggest Eq. 1.27 would be a more appropriate description of susceptibility which does not show temperature independence when multiplied by $T$. Since $Co_2Gd$ remains approximately constant over the entire temperature range this suggests only very weak exchange can be present for the $Co_2Ln$ systems and magnetic features should indeed arise from only the isolated $Ln^{3+}$ and associated $D_{\mathrm{Ln}} \neq 0$.

Turning to $\chi T$ for the $Tb^{3+}$, $Ho^{3+}$ and $Er^{3+}$ compounds it can be seen that $\chi T$ of each begins to drop as temperature is lowered below approximately $100$ K. This can be attributed to the fact that each of these ions does not have a spherically symmetric $f$ electron distribution so will show a single ion anisotropy anisotropy due to interactions with the ligand field [116]. It has been suggested that this drop can be due to intermolecular interactions [118] though these can be ruled out due to the behaviour of the $Gd^{3+}$ analogue. In terms of the SMM Hamiltonian shown in Eq. 3.42 (in zero magnetic field and letting $E = 0$ for simplicity) this non-zero $D$ breaks the degeneracy of all $J_z$ states for isolated $Ln^{3+}$ ions. Thus, when thermal energy reaches the scale of $D$ thermal depopu-

Table 4.1: Comparison of obtained magnetisation of each compound at $\mu_0 H = 7\ \mathrm{T}$ with the saturation magnetisation for a given $Ln^{3+}$ ion.

| Sample | $g_J J$ ($\mu_B$) | $M(\mu_0 H = 7\ \mathrm{T})$ ($\mu_B$) |
|---|---|---|
| $Co_2Gd$ | 7 | 6.5 |
| $Co_2Tb$ | 9 | 4.4 |
| $Co_2Ho$ | 10 | 4.7 |
| $Co_2Er$ | 9 | 4.4 |

lation of higher energy $J_z$ levels occurs. Thus each of $Co_2Tb$, $Co_2Ho$ and $Co_2Er$ show non-zero $D$ (though this gives no indication if the anisotropy is easy axis or easy plane). The statement can be made that as $Er^{3+}$ possesses half-integer $J$ ($= 15/2$) it is a Kramers ion which requires a degeneracy of ground state energy levels [3, 6]. As such, $Co_2Er$ must contain an easy axis making it a strong candidate for SMM slow relaxation. This can be further supported by the similarity of $\chi T$ between $Co_2Er$ and the previously measured $Dy^{3+}$ analogue which was confirmed as a SIM [54].

The behaviour of $Co_2Gd$ as paramagnetic $Gd^{3+}$ can be further tested using the isothermal magnetisation at $2\ \mathrm{K}$ (Fig. 4.3(b)). This was fitted to Eq. 1.12, the magnetisation obeyed by an isolated paramagnet (known as a Brillouin fit), with $g_J = 2$ (since $L = 0$). This yielded $J = 3.262(3)$ in close agreement with the Hund's Rules ground state $J = 7/2$ reinforcing the conclusion that $Co_2Gd$ remains paramagnetic for the entire temperature range studied.

None of the remaining compounds show $M$ vs. $\mu_0 H$ curves which are fit by Eq. 1.12 as expected from the $\chi T$ data (i.e. they are not in the paramagnetic regimes). All show an initial rapid increase below approximately $2\ \mathrm{T}$ before easing off but still increasing. Importantly, none of these samples (excluding $Co_2Gd$) approach the predicted saturation magnetisation of their respective $Ln^{3+}$ ions ($M_\mathrm{S} = g_J J \mu_\mathrm{B}$) by a d.c. field of $7\ \mathrm{T}$ (shown in Tab. 4.1). This functions as further evidence for the presence of anisotropy in these compounds and demonstrates that it is of greater energy than $\sim g_J \mu_\mathrm{B} \boldsymbol{B} \cdot \boldsymbol{J}$ at $7\ \mathrm{T}$.

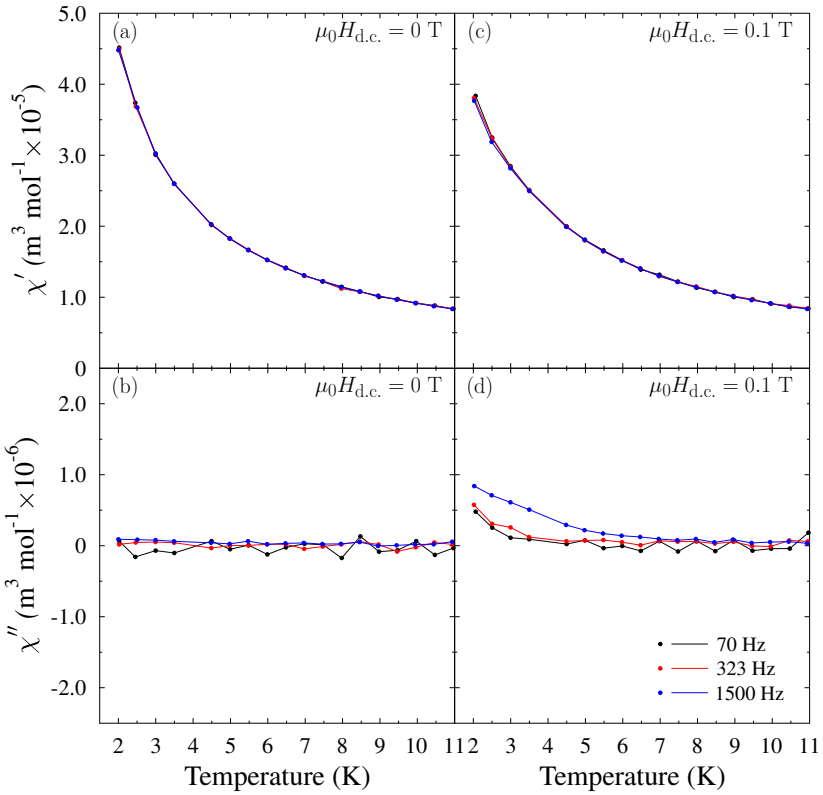



Figure 4.4: A.c. susceptibility (in-phase ((a)) and out-of-phase ((b)) components) of $Co_2Gd$ measured on cooling in $\mu_0 H_{\mathrm{d.c.}} = 0$ T with an a.c. field amplitude of $\mu_0 H_{\mathrm{a.c.}} = 0.4$ mT. A.c. susceptibility (in-phase ((c)) and out-of-phase ((d)) components) of $Co_2Gd$ measured on cooling in $\mu_0 H_{\mathrm{d.c.}} = 0.1$ T with an a.c. field amplitude of $\mu_0 H_{\mathrm{a.c.}} = 0.4$ mT. Only selected frequencies are shown for clarity.

### 4.2.4 A.C. Magnetometry

#### $Co_2Gd$

Fig. 4.4(a) and (b) show the a.c. susceptibility of $Co_2Gd$ in $\mu_0 H_{\mathrm{d.c.}} = 0$ T. $\chi'$ increases as temperature decreases with no visible frequency dependence. Furthermore, $\chi''$ remains zero at all measured frequencies and temperatures suggesting that the $Gd^{3+}$ ion indeed behaves as a paramagnet with no single-ion anisotropy. No slow magnetic relaxation has been detected with much greater frequencies being required to probe the spin-spin relaxation time as described in Section 3.4.5.

A d.c. magnetic field of $\mu_0 H_{\mathrm{d.c.}} = 0.1$ T was applied and the measurement

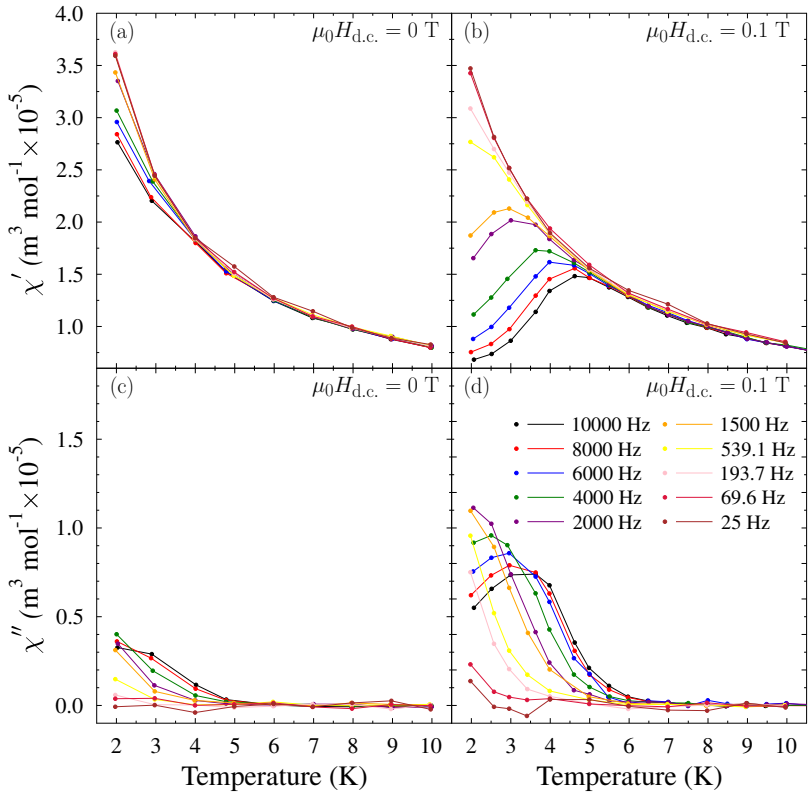



Figure 4.5: A.c. susceptibility (in-phase ((a)) and out-of-phase ((b)) components) of $Co_2Er$ measured on cooling in $\mu_0 H_{\mathrm{d.c.}} = 0$ T with an a.c. field amplitude of $\mu_0 H_{\mathrm{a.c.}} = 0.4$ mT. A.c. susceptibility (in-phase ((c)) and out-of-phase ((d)) components) of $Co_2Er$ measured on cooling in $\mu_0 H_{\mathrm{d.c.}} = 0.1$ T with an a.c. field amplitude of $\mu_0 H_{\mathrm{a.c.}} = 0.4$ mT.

repeated to check for the possibility of field-induced SMM behaviour (Fig. 4.4(c) and (d)). $\chi'$ shows the same behaviour as for $\mu_0 H_{\mathrm{d.c.}} = 0$ T with a very slight depression of magnitude visible at the lowest temperatures. Similar to the zero d.c. field case, no clear frequency separation of data has been induced except for perhaps a very slight change at low temperatures. The out-of-phase data becomes weakly non-zero below $\sim 6$ K with higher frequencies increasing first. This suggests a very weak slow magnetic relaxation induced by the d.c. field. This matches the expected effect of a d.c. magnetic field causing a net magnetisation in a paramagnet and opening up the possibility of spin-lattice relaxation as described in Section 3.4.5 [31].

**$Co_2Er$**

The a.c. susceptibility of $Co_2Er$ at zero applied d.c. field is shown in Fig. 4.5(a) and (b). The real part increases as temperature is lowered and begins to separate based on a.c. measuring frequency below $\sim 4$ K. Higher frequency measurements can be observed to drop in magnitude at higher temperatures, typical of a substance showing slow magnetic relaxation. $\chi''$ also shows frequency dependence, deviating from zero below $\sim 5$ K with higher frequencies rising first further demonstrating the presence of slow magnetic relaxation. Additionally, the highest measured frequencies of $\chi''$ appear to drop below lower frequencies at $2$ K. This is evocative of these frequencies being just above the temperature of a peak in $\chi''(T)$ and therefore the condition $\omega\tau(T) = 1$.

Applying a d.c. field of $\mu_0 H_{\mathrm{d.c.}} = 0.1$ T results in an enhancement of slow magnetic relaxation as shown in Fig. 4.5(c) and (d). In this applied field, the frequency dependence of $\chi'$ is much clearer with all but the lowest frequencies showing a peak (the peaks of higher frequencies occurring at higher temperatures). The imaginary part of susceptibility similarly shows several unambiguous peaks for the higher frequency measurements ($\nu \geq 3000$ Hz), suggestive of SMM behaviour.

These measurements of zero d.c. field and non-zero d.c. field a.c. behaviour offer strong evidence of $Co_2Er$ being a field-induced SIM with SMM slow magnetic relaxation being suppressed at zero field due to the presence of quantum tunnelling. This is further supported by comparison with the previously reported $Dy^{3+}$ analogue (also identified as a field-induced SMM) [54]. Both are Kramers ions [3, 6] necessitating a degenerate ground state (therefore are easy axis rather than easy plane) and show similar a.c. responses (see Fig. 3.9) [54].

Evaluation of the suitability of the Debye model to this compound was performed by creating a Cole-Cole plot of a.c. data in $\mu_0 H_{\mathrm{d.c.}} = 0.1$ T (Fig. 4.6(a)). As temperature is lowered data can be observed to begin to trace single isother-

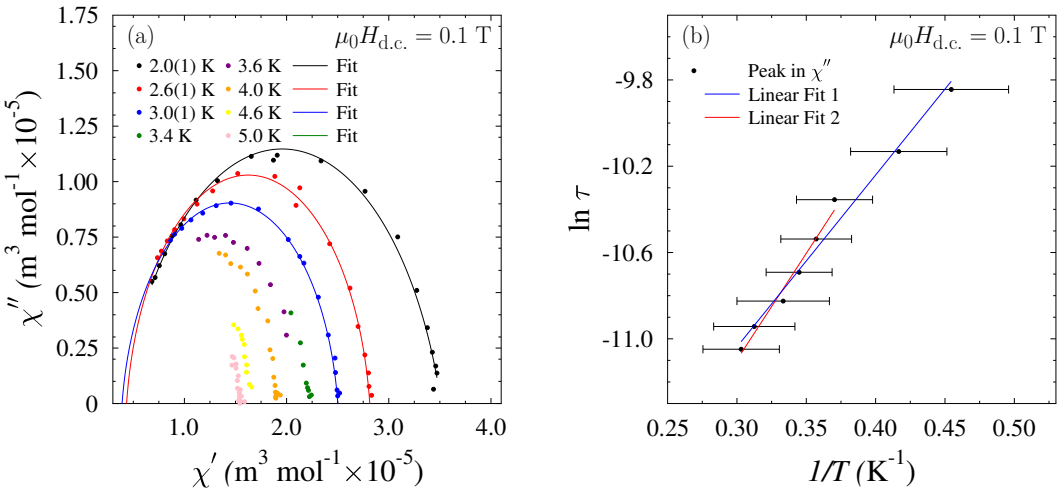



Figure 4.6: (a) Cole-Cole plot ($\chi''$ v. $\chi'$) of a.c. susceptibility in $\mu_0 H_{\rm d.c.} = 0.1$ T. Fits to Eq. 3.38 are also shown. Temperature stability problems occurred for $2 \leq T \leq 3$ K though this variation was minimised to $\pm 100$mK. (b) Plot of $\ln \tau$ v. $1/T$ for $Co_2Er$ in a magnetic field of $\mu_0 H_{\rm d.c.} = 0.1$ T. This assumes that the condition $\omega\tau = 1$ has been reached in Fig. 4.5(d) at each peak in $\chi''$. These points were selected as satisfying $\mathrm{d}\chi''/\mathrm{d}T = 0$.

mal arcs as predicted by the generalised Debye model, suggestive of a single relaxation pathway. Therefore, the lowest temperatures (and most complete arcs) were fit to Eq. 3.38 [55]. These yielded good fits to the data with a near constant $\chi_S$ ($x$-axis intercept) at an average value of $\chi_S = 0.42(2) \times 10^{-5}$ m$^3$ mol$^{-1}$. Furthermore, the value of $\alpha$ varies from $0.2$ to $0.1$ for $2 \leq T \leq 3$ K suggesting a small spread of relaxation times. Notably, $\alpha$ actually increases with decreasing temperature (i.e. the spread of relaxation times increases with decreasing temperature). This is suggestive of other relaxation mechanisms becoming important (such as quantum tunnelling) at low temperatures.

Thus, it appears valid to model the slow magnetic relaxation of $Co_2Er$ as a Orbach process following an Arrhenius expression. Therefore, the peaks of $\chi''$ were selected as satisfying the condition $2\pi\nu\tau = 1$ and plotted as shown in Fig. 4.6(b). An Arrhenius relationship can be linearised in the form of,

$$\ln \tau = \ln \tau_0 + \frac{E_{\rm a}}{k_{\rm B} T}, \tag{4.2}$$

allowing the data shown in Fig. 4.6(b) to be fit to a straight line. As discussed

Table 4.2: Results of linear fits shown in Fig. 4.6(b) to Eq. 4.2 for $Co_2Er$.

| Fit | $\ln \tau_0$ | $\tau_0$ (s) | $E_a/k_B$ (K) |
|---|---|---|---|
| Linear Fit 1 | $-14.1(3)$ | $\approx 8 \times 10^{-7}$ | $9.9(8)$ |
| Linear Fit 2 | $-13.4(2)$ | $\approx 2 \times 10^{-6}$ | $8.0(5)$ |

in Section 3.4.1 the Orbach process governs the Arrhenius-type relaxation for SMMs. Since this involves high energy phonons it would be expected to be dominant at higher temperatures. As such, at low temperatures other non-phonon assisted mechanisms may become important such as quantum tunnelling of magnetisation. To test this possibility two linear fits were performed, one over the entire temperature range and one for $T > 2.5$ K (results shown in Tab. 4.2). This shows that fitting data over only the high temperature (low $1/T$) region yields a slightly steeper gradient and therefore higher $E_a$ suggesting data are not exactly linear. Since a temperature independent process such as quantum tunnelling yields a flat region of a $\ln \tau$ vs. $1/T$ (see, for example, Fig. 3.7(b)) while an Arrhenius law governed region should be linear it appears that this data lies in an intermediate region where Arrhenius relaxation and quantum tunnelling are in competition. This means only limited quantitative conclusions may be drawn from the measured data with higher a.c. frequencies being required to properly map out a region of Arrhenius dominated relaxation. Therefore, bounds can be stated of $\tau_0 \leq 8 \times 10^{-7}$ s and $E_a/k_B \geq 9.9(8)$ K.

**$Co_2Tb$**

Difficulties encountered in finding a region of strong frequency dependence in $Co_2Tb$ prompted a study of a.c. susceptibility as d.c. field was varied. This is shown in Fig. 4.7(a) and (b). While a clear frequency dependence and reduction from the zero field value exists at $\mu_0 H_{d.c.} = 0.1$ T in $\chi'$ (left dashed line in Fig. 4.7(a)) only the maximum applied frequency is shown to have peaked in $\chi''$ upon reaching this d.c. field (left dashed line in Fig. 4.7(b)). As these plots show data at the minimum measurement temperature, they also represent the maximum relaxation time $Co_2Tb$ may adopt in the measured temperature range

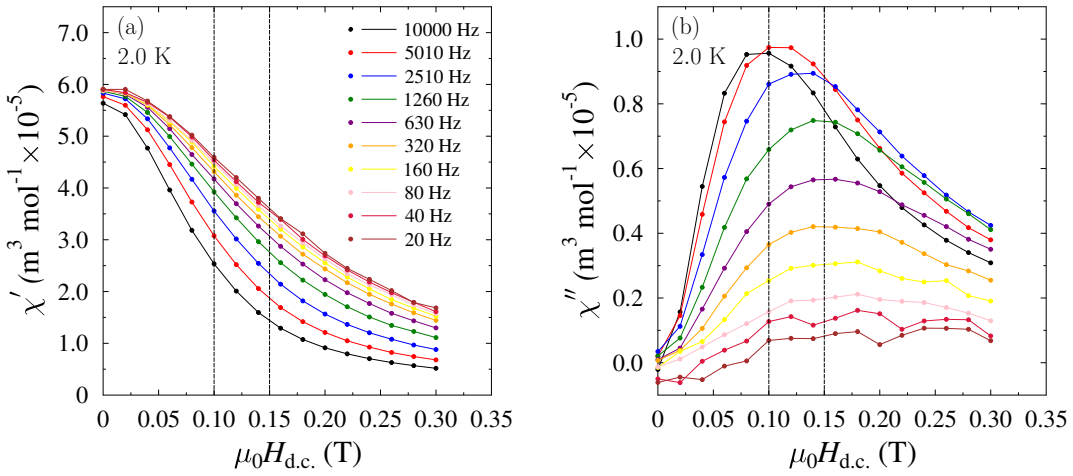



Figure 4.7: Study of d.c. magnetic field dependence of a.c. susceptibility of $Co_2Tb$ at $2.0$ K and an a.c. amplitude of $\mu_0 H_{a.c.} = 0.4$ mT. (a) In-phase a.c. susceptibility of $Co_2Tb$ at $2.0$ K. (b) Out-of-phase susceptibility of $Co_2Tb$ at $2.0$ K. Dashed lines highlight the typical d.c. magnetic field employed to test for field-induced SMM behaviour ($\mu_0 H_{\mathrm{d.c.}} = 0.1$ T, left) and the used magnetic field for $Co_2Tb$ ($\mu_0 H_{\mathrm{d.c.}} = 0.15$ T, right).

assuming $\tau$ increases as temperature is decreased (as is true for SMMs). Therefore, to allow a sufficient number of frequencies to fulfil the condition $\omega\tau(T) = 1$ and evaluate SMM behaviour a d.c. measurement field must be chosen such that a number of $\chi''(\mu_0 H_{\mathrm{d.c.}})$ peaks have occurred below this field. This is a rough requirement to allow peaks in $\chi''(T)$ to be visible at temperatures higher than $2.0$ K (the minimum measurement temperature). At $\mu_0 H_{\mathrm{d.c.}} = 0.15$ T (right dashed lines in Figs. 4.7(a) and (b)) a number of peaks in $\chi''$ can be observed to have occurred at lower fields while a strong $\chi''$ signal remains. Therefore measurements were performed sweeping temperatures in both $\mu_0 H_{\mathrm{d.c.}} = 0$ and $0.15$ T.

In zero applied d.c. magnetic field, $\chi'$ (Fig. 4.8(a)) increases monotonically on cooling with little to no evidence of frequency separation except perhaps very slightly at $2.0$ K. The out-of-phase component (Fig. 4.8(b)) remains unambiguously zero throughout the measured temperature range. When applying the chosen d.c. magnetic field of $\mu_0 H_{\mathrm{d.c.}} = 0.15$ T a large frequency dependence is induced. As shown in Fig. 4.8(c) $\chi'$ shows a frequency separation below

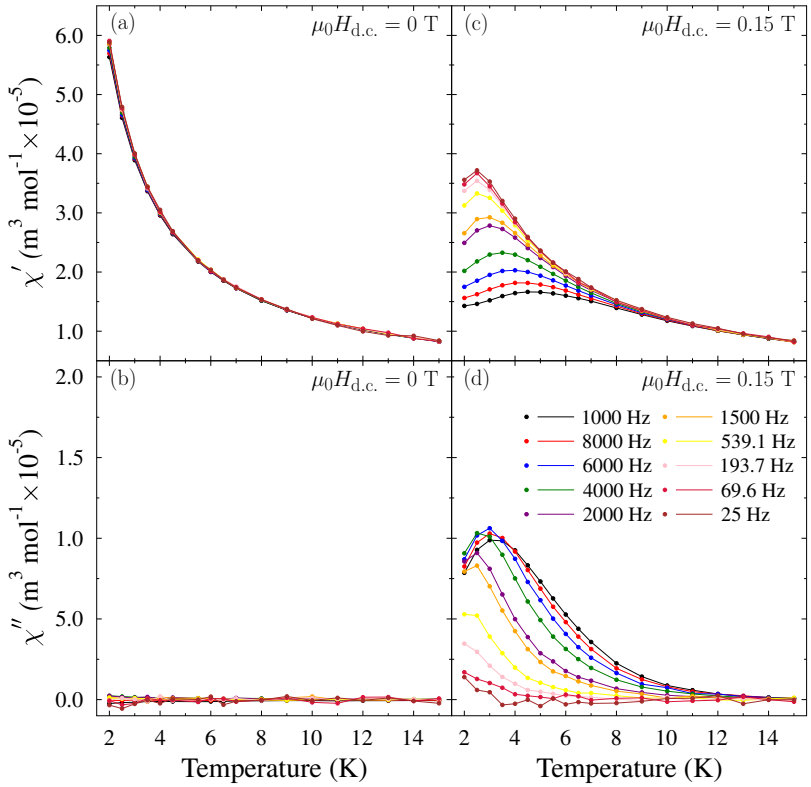



Figure 4.8: A.c. susceptibility (in-phase ((a)) and out-of-phase ((b)) components) of $Co_2Tb$ measured on cooling in $\mu_0 H_{\mathrm{d.c.}} = 0$ T with an a.c. field amplitude of $\mu_0 H_{\mathrm{a.c.}} = 0.4$ mT. A.c. susceptibility (in-phase ((c)) and out-of-phase ((d)) components) of $Co_2Tb$ measured on cooling in $\mu_0 H_{\mathrm{d.c.}} = 0.15$ T with an a.c. field amplitude of $\mu_0 H_{\mathrm{a.c.}} = 0.4$ mT.

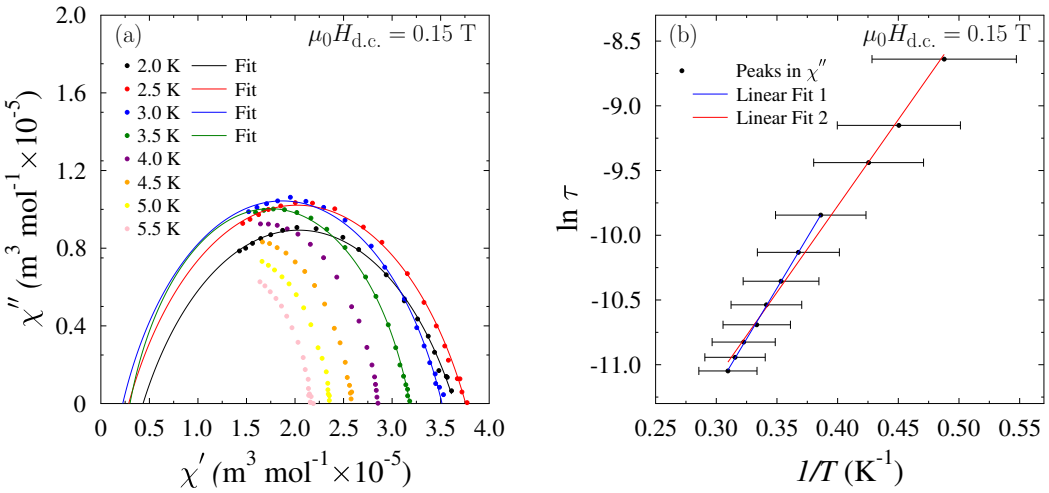



Figure 4.9: (a) Cole-Cole plot of a.c. data of $Co_2Tb$ in $\mu_0 H_{\mathrm{d.c.}} = 0.15$ T with an a.c. amplitude of $\mu_0 H_{\mathrm{d.c.}} = 0.4$ mT. Data were found to be reproducible in an a.c. amplitude of $\mu_0 H_{\mathrm{d.c.}} = 0.1$ mT indicating sample heating was not encountered. Fits to Eq. 3.38 are also shown. (b) Plot of $\ln \tau$ v. $1/T$ for $Co_2Tb$ in a magnetic field of $\mu_0 H_{\mathrm{d.c.}} = 0.15$ T. This assumes that the condition $\omega\tau = 1$ has been reached in Fig. 4.8(d) at each peak in $\chi''$. These points were selected as satisfying $\mathrm{d}\chi''/\mathrm{d}T = 0$.

Table 4.3: Results of fits shown in Fig. 4.9(a) to Eq. 3.38 for $Co_2Tb$.

| $T$(K) | $\chi_S$ (m$^3$mol$^{-1}$ $\times$ 10$^6$) | $\chi_T$ (m$^3$ mol$^{-1}$ $\times$ 10$^6$) | $\alpha$ (K) |
|---|---|---|---|
| 3.5 | 3.0(4) | 3.183(8) | 0.226(6) |
| 3.0 | 2.3(10) | 3.514(9) | 0.28(2) |
| 2.5 | 2.9(5) | 3.758(6) | 0.323(9) |
| 2.0 | 4.3(4) | 3.644(8) | 0.35(1) |

$\sim 10$ K and develops frequency dependent peaks, higher frequencies showing higher temperature peaks. $\chi''$ becomes non-zero and frequency dependent below $\sim 12$ K as shown in Fig. 4.8(d). Furthermore, a series of frequency-dependent peaks have been induced by the d.c. field (higher frequencies peaking at higher temperatures). This behaviour is reminiscent of both $Co_2Er$ and the previously measured $Co_2Dy$ [54] suggesting $Co_2Tb$ is also a field-induced SIM.

To investigate SMM behaviour, a Cole-Cole plot of a.c. susceptibility in $\mu_0 H_{\mathrm{d.c.}} = 0.15$ T was constructed. Shown in Fig. 4.9(a), isothermal arcs are evident and as temperature decreases the size of these arcs increases for $T > 2.5$ K. This shows further similarity between $Co_2Tb$ and $Co_2Er$ and $Co_2Dy$ [54]. However, below this temperature range the arcs actually contract. To investigate this behaviour further, the four lowest temperature arcs were fit to Eq. 3.38 with the fit

Table 4.4: Results of linear fits shown in Fig. 4.9(b) to Eq. 4.2 for $Co_2Tb$.

| Fit | $\ln \tau_0$ | $\tau_0$ (s) | $E_a/k_B$ (K) |
|---|---|---|---|
| Linear Fit 1 | $-15.9(1)$ | $\approx 1 \times 10^{-7}$ | $15.6(4)$ |
| Linear Fit 2 | $-15.1(1)$ | $\approx 3 \times 10^{-7}$ | $13.3(3)$ |

parameters shown in Tab. 4.3. The distribution of relaxation times ($\alpha$) increases on cooling suggestive of another relaxation method becoming important. This is likely quantum tunnelling given the effect of an applied d.c. magnetic field observed in Fig. 4.7 and Fig. 4.8. Attempts to extract the energy barrier to magnetic moment reorientation are shown in Fig. 4.9(b) following the same method as for $Co_2Er$. Similar to $Co_2Er$, fits to Eq. 4.2 were performed over only the high temperature range and over the entire temperature range. Again, it can be seen that the data is not entirely linear with each fit predicting a different gradient (and therefore $E_a$). Gradient is reduced by including lower temperature (high $1/T$) points in the fit suggesting another relaxation mechanism is becoming pertinent as it competes with thermal relaxation. As such, it appears that a similar situation to $Co_2Er$ has been encountered in which to reach a regime where thermal relaxation dominates over quantum tunnelling higher measurement frequencies would be required to fulfil the $\omega\tau = 1$ condition at higher temperatures. Therefore, similar limits are placed on the quantitative results which can be drawn. $Co_2Tb$ is thus identified as a field-induced SIM with $\tau_0 \leq 3 \times 10^{-7}$ s and $E_a/k_B \geq 15.6(4)$ K based on the high temperature fit of Fig. 4.9(b) which will be less susceptible to the onset of alternate relaxation mechanisms.

It can be queried why $Co_2Tb$ may behave as an SMM (even if the behaviour is field induced). As a Kramers ion, $Er^{3+}$ was expected to show the bistable ground state [3, 6] required of the easy axis possessed by SMMs. Thus, it was expected that the non-zero $D$ of that lanthanide ion would be positive in the formalism of Eq. 3.42. $Tb^{3+}$ with $J = 6$ is a non-Kramers ion so another source facilitating the easy axis is required. This can be provided by an axial ligand field around $Tb^{3+}$ allowing a doubly degenerate ground state [116]. In the unit cell of $Co_2Tb$, the

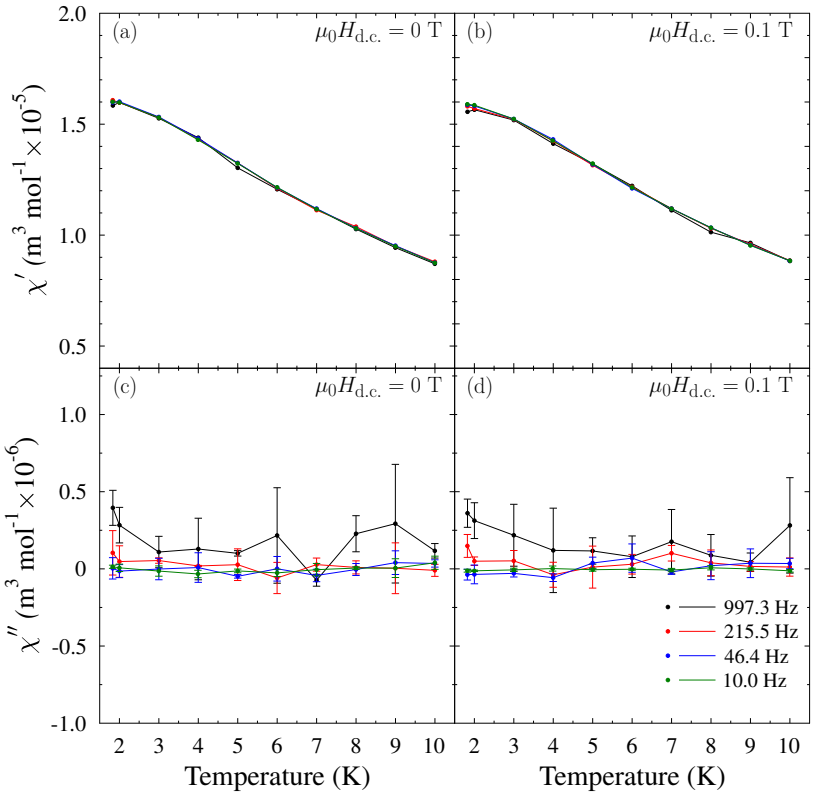



Figure 4.10: A.c. susceptibility (in-phase ((a)) and out-of-phase ((b)) components) of $Co_2Ho$ measured on cooling in $\mu_0 H_{\rm d.c.} = 0$ T with an a.c. field amplitude of $\mu_0 H_{\rm a.c.} = 0.4$ mT. A.c. susceptibility (in-phase ((c)) and out-of-phase ((d)) components) of $Co_2Ho$ measured on cooling in $\mu_0 H_{\rm d.c.} = 0.1$ T with an a.c. field amplitude of $\mu_0 H_{\rm a.c.} = 0.4$ mT.

$Tb^{3+}$ ions have a point group of $2$ thus providing axial (or twofold rotational) symmetry and allowing a bistable ground state.

**$Co_2Ho$**

A.c. susceptibility in zero d.c. magnetic field of the last member of this family ($Co_2Ho$) is shown in Fig. 4.10(a) and (b). $\chi'$ increases on cooling appearing to level off at the lowest measured temperatures. No frequency separation is visible except perhaps an extremely small separation at base temperature (though this is not certain). Similarly, $\chi''$ remains zero throughout the temperature range except for perhaps a very small upturn for $T < 3$ K (higher frequencies rising most). It should be noted that the out-of-phase signal is about two orders of magnitude less than the in-phase signal. These observations suggest at $\mu_0 H_{\rm d.c.} = 0$ T $Co_2Ho$ does not show slow magnetic relaxation. Furthermore, on applying a $0.1$ T d.c.

Table 4.5: Unique Ln–O distances for each member of the $Co_2Ln$ family with each unique distance labelled as in Fig. 4.11. $Co_2Dy$ data from Ref. [54].

| | $Ln^{3+}$–O (Å) | | | | |
|---|---|---|---|---|---|
| O Label | $Gd^{3+}$ | $Tb^{3+}$ | $Ho^{3+}$ | $Er^{3+}$ | $Dy^{3+}$ |
| (a) | 2.398(5) | 2.383(9) | 2.388(6) | 2.361(6) | 2.38(1) |
| (b) | 2.360(3) | 2.334(6) | 2.316(3) | 2.312(3) | 2.329(8) |
| (c) | 2.687(3) | 2.699(6) | 2.700(3) | 2.706(3) | 2.674(9) |
| (d) | 2.3893 | 2.370(6) | 2.353(3) | 2.338(3) | 2.373(7) |
| (e) | 2.385(2) | 2.374(6) | 2.352(2) | 2.347(3) | 2.361(5) |
| Average | 2.444 | 2.432 | 2.422 | 2.410 | 2.43 |

field (Figs. 4.10(c) and (d)) no appreciable change is observed for both $\chi'$ and $\chi''$ indicating quantum tunnelling is not obscuring a thermally activated relaxation. Thus, $Co_2Ho$ does not display SMM behaviour.

To reconcile this observation of no slow magnetic relaxation with $D \neq 0$ (as shown by d.c. measurements of this compound) $Co_2Ho$ may be compared with $Co_2Tb$. Like $Tb^{3+}$, $Ho^{3+}$ is a non-Kramers ion so does not require a degenerate ground state. While $Co_2Tb$ showed $D > 0$ and so a degenerate ground state and slow magnetic relaxation, $Co_2Ho$ appears to possess $D < 0$ which must be of a comparable value to that for $Co_2Er$ and $Co_2Tb$ due to similar d.c. magnetic properties observed. For $D < 0$ the double well potential of SMMs (Fig. 3.8) is instead a single potential well with a $J_z = 0$ non-degenerate ground state. In such a system, slow magnetic relaxation would not be expected even in an applied d.c. field assuming the $J_z = 0$ ground state is well separated from the first excited states compared to the Zeeman energy in the applied d.c. field. This assumption is supported by the $M$ vs. $\mu_0 H$ curve at $2\ \mathrm{K}$ (see Fig. 4.3(b)) where at $\mu_0 H_{\mathrm{d.c.}} = 0.1\ \mathrm{T}$ $M$ is well within the initial rapid increase which lasts for several $\mathrm{T}$. Such lack of slow magnetic relaxation has been observed in other $D < 0$ non-Kramers ions [119].

### 4.2.5 Origin of Lanthanide Anisotropy

While $Co_2Er$ and $Co_2Tb$ have been identified as field-induced SIMs (analogous to $Co_2Dy$) and $Co_2Ho$ has been shown to adopt a $J_z = 0$ ground state. The origin of

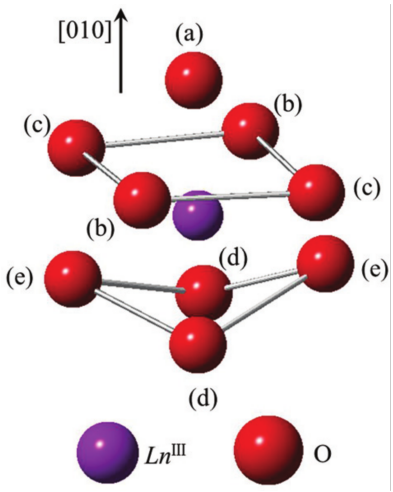



Figure 4.11: The monocapped distorted square anti-prism coordination environment of the $Ln^{3+}$ ions as shown in Fig. 4.2(b) for $Co_2Gd$ but focusing on unique oxygen atoms. The twofold rotation axis ($[010]$) shows that there are five unique Ln–O distances labelled (a)–(e).

the single-ion anisotropies in these compounds can be rationalised when considering their ligand environment. For completeness, $Co_2Dy$ with $E_a/k_B = 88(8)$ K [54] may also be considered.

Firstly, each of these compounds is isostructural (as stated in Section 4.2.2) with the $Ln^{3+}$ ion existing in a near identical ligand environment between each compounds. Indeed, the monocapped square anti-prisms constructed of the central $Ln^{3+}$ and chelating O (shown in Fig. 4.2(b) for $Co_2Gd$ and alternately depicted in Fig. 4.11) shows little variation of Ln-O bond distances (Tab. 4.5). Thus, differences in single-ion anisotropy must primarily arise from the interaction between the $4f$ electron density and the positioning of the ligand field [116].

$Dy^{3+}$ and $Tb^{3+}$ show oblate free-ion electron densities, $Ho^{3+}$ weakly oblate, $Er^{3+}$ weakly prolate and $Gd^{3+}$ spherically symmetric [116]. A high $J_z$ ground state will be favoured for a ligand environment which minimises contact between the ligand field and $4f$ electron density. Thus $Co_2Gd$ shows no anisotropy and no slow magnetic relaxation. The monocapped anti-prism ligand environment (Fig. 4.11) corresponds to a sandwich type coordination which has been known to promote $D > 0$ (or, in other words, promote high $|J_z|$ degenerate ground

states) for lanthanide ions of oblate electron densities [116]. Therefore, the $Dy^{3+}$ and $Tb^{3+}$ analogues would be expected to show the strongest SIM properties (evidenced as possessing the highest energy barriers to spin reorientation) which has been the situation observed. The fact the $Dy^{3+}$ analogue appears to show the higher energy barrier of the two is likely an effect of $Dy^{3+}$ also being a Kramers ion further ensuring a degenerate ground state. While it was previously argued that the point group of $2$ allows a uniaxial anisotropy and so SIM behaviour, this low-symmetry environment appears to promote only a small anisotropy thus $Co_2Tb$ showing a lower energy barrier than $Co_2Dy$ which has been enhanced by $Dy^{3+}$ being a Kramers ion.

Since the $Ho^{3+}$ and $Er^{3+}$ analogues are only weakly oblate and prolate respectively it would be expected for them to display weaker anisotropies than their $Dy^{3+}$ and $Tb^{3+}$ counterparts. $Co_2Er$ follows this trend with SIM behaviour displaying an apparently smaller energy barrier than the $Dy^{3+}$ and $Tb^{3+}$ analogues. Furthermore, the prolate electron density of the $Er^{3+}$ ion would be expected to promote an easy plane rather than a easy axis anisotropy in this ligand environment [116]. The SIM behaviour of this compound likely primarily originates from its Kramers ion nature. However, since $Co_2Ho$ has shown $D < 0$ this suggests this ligand environment either does not strongly promote anisotropy or the non-spherically symmetric electron density of $Ho^{3+}$ is particularly weak here.

### 4.2.6 Conclusion

The magnetic behaviour of the isostructural zero-dimensional molecular magnet family $[Co^{III}_2Ln(L)_2(\mu\text{-}O_2CCH_3)_2(H_2O)_3]\cdot NO_3\cdot x MeOH\cdot y H_2O$ for Ln = Gd ($x = 1$, $y = 1$), Tb ($x = 0$, $y = 2$), Ho ($x = 1$, $y = 1$) and Er ($x = 1$, $y = 1$) was elucidated. D.c. magnetometry showed each to contain a non-zero anisotropy except for the $Gd^{3+}$ analogue which was well modelled as a paramagnetic $Gd^{3+}$ ion. This confirmed both that the magnetic behaviour of the other compounds was primarily due to their respective $Ln^{3+}$ ion and no appreciable intermolecule

exchange was present.

A.c. magnetometry showed the Kramers ion containing $Co_2Er$ to show strong evidence of field-induced SIM slow magnetic relaxation that was suppressed at zero applied d.c. magnetic field due to quantum tunnelling. Application of a d.c. field of $\mu_0 H_{\mathrm{d.c.}} = 0.1\ \mathrm{T}$ suppressed quantum tunnelling with thermal relaxation becoming the dominant relaxation pathway allowing an energy barrier to magnetic moment reorientation to be estimated as $E_{\mathrm{a}}/k_{\mathrm{B}} \geq 9.9(8)\ \mathrm{K}$. Similarly, the non-Kramers ion containing $Co_2Tb$ was also found to be a field-induced SIM with an estimated $E_{\mathrm{a}}/k_{\mathrm{B}} \geq 15.6(4)\ \mathrm{K}$. $Co_2Ho$ did not show evidence of slow relaxation suggesting it contained an easy plane anisotropy with a $J_z = 0$ ground state that did not relax via quantum tunnelling or thermal processes. The a.c. response of $Co_2Gd$ was found to be consistent with a paramagnetic ion with zero single-ion anisotropy.

## 4.3 The $Ni_4Ln_4$

In contrast to the $Co_2Ln$ family in which magnetic properties originated only from the $Ln^{3+}$ ion, lanthanide-based zero-dimensional magnets can be constructed with many more magnetic ions in the core metal cluster (lanthanide and transition metal both) [114, 116, 117]. This introduces further complexity not only due to the difficulties already possessed by transition metal only SMMs of maintaining both the correct anisotropies and exchange to ensure large angular momenta [70] but also due to the unique problems associated with the lanthanides, an example being the discovery that their exchange is better mediated by radicals [120]. As a result, lanthanide ions can be mixed with magnetic $3d$ ions in an effort to improve this exchange and hopefully yield SMM slow relaxation with larger energy barriers to spin reorientation and so longer relaxation times at higher temperatures.

Thus, the prospective heterobimetallic SMM family based on lanthanide and

nickel ions, $[Ln_4Ni_4(H_3L)_4(\mu_3\text{-}OH)_4(\mu_2\text{-}OH)_4]4Cl{\cdot}xH_2O{\cdot}yCHCl_3$ with $Ln^{3+}$ = $Dy^{3+}$ ($x = 30.6$, $y = 2$), $Tb^{3+}$ ($x = 28$, $y = 0$), $Gd^{3+}$ ($x = 25.3$, $y = 0$) and $Ho^{3+}$ ($x = 30.6$, $y = 3$), was studied. The ligand L is defined as $H_5L$ = $N_1, N_3$-bis(6-formyl-2-(hydroxymethyl)-4-methylphenol)diethylenetriamine. These four compounds were characterised magnetically with each compound henceforth referred to as $Ni_4Dy_4$, $Ni_4Tb_4$, $Ni_4Gd_4$ and $Ni_4Ho_4$ for brevity.

### 4.3.1 Experimental Methods

Single crystals of each compound were measured using a Bruker SMART CCD diffractometer as described in Ref. [80]. D.c. magnetometry was performed in a MPMS while a.c. magnetometry was performed in both a MPMS and PPMS as detailed in Chapter 3. Analogous to the study of the $Co_2Ln$ family, powdered sample were dispersed in Vaseline in gelatin capsules to prevent grain movement during magnetometry measurements. Similarly, to avoid sample heating during a.c. susceptibility measurement at the higher frequencies accessible in the PPMS a $45$ s wait time was included between each frequency in order to ensure temperature stability. Additionally, it was found that for some measurements the a.c. amplitude had to be reduced to prevent this heating problem and this is noted in the appropriate figures.

### 4.3.2 Synthesis and Structure

Synthesis and structural characterisation were performed by S. Biswas, J. Goura, S. Das and V. Chandrasekhar.

All four complexes were synthesised by a sequential reaction. First the ligand $H_5L$ was dissolved in MeOH/$ChCl_3$ which was reacted with the lanthanide containing $LnCl_3{\cdot}6H_2O$ to which was added triethylamine. After $1$ hr of stirring a methanolic solution of $NiCl_2{\cdot}6H_2O$ was added. Further triethylamine followed this. After additional treatment of the reaction mixture (stripping in vacuo and washing followed by slow evaporation) green crystals suitable for X-ray diffrac-

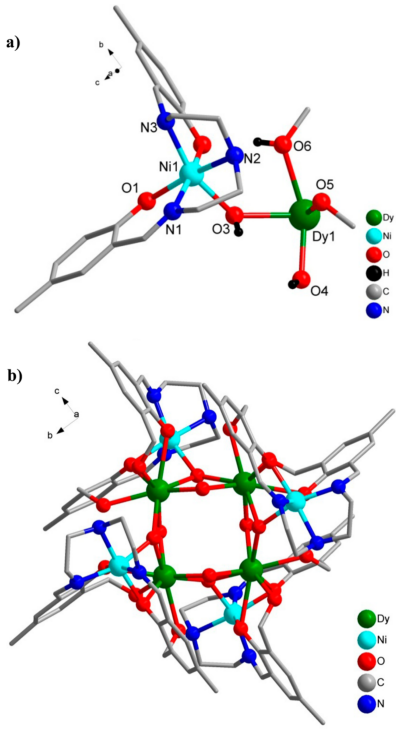



Figure 4.12: (a) The asymmetric unit of $Ni_4Dy_4$. (b) The structure of $Ni_4Dy_4$ omitting hydrogen atoms, chlorides and slovent molecules for clarity.

tion were obtained. Full details of synthesis can be found in Ref. [80].

Single crystal X-ray diffraction showed each compound to be isostructural as cubic systems with space group $I\bar{4}3\mathrm{d}$. Fig. 4.12 shows the structure of $Ni_4Dy_4$ as a representative example of this family. Fig. 4.12(a) shows specifically the asymmetric unit of this compound. Interestingly, the $Ln^{3+}$ ions for this compounds actually lie in a plane and adopt a $[2 \times 2]$ square plane motif with each $Ln^{3+}$ ion connected to a $Ni^{2+}$ ion via three bridging O atoms. The $Ni^{2+}$ ions alternate

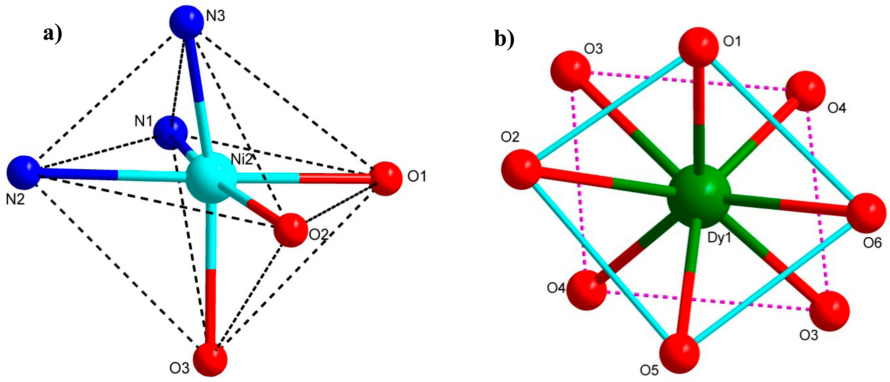



Figure 4.13: (a) The distorted octahedral coordination environment of the $Ni^{2+}$ ions in $Ni_4Dy_4$ and, by extension, the $Ni_4Ln_4$ family. (b) The distorted square anti-prism coordination environment of the $Dy^{3+}$ ions in $Ni_4Dy_4$.

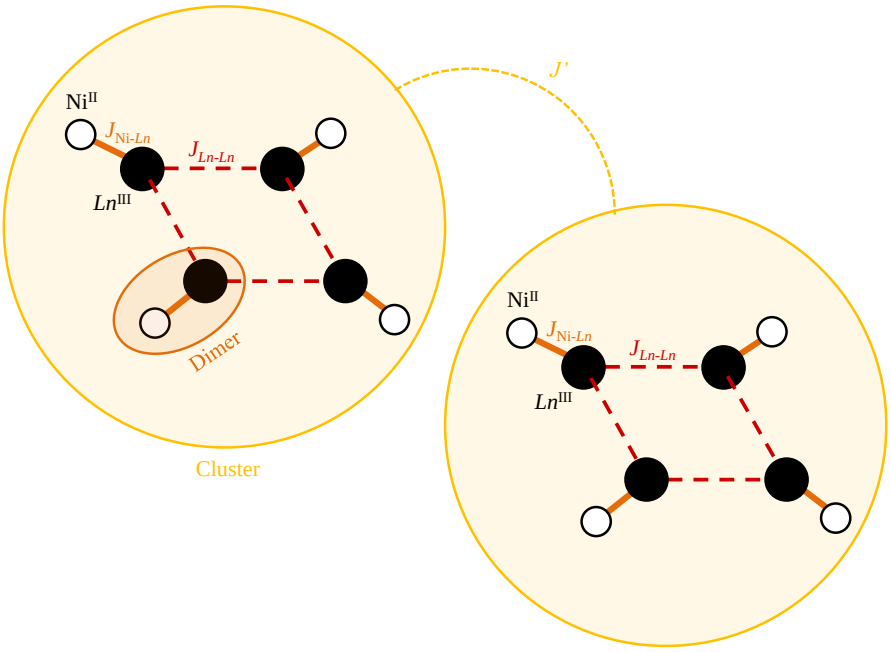



Figure 4.14: Schematic depiction of possible interactions between metal ions in the $Ni_4Ln_4$ family showing only the core metal cluster for clarity.

between lying above or below the $Ln_4$ square plane with a distorted octahedral coordination environment (Fig. 4.13(a)). $Ln^{3+}$ lies at the centre of a distorted square anti-prism (Fig. 4.13(b)). Importantly, octahedral crystal field splitting applied to the $d^8$ $Ni^{2+}$ yields $S = 1$ (unlike $S = 0$ $Co^{3+}$ in the $Co_2Ln$ series). Thus, the magnetic properties of these ions are expected to be a result of both lanthanides and transition metals.

### 4.3.3 Possible Magnetic Exchanges

Before considering the results of magnetometry measurements, it is useful to consider the interactions and anisotropies that may be present in this family of compounds. In terms of magnetic exchange pathways (represented in Fig. 4.14) possibly exchanges that may exist are Ln–Ln, Ni–Ni and Ni–Ln. As these compounds are insulators the relevant exchange mechanism is superexchange requiring clear non-magnetic intermediaries, as discussed in Section 1.3. Therefore, Ni–Ni exchange can be disregarded since there is no structural link between $Ni^{2+}$ ions that does no proceed first through a $Ln^{3+}$ ion. Thus, the system can be

represented by a Hamiltonian of the form,

$$\mathcal{H} = \sum_{\text{Ln ions}} -D_{\text{Ln}}(J_z^{\text{Ln}})^2 + \sum_{\text{Ni ions}} -D_{\text{Ni}}(S_z^{\text{Ni}})^2 + \sum_{\text{All Clusters}} \left[ \sum_{\text{Ni-Ln Pairs}} \mathcal{J}_{\text{Ni-Ln}} \boldsymbol{S}^{\text{Ni}} \cdot \boldsymbol{J}^{\text{Ln}} + \sum_{\text{Ln ions}} \mathcal{J}_{\text{Ln-Ln}} \boldsymbol{J}_i^{\text{Ln}} \cdot \boldsymbol{J}_j^{\text{Ln}} \right] + \sum_{\text{clusters}} \mathcal{J}' \boldsymbol{J}^{\text{cl}} \cdot \boldsymbol{J}^{\text{cl}}, \quad (4.3)$$

where the first line of the equation refers to the single-ion anisotropies that may be associated with each individual ion and the second line considers the possible coupling between $Ni^{2+}$ and $Ln^{3+}$ to produce dimers (quantified by exchange $\mathcal{J}_{\text{Ni-Ln}}$) and the possibility of Ln–Ln exchange. Should dimers form this term would be replaced by an interdimer exchange term, $\mathcal{J}_{\text{Dimer-Dimer}} \boldsymbol{J}_i^{\text{Dimer}} \cdot \boldsymbol{J}_j^{\text{Dimer}}$. The third line incorporates the possibility of intercluster exchange.

Some assumptions can be made about the relative magnitudes of these terms. Firstly, $4f$ orbitals in addition to higher anisotropy than $3d$ orbitals are also more contracted spatially. Therefore, it would be expected for exchange between $Ln^{3+}$ centres to be less than that between Ni–Ln ($\mathcal{J}_{\text{Ln-Ln}} \ll \mathcal{J}_{\text{Ni-Ln}}$). It can be argued based on the large distance between molecules and the lack of structural link (and therefore superexchange pathway) that the intercluster exchange, $\mathcal{J}'$, should be the smallest exchange term. Indeed, this lack of strong intermolecular exchange is expected for SMMs. As such, a system of weakly interacting Ni–Ln dimers may be encountered. Furthermore, other studies of systems containing $Ni^{2+}$–$Ln^{3+}$ exchange [121–124] have suggested an empirical rule of ferromagnetic exchange when $Ln^{3+}$ contains half-filled or greater $4f$ orbitals but antiferromagnetic otherwise [125]. This suggests that each member of this family should show ferromagnetic dimer exchange though deviations from this may occur as it does not take into account bond angles or number of bridging intermediates. Fi-

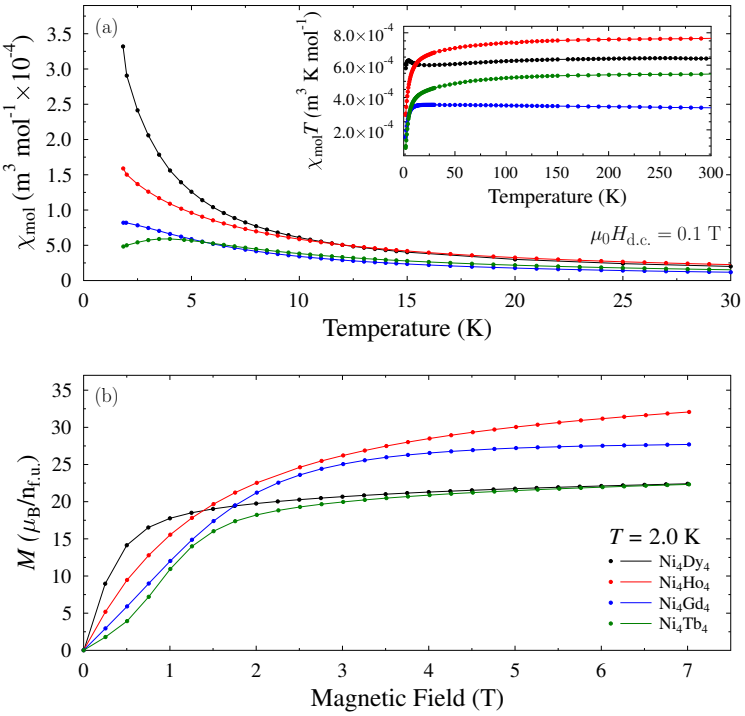



Figure 4.15: (a) D.c. molar susceptibility ($\chi_{\mathrm{mol}}$) of the $Ni_4Ln_4$ family measured in a magnetic field of $\mu_0 H_{\mathrm{d.c.}} = 0.1$ T. Presented are ZFC sweeps. Inset: Product of molar susceptibility with temperature ($\chi_{\mathrm{mol}}T$) vs. temperature. (b) Isothermal magnetisation of each member of this family vs. applied d.c. field up to 7 T at 2.0 K. Only up sweeps are shown for clarity as no hysteresis was detected.

nally, due to the high anisotropies associated with the $4f$ electrons of lanthanide ions [116], the depiction of interactions in Eq. 4.3 as Heisenberg may not be accurate.

### D.C. Magnetometry

The results of d.c. magnetometry measurements on each $Ni_4Ln_4$ compound are shown in Fig. 4.15. Due to the greater complexity in each compound compared to the $Co_2Ln$ family (owing to the presence of multiple magnetic ions) each will be discussed in turn. Prior to this a brief note can be made of the high temperature region of $\chi T$ vs. $T$ (inset of Fig. 4.15(a)). Each compound shows a flat, constant value of $\chi T$ at high temperatures indicative of each compound being in a paramagnetic phase with thermal fluctuations overcoming any internal interactions. Furthermore, these high temperature values of $\chi T$ lie within $\sim 15$ % of that expected from four $Ni^{2+}$ ions and four $Ln^{3+}$ ions that obey Eq. 4.1. This

suggests any low temperature deviations will result from metal ion anisotropies and interactions. The $15\%$ deviation likely arises from unaccounted diamagnetic contributions from sample holder, Vaseline and organic ligands and/or small milligram mass losses which occurred during mixing of each sample with Vaseline. Only for $Ni_4Gd_4$ can a small negative gradient in $\chi T$ be detected at high temperatures likely arising from the aforementioned diamagnetic contributions. It likely is not visible in the other compounds due to $Ni_4Gd_4$ showing the lowest room-temperature magnetic moment.

**$Ni_4Gd_4$**

Much like studies of the $Co_2Ln$ family, the inclusion of a member for Ln = Gd allows the study of magnetic properties in absence of $Ln^{3+}$ anisotropy [116]. In fact, when considering only the single ion terms of Eq. 4.3 it would be expected for the lanthanide term to dominate meaning $Ni_4Gd_4$ affords the opportunity to study the influence of the lesser $Ni^{2+}$ anisotropy in these systems should magnetic exchange be weak.

D.c. susceptibility of $Ni_4Gd_4$ (Fig. 4.15(a)) increases as temperature is decreased until the lowest measured temperatures where it appears to stabilise. At low temperatures, a rapid drop of $\chi T$ below $T > 10\ \mathrm{K}$ is observed. This may be entirely or in part due to a thermal depopulation of the $Ni^{2+}$ levels ($D_{\mathrm{Ni}} \neq 0$) [54, 76, 117]. Additional contributions may be Gd–Gd interactions. In fact, the onset of a low-temperature plateau in $\chi$ can indicate the presence of $D_{\mathrm{Ni}} \neq 0$ [126] which, if correct, also suggests a reduction of the contribution of paramagnetic $Gd^{3+}$ due to the lack of Curie-like divergence of $\chi$ at low temperatures.

In considering Ni–Gd exchange, a density functional theory study of a dinuclear [$Ni^{2+}$–$Gd^{3+}$] complex [127] found an empirical formula for calculating Ni–Gd exchange as $\mathcal{J}_{\mathrm{Ni-Gd}} = A\exp(-x/t) + y_0$ where $y_0 = 5.50118\ \mathrm{cm}^{-1}$, $A = -28.62337\ \mathrm{cm}^{-1}$, $t = 50.98665$ and $x$ is the Ni–O–Gd bond angle in degrees. While specifically for a dinuclear complex (which these compounds are not) this

was used to estimate exchange through each of the three unique Ni–O–Gd exchange pathways in a single dimer and allowing them to sum yielded an overall exchange strength of $\mathcal{J}_{\mathrm{Ni-Gd}}/k_{\mathrm{B}} \approx 2.3$ K. For Gd–Gd interactions, the dipolar interaction was considered since the Ln–Ln exchange is expected to be small. By treating each $Gd^{3+}$ ion as a classical moment with $\mu = \mu_{\mathrm{eff}}\mu_{\mathrm{B}}$ the dipole-dipole energy (Eq. 1.21) was found to be lowered on cooling by $E/k_{\mathrm{B}} \sim 2.8$ K if each $Gd^{3+}$ ion aligns antiparallel to its neighbour and perpendicular to the $Gd_4^{3+}$ square plane. As this reduction is of a slightly higher value than the estimated $\mathcal{J}_{\mathrm{Ni-Gd}}$ it can tentatively be reasoned as to why $\chi$ levels off at low temperatures. The dipole-dipole interaction causes the $Gd^{3+}$ ions to align antiferromagnetically effectively cancelling out their contribution to the susceptibility thus leaving only the (single-ion) $Ni^{2+}$ behaviour to be observed.

Assuming $Ni^{2+}$ alone was the cause of the low temperature $\chi$ behaviour, a $Ni^{2+}$ ion with easy plane anisotropy was considered in further detail. Isolated and without interaction the appropriate Hamiltonian is of the form,

$$\mathcal{H} = D_{\mathrm{Ni}} S_z^2 + g_J \mu_{\mathrm{B}} \mu_0 \boldsymbol{S} \cdot \boldsymbol{H}, \tag{4.4}$$

where the first term accounts for $Ni^{2+}$ single-ion anisotropy and the second is a Zeeman term. Note a different convention for $D$ is used here such that $D_{\mathrm{Ni}} > 0$ is easy plane. The formalism of Eq. 3.42 is otherwise used throughout this thesis. For $Ni_4Gd_4$ to follow this Hamiltonian other effects (such as Ni–Gd interactions) must be small enough to be ignored (i.e. the system must be at a temperature above the strength of these effects). This Hamiltonian may be exactly diagonalised to yield all possible energy levels, $E_n$, where $n$ defines the level. This may then be used to calculate the magnetic susceptibility using the Van Vleck formula [4]

$$\chi = \frac{N\sum_n (E_n^{(1)2}/k_{\mathrm{B}}T - 2E_n^{(2)})\exp\left(-E_n^{(0)}/k_{\mathrm{B}}T\right)}{\sum_n \exp\left(-E_n^{(0)}/k_{\mathrm{B}}T\right)}. \tag{4.5}$$

This formula involves the approximations of expanding the energy levels in powers of the applied field, $E_n = E_n^{(0)} + E_n^{(1)}H + E_n^{(2)}H^2 + \cdots$, and $H/k_{\mathrm{B}}T \ll 1$ [4]. Powder averaging may subsequently be performed (which effectively randomises the direction of the applied magnetic field) and yields a susceptibility of

$$\chi = \frac{N_{\mathrm{A}}\mu_0\mu_{\mathrm{B}}^2 g_J^2 S(S+1)}{3}\left(\frac{\exp(-\beta D)}{k_{\mathrm{B}}T(1+2\exp(-\beta D))} + \frac{2(1-\exp(-\beta D))}{D(1+2\exp(-\beta D))}\right), \tag{4.6}$$

where $\beta = 1/k_{\mathrm{B}}T$. Simulations of this equation are shown in Fig. 4.16 as well as the unique behaviour of a minimum in $\mathrm{d}\chi/\mathrm{d}T$ at a value proportional to $D_{\mathrm{Ni}}$ ($T = 0.45D_{\mathrm{Ni}}/k_{\mathrm{B}}$). The value of this minimum was found to be $3.0(3)$ K for $Ni_4Gd_4$, slightly above the estimate of the temperature of Gd-Gd dipolar interactions (but within error). As such, it is acknowledged that the antiferromagnetic alignment of $Gd^{3+}$ ions may affect $\mathrm{d}\chi/\mathrm{d}T$ and the estimate of $D_{\mathrm{Ni}}/k_{\mathrm{B}} = 6.7(7)$ K.

The isothermal magnetisation of $Ni_4Gd_4$ is shown in Fig. 4.15(b) and follows a steady, near linear increase to a value of $M = 25\ \mu_{\mathrm{B}}/n_{\mathrm{f.u.}}$ at $\mu_0 H_{\mathrm{d.c.}} = 7$ T. This lies well below the saturation magnetisation ($M_{\mathrm{sat}} = g_J J$) of four paramagnetic $Ni^{2+}$ ions and four paramagnetic $Gd^{3+}$ ions ($M = 36\ \mu_{\mathrm{B}}/n_{\mathrm{f.u.}}$) suggestive of the presence of an anisotropy in the system. The presented d.c. susceptibility measurements suggest this to be the single-ion anisotropy of $Ni^{2+}$.

### $Ni_4Ho_4$

The d.c susceptibility of $Ni_4Ho_4$ (Fig. 4.15(a)) can be observed to increase on cooling showing no evidence of the levelling off that occurred at the lowest temperatures for $Ni_4Gd_4$. As temperature decreases $\chi T$ remains steady before beginning to decrease at $\sim 50$ K, a much higher temperature than the similar

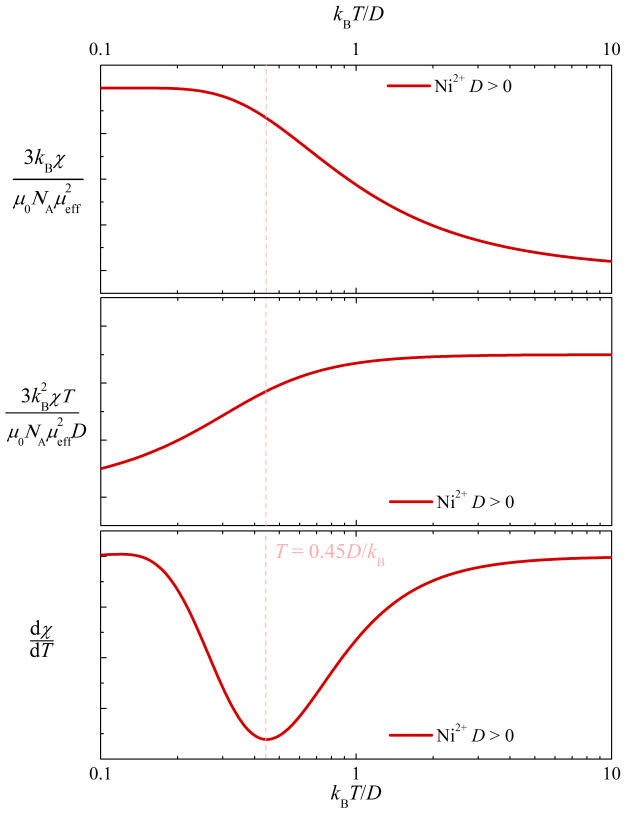



Figure 4.16: Simulated curves of d.c. magnetic behaviour of an easy plane $Ni^{2+}$ ion based on Eq. 4.6. Data has been normalised and plotted as $\chi$, $\chi T$ and $\mathrm{d}\chi/\mathrm{d}T$. Also indicated is the unique value of temperature resulting in a minimum in $\mathrm{d}\chi/\mathrm{d}T$ ($T = 0.45D_{\mathrm{Ni}}/k_{\mathrm{B}}$). Diagonalisation of Hamiltonian and simulation performed by J. Brambleby.

behaviour for $Ni_4Gd_4$. Due to the high anisotropy associated with the electron distribution of $Ho^{3+}$ [116] it would be expected that $|D_{\mathrm{Ho}}| \gg |D_{\mathrm{Ni}}|$. Therefore, while this behaviour was associated with the thermal depopulation of $Ni^{2+}$ levels for $Ni_4Gd_4$, for $Ni_4Ho_4$ it can be associated with a combination of the depopulation of the $Ni^{2+}$ levels and the split $Ho^{3+}$ levels due to a non-zero $D_{\mathrm{Ho}}$. The lack of levelling off in $\chi$ at the lowest measurement temperatures suggest no cancelling out of the $Ho^{3+}$ magnetic moments (i.e. no antiferromagnetic Ho–Ho interaction) as has been suggested for $Ni_4Gd_4$.

The isothermal magnetisation at $2.0\ \mathrm{K}$ showed no evidence for hysteresis (Fig. 4.15(b) shows only up sweeps due to this fact) nor did any anomalies appear in $\chi$. As such this suggests no strong interactions in this system and the single ion properties of $Ni^{2+}$ and $Ho^{3+}$ dominate. The magnetisation of $Ni_4Ho_4$ shows a slow increase that appears to be plateauing but has not succeeded by the maximum applied field of $7\ \mathrm{T}$. At this field, $M \sim 32\ \mu_{\mathrm{B}}/n_{\mathrm{f.u.}}$ which is much less than the predicted saturation magnetisation from the ensemble of eight independent metal ions of $50.7\ \mu_{\mathrm{B}}/n_{\mathrm{f.u.}}$. Even if slight errors in mass determination are allowed this shows that another effect is present in the sample preventing saturation from being reached. Thus this offers further evidence for a large $D_{\mathrm{Ho}}$.

Considering only properties due to the single ions, it can be noted that $Ho^{3+}$ is a non-Kramers ion ($J = 6$), a degenerate ground state is not ensured requiring an axial crystal field at the lanthanide centres [116]. At the lanthanide centres of these compounds the point group is determined to be $1$ not fulfilling this requirement. As such, it is likely that $D_{\mathrm{Ho}} < 0$ with an easy plane anisotropy.

#### $Ni_4Dy_4$

The susceptibility of $Ni_4Dy_4$ ($\chi$ shown in Fig. 4.15(a)) increases monotonically on cooling in a manner most similar to $Ni_4Ho_4$ but with greater magnitude. $\chi T$ (inset of Fig. 4.15(a)) shows the greatest difference from the other compounds in this family, decreasing on cooling below $\sim 100\ \mathrm{K}$ in a manner similar to $Ni_4Ho_4$

suggestive of a depopulation of the lanthanide ion spin states (i.e. $D_{\mathrm{Dy}} \neq 0$). At lower temperatures a peak appears in $\chi T$ centred at $T \sim 4.8$ K. This feature has been observed in other $Ni^{2+}$–$Ln^{3+}$ compounds and has been associated with a ferromagnetic exchange between $Ni^{2+}$ and $Ln^{3+}$ [121, 122, 125]. As such, $Ni_4Dy_4$ is the compound most likely showing ferromagnetic exchange.

The magnetisation of $Ni_4Dy_4$ at $2.0$ K shows the most rapid initial increase of any member of this series transitioning to a slower increase above $1$ T. While still showing a small positive gradient at $7$ T the value of $M$ at this field ($22.5\ \mu_{\mathrm{B}}/n_{\mathrm{f.u.}}$) is much less than the expected saturation magnetisation of $48.0\ \mu_{\mathrm{B}}/n_{\mathrm{f.u.}}$. As with the the previous compounds, this suggests the presence of single-ion anisotropies of both $Ni^{2+}$ and $Dy^{3+}$. Furthermore, since this shows the rapid initial increase of $M$ did not lead to saturation, it is likely that this increase can be be associated with the energy scale of some interaction in the system (i.e. an exchange).

**$Ni_4Tb_4$**

$Ni_4Tb_4$ shows a small low temperature susceptibility (Fig. 4.15(a)) and a rounded maximum at $3.9(3)$ K in contrast to the levelling off observed for $Ni_4Gd_4$ which was attributed to the single-ion anisotropy of $Ni^{2+}$ ions and cancelling out of $Gd^{3+}$ ion moments suggested to be due to antiferromagnetic interactions.

$\chi T$ (inset of Fig. 4.15(a)) bears strong similarity to $Ni_4Ho_4$. As temperature is decreased, the high temperature steady value of $\chi T$ begins to decrease around $\sim 100$ K which can be attributed to thermal depopulation of crystal-field split $Tb^{3+}$ (analogous to $Ni_4Dy_4$ and $Ni_4Ho_4$ signifying $D_{\mathrm{Tb}} \neq 0$). Like $Ho^{3+}$, $Tb^{3+}$ is $J = 6$ so via similar arguments it is expected $D_{\mathrm{Tb}} < 0$. Again analogous to $Ni_4Ho_4$, $\chi T$ shows a more pronounced decrease for $T < 10$ K. This feature is also shared with the $Gd^{3+}$ congener where it was attributed to a thermal depopulation of crystal-field split $Ni^{2+}$ levels ($D_{\mathrm{Ni}} \neq 0$). Therefore, it is also attributed to $D_{\mathrm{Ni}} \neq 0$ for $Ni_4Tb_4$.

A peak similar to that found in $Ni_4Dy_4$ is not detected in $\chi T$ indicating a

lack of ferromagnetic Ni–Tb interactions [121, 122, 125]. Combined with the observation of a peak in $\chi$ (and forthcoming a.c. susceptibility measurements) these lead to a proposed model with antiferromagnetic exchange between $Ni^{2+}$ and $Tb^{3+}$ ions. This would be consistent with the maximum of $\chi$ corresponding to a cancellation of Ni–Tb dimer moments due to anitferromagnetic interactions (likely dipolar interactions based on $Ni_4Gd_4$ results). This would imply $Ni_4Tb_4$ to be a counterexample to the empirical rule that predicts ferromagnetic exchange between $Ni^{2+}$ and $Ln^{3+}$ ions since each compound in this study shows half-filled or greater $4f$ orbitals [121, 122, 125]. This deviation likely originates from the precise form of the Ni–Ln exchange pathway and indeed appears to be violated by most compounds in this family.

The isothermal magnetisation of $Ni_4Tb_4$ at $2.0\ \mathrm{K}$ (Fig. 4.15(b)) initially shows a concave increase towards a broad shoulder around $\mu_0 H_{\mathrm{d.c.}} \approx 1.5\ \mathrm{T}$. This leads to a steady increase that eventually matches the small gradient of $Ni_4Dy_4$. Remarkably, the magnetisation reached at $7\ \mathrm{T}$ ($22.5\ \mu_{\mathrm{B}}/n_{\mathrm{f.u.}}$) matches that of $Ni_4Dy_4$. This is below the saturation magnetisation of $44\ \mu_{\mathrm{B}}/n_{\mathrm{f.u.}}$ suggestive of further interactions or anisotropies in the system at higher energy scales.

### 4.3.4 A.C. Magnetometry

#### $Ni_4Gd_4$

In zero applied d.c. magnetic field the real part of a.c. susceptibility of $Ni_4Gd_4$ (Fig. 4.17(a)) increases on cooling with no indication of frequency separation for frequencies of $\nu \leq 1500\ \mathrm{Hz}$ and temperatures above $2.0\ \mathrm{K}$. Furthermore, $\chi''$ (Fig. 4.17(b)) remains zero throughout suggesting no slow magnetic relaxation is taking place. When applying a d.c. magnetic field of $\mu_0 H_{\mathrm{d.c.}} = 0.1\ \mathrm{T}$ $\chi'$ (Fig. 4.17(c)) remains relatively unchanged with perhaps a very slight separation of frequencies occurring at $2.0\ \mathrm{K}$ though this does not appear to be accompanied by a development of a non-zero $\chi''$ (Fig. 4.17(d)). As such, this can likely be

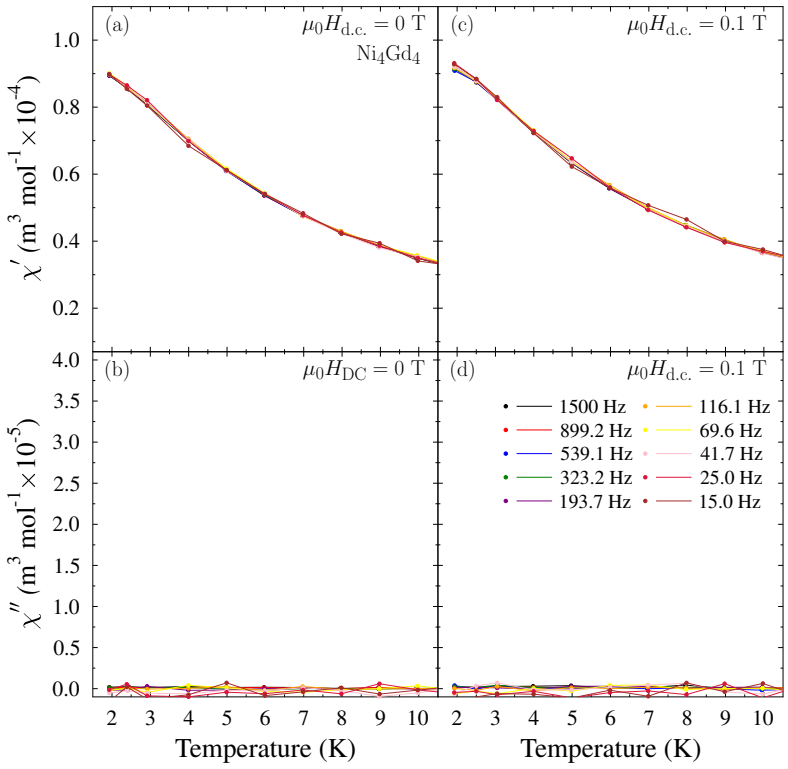



Figure 4.17: In-phase and out-of-phase components ($\chi'$ and $\chi''$) of a.c. susceptibility of $Ni_4Gd_4$ with an a.c. amplitude of $\mu_0 H_{\mathrm{a.c.}} = 0.4$ mT. (a) and (b) show data in a d.c. magnetic field of $\mu_0 H_{\mathrm{d.c.}} = 0$ T and (c) and (d) show data in a magnetic field of $\mu_0 H_{\mathrm{d.c.}} = 0.1$ T.

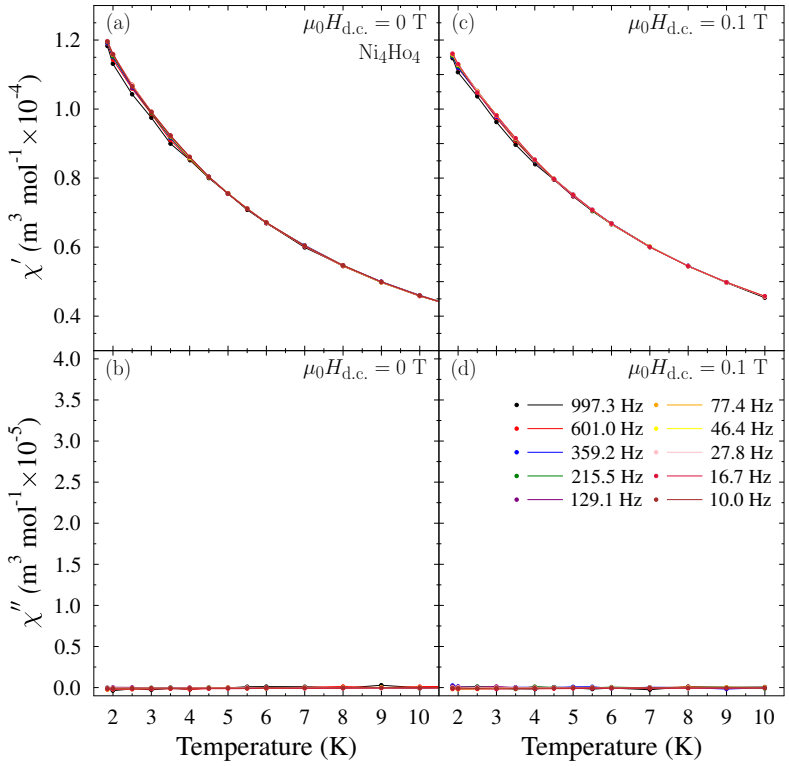



Figure 4.18: In-phase and out-of-phase components ($\chi'$ and $\chi''$) of a.c. susceptibility of $Ni_4Ho_4$ with an a.c. amplitude of $\mu_0 H_{\mathrm{a.c.}} = 0.4$ mT. (a) and (b) show data in a d.c. magnetic field of $\mu_0 H_{\mathrm{d.c.}} = 0$ T and (c) and (d) show data in a magnetic field of $\mu_0 H_{\mathrm{d.c.}} = 0.1$ T.

attributed to the slight slow magnetic relaxation that may be induced in paramagnets by an applied magnetic field [31, 54].

Therefore, a.c. and d.c. measurements suggests $Ni_4Gd_4$ does indeed contain a non-zero anisotropy originating from the $Ni^{2+}$. However, the lack of a strong frequency dependent signal suggests it is easy plane rather than the easy axis required for SMM slow magnetic relaxation as predicted from $Ni^{2+}$ simulations.

### $Ni_4Ho_4$

Investigating the dynamic behaviour of $Ni_4Ho_4$ at low a.c. frequencies and in zero applied d.c. fields finds the real part (Fig. 4.18(a)) to increase as temperature is decreased with no frequency dependence. $\chi''$ (Fig. 4.18(b)) also remains zero throughout the measurement range suggesting a lack of slow magnetic relaxation. The situation remains largely unchanged when applying a small d.c

magnetic field (Fig. 4.18(c) and (d)) with only a slight depression in magnitude of $\chi'$ at low temperatures. This suggests a lack of field-induced slow relaxation. A small caveat exists in that at both $\mu_0 H_{\mathrm{d.c.}} = 0$ and $0.1$ T the maximum a.c. frequency sweep of $\chi'$(T) drops slightly below other frequencies for $2.0 \leq T \leq 4.0$ K but recovers at $T = 1.8$ K such that all frequencies show the same $\chi'$. Other frequencies do not consistently show the expected ordering for a slow relaxing effect. Additionally, no $\chi''$ signal accompanies this feature. Therefore, it may be attributed to a measurement artefact.

This observation of no slow magnetic relaxation supports the conclusion from d.c. results of a large, non-zero $D_{\mathrm{Ho}}$ that is easy plane ($D_{\mathrm{Ho}} < 0$). Thus (if the results from isostructural $Ni_4Gd_4$ can be generalised to $Ni_4Ho_4$) due to the lack of evidence for Ni–Ho interactions, both d.c. and a.c. measurements suggests this compound contains single-ion anisotropies from both $Ni^{2+}$ and $Ho^{3+}$, both of which are easy plane with $|D_{\mathrm{Ho}}| \gg |D_{\mathrm{Ni}}|$.

**$Ni_4Dy_4$**

Fig. 4.19(a) and (b) show the a.c. susceptibility of $Ni_4Dy_4$ in $\mu_0 H_{\mathrm{d.c.}} = 0$ T. A frequency separation is evident in $\chi'$ below $\sim 5$ K of the ordering expected for slow magnetic relaxation (higher frequencies being reduced at higher temperatures). $\chi''$ also shows a clear frequency-dependence, becoming non-zero at $\sim 8$ K. This is very similar to SMM compounds in which slow thermal relaxation is suppressed at zero applied fields due to the presence of quantum tunnelling [54, 76, 77] as was found for $Co_2Er$ and $Co_2Tb$ in Section 4.2.4.

In order to investigate the presence of SMM slow magnetic relaxation, a d.c. magnetic field study was performed with the out-of-phase results shown in Fig. 4.20(a). Following each line of constant magnetic field, $\chi''$ increases with increasing frequency reaching a peak that appears outside the measurement range for low fields and is suppressed into the measurement range for intermediate fields. At higher fields the peak is pushed to higher frequencies. As an isother-

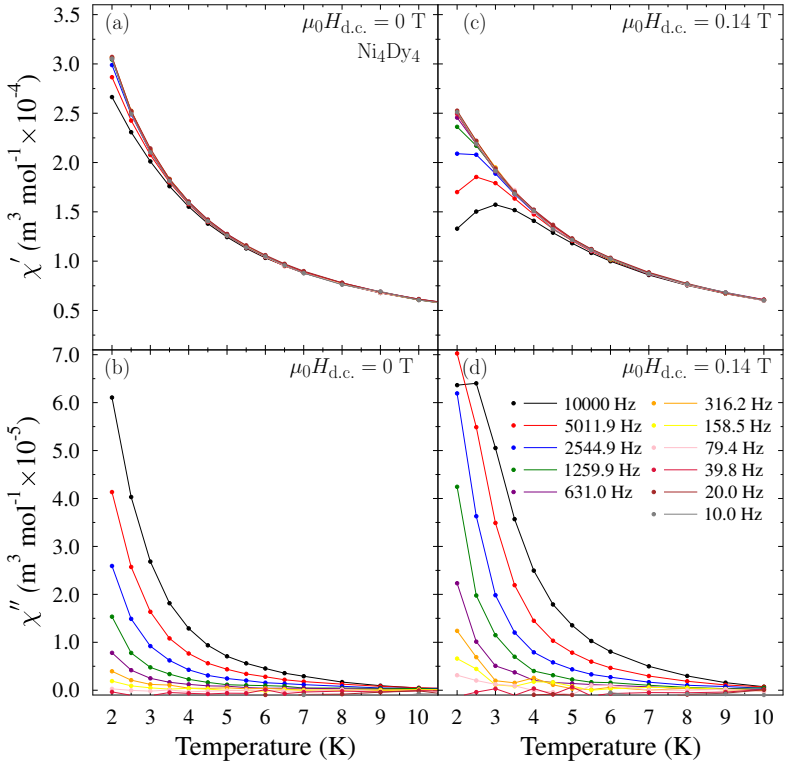



Figure 4.19: In-phase and out-of-phase components ($\chi'$ and $\chi''$) of a.c. susceptibility of $Ni_4Dy_4$ with an a.c. amplitude of $\mu_0 H_{\mathrm{a.c.}} = 0.4$ mT for $\nu \leq 1259.9$ Hz and $\mu_0 H_{\mathrm{a.c.}} = 0.1$ mT for $\nu > 1259.9$ Hz. The change of a.c. field amplitude was found to be required due to heating effects. (a) and (b) show data in a d.c. magnetic field of $\mu_0 H_{\mathrm{d.c.}} = 0$ T and (c) and (d) show data in derived optimum magnetic field of $\mu_0 H_{\mathrm{d.c.}} = 0.14$ T.

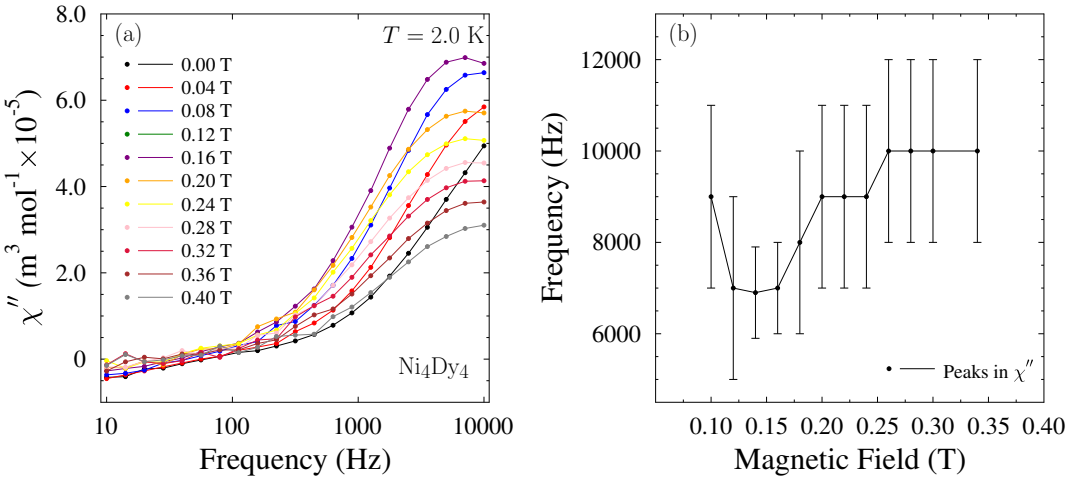



Figure 4.20: (a) Out-of-phase susceptibility of $Ni_4Dy_4$ at $T = 2.0$ K as d.c. field was varied from $\mu_0 H_{\mathrm{d.c.}} = 0$ to $0.4$ T. Data were measured in $0.02$ T steps though only half of all data are shown for clarity. (b) Peaks from (a) derived as the points where $\mathrm{d}\chi''/\mathrm{d}\nu = 0$. Large error is due to the logarithmic scale of (a) combined with the peaks occurring on the high frequency side.

mal measurement, these peaks more accurately fulfil the condition $\omega\tau = 1$ (as stated in Section 3.3.6 selecting $\chi''(T)$ peaks assumes $\chi_S$ and $\chi_T$ to vary little over the temperature for which the peak occurs) allowing the change of $\tau$ with d.c. magnetic field to be followed. This is shown in Fig. 4.20(b) as $\nu$ ($\propto \tau^{-1}$) vs. $\mu_0 H_{\mathrm{d.c.}}$. $\tau^{-1}$ initially decreases as d.c. magnetic field increases: magnetic relaxation slows. Such an effect is expected for a SMM for which slow thermal relaxation is suppressed at zero d.c. magnetic field by quantum tunnelling. The increase of $\tau^{-1}$ beyond the minimum of $\sim 0.14$ T is likely due to further relaxation processes becoming important as described in Eq. 3.44. The minimum of $\sim 0.14$ T represents the optimum field to study Orbach type relaxation as the contribution of quantum tunnelling has been minimised and other effects have not yet overcome the field independent Orbach process.

Therefore, a.c. susceptibility as a function of temperature was measured at this optimum field as shown in Figs. 4.19(c) and (d). $\chi'$ has dramatically changed from the zero d.c. field case showing a frequency separation below $\sim 5$ K and a number of peaks have been resolved at high frequencies. $\chi''$ has become non-zero below $\sim 9$ K and found a general enhancement of magnitude compared to zero field results. Importantly, for the maximum measurement frequency (10 kHz) $\chi''$ appears to level off at the lowest measured temperatures. This appears to be the edge of a peak and strongly suggests that slow magnetic relaxation is present in $Ni_4Dy_4$ at $\mu_0 H_{\mathrm{d.c.}} = 0.14$ T but lies just outside the available measurement range requiring lower temperatures and/or higher frequencies to fully investigate.

Further examination of this field-induced slow relaxation was performed by preparing a Cole-Cole plot of the a.c. susceptibility at $\mu_0 H_{\mathrm{d.c.}} = 0.14$ T as shown in Fig. 4.21. As temperature is reduced, the data begin to trace isothermal arcs with the lowest temperature showing the most complete arc. This is suggestive of single relaxing entities. A fit to the generalised Debye model (Eq. 3.28) at 2.0 K is

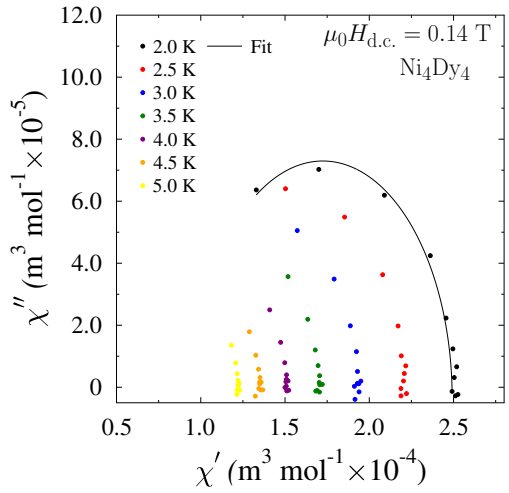



Figure 4.21: Cole-Cole plot ($\chi''$ vs. $\chi'$) of a.c. susceptibility in $\mu_0 H_{\mathrm{d.c.}} = 0.14$ T of $Ni_4Dy_4$. The lowest temperature was fit to Eq. 3.38.

also shown in Fig. 4.21 which yielded parameters $\chi_T = 2.491(7) \times 10^{-4}$ m$^3$ mol$^{-1}$, $\chi_S = 9.6(9) \times 10^{-5}$ m$^3$ mol$^{-1}$ and $\alpha = 0.03(4)$. This low value of $\alpha$ suggests a small spread of relaxation times and that $Ni_4Dy_4$ should reasonably obey the Debye model. Combined with the previous a.c. susceptibility observations this offers strong evidence that $Ni_4Dy_4$ behaves as a field-induced SMM with quantum tunnelling in zero applied d.c. magnetic field.

The origin of this weak SMM behaviour in $Ni_4Dy_4$ likely arises from single-ion anisotropy of $Dy^{3+}$. Analogous with $Co_2Er$ (see Section 4.2.4), $Dy^{3+}$ with $J = 15/2$ is a Kramers ion necessitating a degenerate ground state. It should be noted that the formation of Ni–Dy dimers could affect this degenerate ground state though the dimer anisotropy would likely be dominated by the larger $Dy^{3+}$ anisotropy. Due to the already discussed $Ln^{3+}$ centre point group of 1 for $Ni_4Ho_4$ there does not appear to be a ligand environment reason for a degenerate ground state.

### $Ni_4Tb_4$

In $\mu_0 H_{\mathrm{d.c.}} = 0$ T the real part of a.c. susceptibility of $Ni_4Tb_4$ (Fig. 4.22(a)) shows no frequency dependence except a small amount at 2.0 K. The most prominent feature is the rounded maximum detected at $\sim 3.9$ K which matches the same

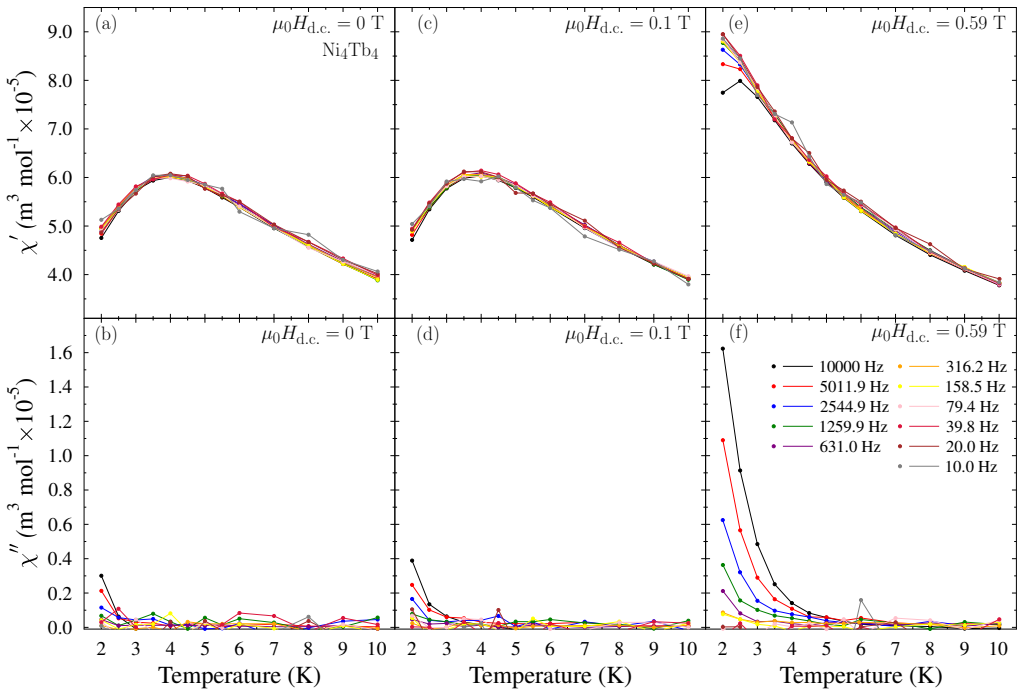



Figure 4.22: In-phase and out-of-phase components ($\chi'$ and $\chi''$) of a.c. susceptibility of $Ni_4Tb_4$ with an a.c. amplitude of $\mu_0 H_{\mathrm{a.c.}} = 0.4$ mT for $\nu \leq 1259.9$ Hz and $\mu_0 H_{\mathrm{a.c.}} = 0.1$ mT for $\nu > 1259.9$ Hz. The change of a.c. field amplitude was found to be required due to heating effects. (a) and (b) show data in a d.c. magnetic field of $\mu_0 H_{\mathrm{d.c.}} = 0$ T, (c) and (d) show data in a d.c. magnetic field of $\mu_0 H_{\mathrm{d.c.}} = 0.1$ T and (e) and (f) show data in a d.c. magnetic field of $\mu_0 H_{\mathrm{d.c.}} = 0.59$ T.

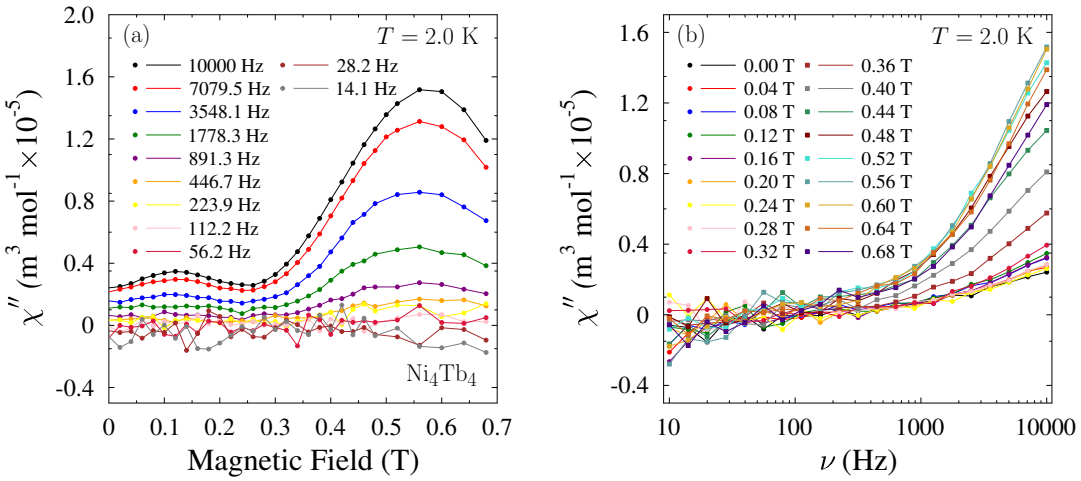



Figure 4.23: (a) Out-of-phase component of a.c. response of $Ni_4Tb_4$ at 2.0 K as d.c. magnetic field is varied. (b) Same data as (a) plotted as a function of frequency. No $\chi''$ peaks are resolved within the available frequency range.

feature in d.c. susceptibility. In $\chi''$ a weak, non-zero signal is only observed for $T < 3$ K. A small, arbitrary d.c. field of $\mu_0 H_{\mathrm{d.c.}} = 0.1$ T was applied to act as a test for field-induced slow magnetic relaxation. The results of these measurements are shown in Figs. 4.22(c) and (d). Both $\chi'$ and $\chi''$ remain relatively unchanged from the zero d.c. field case with only a slight enhancement of $\chi''$. The presence of a small out-of-phase component prompted a d.c. magnetic field dependent study analogous to $Ni_4Dy_4$. This is shown in Figs. 4.23(a) and (b). Considering Fig. 4.23(a) where data was plotted as $\mu_0 H_{\mathrm{d.c.}}$ was varied the out-of-phase component and frequency dependence is initially enhanced with small maximum in the region of $0.1$ T before being reduced. On further increase of $\mu_0 H_{\mathrm{d.c.}}$ a second, larger set of broad maxima appear. For the maximum a.c. measurement frequency ($10$ kHz) this maximum lies at $\sim 0.59$ T with lower frequency peaks lying at slightly lower magnetic fields. This means as the d.c. magnetic field increases in this region the relaxation rate of the magnetic relaxation process ($\tau^{-1} = \omega$ at the $\chi''$ peaks) increases. Thus the frequency ordering of these peaks hints at d.c. magnetic field dependent relaxation mechanism not proceeding as would be expected for quantum tunnelling (which would slow for increased $\mu_0 H_{\mathrm{d.c.}}$). Thus, it appears a different relaxation mechanism may be present than that for standard SMMs though this analysis assumes little change in $\chi_S$ and $\chi_T$ over these peaks as magnetic field is varied. Plotting this data as lines of constant d.c. field while varying $\nu$ (Fig. 4.23(b)) eliminates this assumption. This is qualitatively similar to Fig. 4.20(a) though does not result in any peaks within the measurement frequency range. As such the condition $\omega\tau = 1$ does not fall within the measurement range and so an optimum field to observe Arrhenius behaviour could not be found. Therefore, the a.c. susceptibility as a function of temperature was remeasured in $\mu_0 H_{\mathrm{d.c.}} = 0.59$ T and is presented in Figs. 4.22(e) and (f). The larger d.c. magnetic field has suppressed the frequency independent maximum in $\chi'$ and yielded what appears to be the first of a series

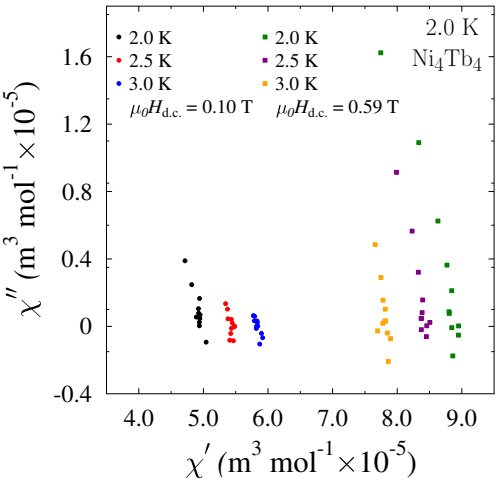



Figure 4.24: Cole-Cole plot ($\chi''$ v. $\chi'$) of a.c. susceptibility in $\mu_0 H_{\mathrm{d.c.}} = 0.1$ T and $\mu_0 H_{\mathrm{d.c.}} = 0.59$ T for $Ni_4Tb_4$.

of frequency dependent $\chi'$ peaks for the 10 kHz measurements. The suppression of the $\chi'$ maximum to lower temperatures with higher d.c. fields suggests the presence of antiferromagnetic interactions lending support to the presence of antiferromagnetic dimers. $\chi''$ shares similar behaviour to data measured in lower d.c. fields showing a general increase of magnitude, becoming non-zero below $\sim 6.0$ K.

As qualitatively similar data to $Ni_4Dy_4$ was obtained, further investigation of the slow magnetic relaxation was performed by constructing a Cole-Cole plot. This was constructed for the lowest measured temperatures of both non-zero d.c. magnetic field measurements and is presented in Fig. 4.24. In $\mu_0 H_{\mathrm{d.c.}} = 0.1$ T it is difficult to determine if data is beginning to trace isothermal arcs due to the small out-of-phase component. In $\mu_0 H_{\mathrm{d.c.}} = 0.59$ T low temperature data appears to show the beginnings of clearer arcs which extend more in the $\chi'$–$\chi''$ plane as temperature is decreased. The small amount of arcs visible prevents fits to the generalised Debye model or, indeed, determination of whether single arcs are present but certainly aids in the confirmation of slow magnetic relaxation in $Ni_4Tb_4$ which is more prominent at $\mu_0 H_{\mathrm{d.c.}} = 0.59$ T.

While this slow magnetic relaxation is field-induced, in combination with d.c. results it does not agree with traditional SMM slow relaxation. D.c. results have

suggested $D_{\mathrm{Tb}} < 0$ with a generalisation of $Ni_4Gd_4$ measurements also suggesting $D_{\mathrm{Ni}} < 0$ (both stated in the formalism of Eq. 3.42). Therefore, there is no source of SMM-type slow magnetic relaxation which requires an Ising axis. Even the formation of antiferromagnetic Ni–Tb dimers does not offer evidence of the introduction of an easy-axis suggesting the slow relaxation must have a different origin. At $\mu_0 H_{\mathrm{d.c.}} = 0.59$ T (where the slowest relaxation was obtained) the d.c. magnetisation of the sample was undergoing a rapid rise (see Fig. 4.3(b)). It can be assumed that this would cause a large number of dimers to align with the applied field (though not necessarily all) introducing a favourable axis to the system via the external magnetic field. The slow magnetic relaxation can be explained in terms of a model Hamiltonian based on the Ni–Tb dimer,

$$\mathcal{H} = \mathcal{J}_{\mathrm{NiTb}} \boldsymbol{S}^{\mathrm{Ni}} \cdot \boldsymbol{J}^{\mathrm{Tb}} - D_{\mathrm{Dimer}} J_z^2 + g\mu_0\mu_{\mathrm{B}} \boldsymbol{J} \cdot \boldsymbol{H}, \tag{4.7}$$

where $J$ is the dimer total angular momentum and $g$ is the dimer g-factor. An antiferromagnetic dimer exchange ($\mathcal{J}_{\mathrm{NiTb}} > 0$) means the low-spin $J = 5$ state will be favoured with the dimer anisotropy, $D_{\mathrm{Dimer}}$, resulting from the coupled anisotropic moments of $Ni^{2+}$ and $Tb^{3+}$. Since the anisotropy of $Tb^{3+}$ is expected to dominate and has been identified as easy plane, the dimer anisotropy is also expected to be easy plane yielding a non-degenerate ground-state with $J_z = 0$.

In this model, for small d.c. magnetic fields the ground-state remains a non-degenerate $J_z = 0$ state due to the lack of significant perturbation and no strong slow magnetic relaxation is obtained. This is what has been observed with the small amount of frequency dependence observed at the lowest temperatures of $Ni_4Tb_4$ for $\mu_0 H_{\mathrm{d.c.}} \leq 0.1$ T (Figs. 4.22(a)–(d)) likely due to other small effects not accounted for. When a d.c. magnetic field is applied along the $z$-axis (perpendicular to the easy plane) the $J_z = 0$ ground state is unaffected but the first excited $J_z = \pm 1$ states split. As the field increases, this Zeeman splitting increasing causing the $J_z = -1$ first excited state to close the gap with the $J_z = 0$ state

(assuming $g > 0$). A level crossing would be obtained which would be accompanied by a sharp increase of magnetisation. In a polycrystalline sample (which has been measured) this is broadened and rounded from the sharp feature expected due to the random orientations of each grain meaning the d.c. magnetic field is applied at all angles to the $z$-axis. Non-zero temperatures also reduce this sharpness. Thus, the increase in magnetisation in Fig. 4.15(b) for $Ni_4Tb_4$ in the region of $\mu_0 H_{\mathrm{d.c.}} \sim 0.6$ T can be attributed to a magnetic ground state being adopted with the $J_z = 0$ and $J_z = -1$ states being brought into degeneracy or near degeneracy. Slow magnetic relaxation may exist in this region due to thermal processes as dimers switch between $J_z = 0$ and $-1$ states in the oscillating a.c. magnetic field. On further increase of the d.c. field the degeneracy is broken and a non-degenerate ground state (now $J_z = -1$) is recovered. This is supported by the drop of $\chi''$ above $0.6$ T (Fig. 4.23(a)). Therefore, the qualitatively similar a.c. response of $Ni_4Tb_4$ at $\mu_0 H_{\mathrm{d.c.}} = 0.59$ T to that of $Ni_4Dy_4$ at $\mu_0 H_{\mathrm{d.c.}} = 0.14$ T presents an interesting demonstration of two different examples of field-induced slow relaxation originating from different effects.

### 4.3.5 Conclusion

The magnetic properties of heterobimetallic family $[Ln_4Ni_4(H_3L)_4(\mu_3\text{-}OH)_4(\mu_2\text{-}OH)_4]4Cl{\cdot}xH_2O{\cdot}yCHCl_3$ with $Ln^{3+}$ = $Dy^{3+}$ ($x = 30.6$, $y = 2$), $Tb^{3+}$ ($x = 28$, $y = 0$), $Gd^{3+}$ ($x = 25.3$, $y = 0$) and $Ho^{3+}$ ($x = 30.6$, $y = 3$) were shown by a.c. and d.c. magnetometry to differ between the members of the family.

The magnetic behaviour of $Ni_4Gd_4$ was found to be dominated by $Ni^{2+}$ single-ion anisotropy with the contributions from the $Gd^{3+}$ reduced at low temperatures due an antiferromagnetic dipolar interaction between them. $D_{\mathrm{Ni}}/k_{\mathrm{B}}$ was found to be easy-plane from a lack of slow magnetic relaxation in a.c. measurements and estimated as $|D_{\mathrm{Ni}}|/k_{\mathrm{B}} = 6.7(7)$ K. This result was assumed to be approximately constant across all members of the series.

$Ni_4Ho_4$ exhibited a non-zero lanathanide single-ion anistropy much greater

Table 4.6: Summary of results from the $Co_2Ln$ family.

| Sample | $D_{\mathrm{Ln}}$ | $E_{\mathrm{a}}/k_{\mathrm{B}}$ (K) | $\tau_0$ (s) |
|---|---|---|---|
| $Co_2Gd$ | $0$ | N/A | N/A |
| $Co_2Er$ | $> 0$ (Easy Axis) | $\geq 9.9(8)$ | $\leq 8 \times 10^{-7}$ |
| $Co_2Tb$ | $> 0$ (Easy Axis) | $\geq 15.6(4)$ | $\leq 3 \times 10^{-7}$ |
| $Co_2Ho$ | $< 0$ (Easy Plane) | N/A | N/A |

than that of $Ni^{2+}$ visible in the higher temperature decrease of $\chi T$ as compared to $Ni_4Gd_4$. No evidence of Ni–Ho interactions was found in d.c. magnetometry nor was slow magnetic relaxation evident in a.c. measurements supporting the presence of easy-plane $Ho^{3+}$ and $Ni^{2+}$.

A large single-ion anisotropy was found in $Ni_4Dy_4$ attributed to $Dy^{3+}$ ions as well as evidence of a ferromagnetic Ni–Dy exchange below $5\ \mathrm{K}$. As a Kramers ion, a degenerate ground state is guaranteed for $Dy^{3+}$ creating an easy-axis anisotropy necessary for SMM behaviour. Evidence for this kind of slow magnetic relaxation was found in a.c. magnetic susceptibility but only for a small applied d.c. magnetic field suggesting $Ni_4Dy_4$ is a field-induced SMM with slow relaxation suppressed at zero d.c. field by quantum tunnelling.

Similarly, a large $Tb^{3+}$ based single-ion anisotropy was found in $Ni_4Tb_4$ but with evidence of antiferromagnetic Ni–Tb dimer formation in d.c. susceptibility. As a non-Kramers ion analogous to $Ho^{3+}$ at a lattice site not promoting an easy-axis, this anisotropy was suspected to be easy-plane. A.c. measurements at low d.c. magnetic fields confirmed this with no strong slow magnetic relaxation. However, slow relaxation could be induced with a d.c. field of $0.59\ \mathrm{T}$ which was suggested to be due to a level crossing to a magnetic ground state in the easy plane $Ni_4Tb_4$ dimers.

## 4.4 General Conclusion

This section has served to demonstrate the use of d.c. and a.c. magnetometry to determine the presence of SMM-type slow magnetic relaxation in the $Co_2Ln$ and $Ni_4Ln_4$ families with the key results summarised in Tabs. 4.6 and 4.7. Beyond the use of investigating new zero-dimensional molecular magnets for the clear purpose of elucidating

Table 4.7: Summary of results from the $Ni_4Ln_4$ family.

| Sample | $D_{\mathrm{Ln}}$ | Dimerisation | Slow Relaxation | SMM Behaviour |
|---|---|---|---|---|
| $Ni_4Gd_4$ | $0$ | Little Evidence | None | N/A |
| $Ni_4Ho_4$ | $< 0$ (Easy Plane) | No Evidence | None | N/A |
| $Ni_4Dy_4$ | $> 0$ (Easy Axis) | Ferromagnetic | Yes | Yes |
| $Ni_4Tb_4$ | $< 0$ (Easy Plane) | Antiferromagnetic | Yes | No |

properties that may lead to improved blocking temperatures it has offered clear examples of the a.c. response of SMMs. Beginning with the $Co_2Ln$ family allows examination of a near ideal a.c. response obeying the generalised Debye model. Furthermore, beginning with compounds in which magnetism arises from a single ion allowed the setting out of various methods for considering the origins of the a.c. response in d.c. magnetometry and structure. Continuing with the $Ni_4Ln_4$ family shows how these same methods may be applied to systems that may contain magnetic exchange. Furthermore, despite this increased complexity these techniques make considerable headway in this family, identifying SMM behaviour and suggesting origins of its presence (or lack thereof).

# Chapter 5

# Layer-based Magnetism in the $Li_{1-x}Fe_x(OH)Fe_{1-y}Se$ Family

## 5.1 Introduction

Superconductors have a very clear practical use in the modern world. As mentioned in Section 1.5 the dissipationless flow of current is an extremely attractive feature for applications in power generation and electrical transport [10, 11]. Thus, a great deal of research focuses on synthesising new superconductors with greater (and therefore more manageable) $T_c$'s, critical fields and critical currents [10, 11] as well as better workable qualities for use in wires [11]. Iron selenides, as a subset of iron-based superconductors, are one such class of materials receiving considerable interest in efforts to raise $T_c$. The parent compound, FeSe, was found to be a superconductor with $T_c \approx 8$ K [128, 129] which has a strong dependence on the precise stoichiometry [129]. It was found by applying hydrostatic pressure [130, 131] or by preparing the compound as a single-layer [132–134] $T_c$ could be increased. Applying pressure has been suggested to change the hybridisation of the Fe and Se orbitals [135] which may indicate electron doping from a $Se^{2-}$ to $Fe^{2+}$ charge transfer driving the increase in $T_c$. Similarly, electron doping either due to O-deficient substrate or Se loss to form $FeSe_{1-x}$ [134] has been suggested to cause $T_c$ enhancement in monolayer FeSe. Furthermore, reduction of bulk FeSe with K atoms also leads to the increase of superconducting $T_c$ [136]. A different method to

alter the FeSe system to increase $T_c$ has been chemical intercalation; the insertion of additional ions or molecules between FeSe layers. By intercalating metal ions, A, to form the family of compounds with formula $A_xFe_2Se_2$ $T_c$'s of approximately $30 - 40$ K have been reached in bulk compounds $A_{0.8}Fe_{1.6}Se_2$ [137–140]. This process may be taken further by intercalating, along with the reducing alkali metal, larger molecules such as ammonia to form $Li_x(NH_2)_y(NH_3)_{1-y}Fe_2Se_2$ and pyridine to form $Li_x(C_5H_5N)_yFe_{2-z}Se_2$ with superconducting transitions of $43$ K [141] and $45$ K [142] respectively. The change of $T_c$ achieved by this method may be considered a result of increased interplanar spacing [143]. Importantly, as the intercalating compound becomes more complex questions may be raised about new physical behaviour that is introduced by inserting additional material between the FeSe layers.

One such example of a more complex intercalated version of FeSe (and the subject of this chapter) is the system of layered hydroxide selenides, $Li_{1-x}Fe_x(OH)Fe_{1-y}Se$ [144–146]. These compounds consist of alternating layers of tetrahedral FeSe and tetrahedral $Li_{1-x}Fe_x(OH)$ (shown in Fig. 5.1) and have the advantage over amine-intercalated compounds of being much more thermally stable. In the FeSe layers the Fe site contains vacancies with previous studies [36, 144] finding these to have a strong effect on the superconducting properties. A notable observation has been that the hydroxide layers always contain a roughly $4:1$ ratio of Li:Fe with a $+2$ oxidation state of iron [144, 146]. A density functional theory (DFT) study suggests that this Li:Fe ratio is favoured to avoid lattice mismatch between the hydroxide and FeSe layers and allow commensurate stacking [147]. Furthermore, other studies [147, 148] have suggested the hydroxide layer iron may play a role in enhancing $T_c$ by increasing charge transfer of $x$ electrons into the FeSe layers providing a similar level of doping to that in the metal/ammonia intercalates.

These particular compounds represent good candidates for study as it has been demonstrated that a certain degree of control may be exercised over their superconducting properties. A post synthetic lithiation may be performed which introduces further Li into the system to displace Fe from the hydroxide layer which in turn fills Fe vacancies in the FeSe layer [144]. Utilising this method, it has been shown that superconductivity in these compounds requires both near stoichiometric FeSe layers ($y < 0.05$) and the

reduction of Fe in this layer below the +2 oxidation state as facilitated by the hydroxide layer Fe [36, 144]. Increased lithiation to form the stoichiometric Li(OH)FeSe was found to destroy superconductivity [36]. A further feature of these compounds has been reports of magnetic order (originating from the hydroxide layers) with both ferromagnetic [146, 149] and antiferromagnetic [145, 150] order being proposed. Magnetism from this layer as also been suggested to couple to and influence the FeSe layer therefore affecting superconductivity [148]. This has been likened to the interaction between interstitial Fe and $FeTe_{1-x}Se_x$ layers in $Fe_{1+y}Te_{1-x}Se_x$ [151].

This chapter details a study of the $Li_{1-x}Fe_x(OH)Fe_{1-y}Se$ family with particular focus on the magnetism of the hydroxide layer rather than the superconducting properties. It will be shown that through contrast between superconducting and non-superconducting variants of this family that (owing to a lack of evidence for long range order in powder neutron diffraction [36, 152]) the magnetism of the hydroxide layer is spin glass-like. This was initially suggested in *Inorg. Chem.*, 2016, **55**, 9886 before the contents of this chapter were published in *Phys. Rev. B*, 2017, **95**, 134419. Synthesis and structural characterisation were performed by D. N. Woodruff, F. Schild, H. Sun and S. J. Clarke. $\mu$SR measurements were performed and analysed by F. K. K. Kirschner, P. J. Baker and S. J. Blundell. E. Suard is thanked for assistance on the D2B beamline at the Institut Laue-Langevin.

## 5.2 Experimental Methods

The structure and composition of each compound were derived from X-ray powder diffraction on the I11 beamline at the Diamond Light Source (Rutherford Appleton Laboratory, UK) with additional neutron powder diffraction performed at the Institut Laue-Langevin (Grenoble, France) on one compound (named NonSC3 in the following). Magnetometry (d.c. and a.c.) were performed using an MPMS as detailed in Chapter 3. Heat capacity measurements were performed using a PPMS on pressed pellets of powders as detailed in Chapter 2. $\mu$SR experiments were performed using a $He^3$ cryostat inserted in the MuSR spectrometer at the ISIS pulsed muon facility (Rutherford Appleton Laboratory, UK) [153]. Zero-field (ZF) measurements were performed in which the

Table 5.1: Compositions of $Li_{1-x}Fe_x(OH)Fe_{1-y}Se$ and lattice parameters of the samples in this study.

| Label | $x$ | $y$ | $a$(Å) | $c$(Å) | Volume(Å$^3$) | Comments |
|---|---|---|---|---|---|---|
| NonSC1 | 0.203(8) | 0.156(7) | 3.8169(1) | 9.1744(6) | 133.665(1) | |
| NonSC2 | 0.207(2) | 0.129(1) | 3.8196(2) | 9.1706(1) | 133.793(2) | |
| NonSC3 | 0.228(2) | 0.078(3) | 3.8054(1) | 9.2014(4) | 133.243(1) | |
| SC1 | 0.162(2) | 0.011(4) | 3.7729(1) | 9.3590(2) | 133.228(2) | |
| SC2 | 0.164(2) | 0.010(3) | 3.7808(1) | 9.3002(2) | 132.947(1) | Deuterated |

Earth's magnetic field of $50$ $\mu$T is cancelled out to better than a few $\mu$T using three mutually perpendicular sets of compensation coils. Thus in a ZF-$\mu$SR experiment, the polarization of incoming muons is measured in the sample in the absence of an external magnetic field. The $\mu$SR data were analyzed using the analysis software WiMDA [154].

## 5.3 Synthesis and Structure

Five powder samples of $Li_{1-x}Fe_x(OH)Fe_{1-y}Se$ (three non-superconductors and two superconductors) were synthesised as detailed in Refs. [144] and [36]. They are henceforth referred to as NonSC1, NonSC2, NonSC3, SC1 and SC2. Non-superconducting samples were synthesised hydrothermally while superconducting samples underwent a post-synthetic lithiation after hydrothermal synthesis to "turn on superconductivity" by generating near stoichiometric FeSe layers via reductive intercalation of Li [144].

Tab. 5.1 shows the precise composition of each studied sample as well as the lattice parameters where $a$ and $c$ are the intralayer and interlayer parameters respectively. It should be noted that SC2 was also the subject of a separate neutron spectroscopy study [155]. The hydroxide layer Fe occupancy takes a similar value for all samples of $x \approx 0.2$ for non-superconductors and $x \approx 0.16$ for superconductors. This can attributed to the post synthetic lithiation performed to produce superconductivity in SC1 and SC2 as this caused hydroxide layer Fe to migrate to the FeSe layer. In contrast, the value of $y$ varies from approximately $0.01 - 0.16$. This agrees with the $x$ and $y$ values of other published work on these compounds [145, 146, 149, 150] and the required $x$ thought to be needed for structural stability [147].

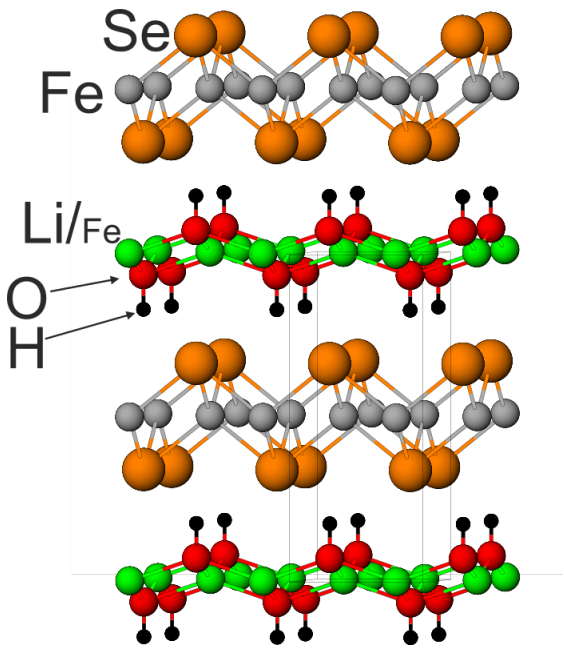



Figure 5.1: Layer structure of $Li_{1-x}Fe_x(OH)Fe_{1-y}Se$. A unit cell is also highlighted.

## 5.4 The Hydroxide Layer

The layered structure of $Li_{1-x}Fe_x(OH)Fe_{1-y}Se$ is shown in Fig. 5.1. The hydroxide layer is comprised of a 2-D network of metal tetrahedra, $M(OH)_4$, compressed along the stacking direction. This results in the the metal ions of the hydroxide layer forming two-dimensional metal sheets. By assuming an Fe occupancy of $x \approx 0.2$ in the hydroxide layer (and with no structural evidence for Li/Fe long range order [36, 152]) the probability that a specified Fe ion was isolated, part of a dimer, part of a trimer, etc, was calculated assuming a random distribution of Li and Fe ions. Fig. 5.2(a) shows this with probabilities plotted as a function of $x$. For the hydroxide layer concentrations spanned by this study ($x \approx 0.16$–$0.23$) the majority of Fe ions exist as isolated ions, though there are also dimers and clusters of greater than three ions. It should be noted that Fig. 5.2(a) shows only the probability that a specified Fe ion is in a cluster of a certain size not the fraction of clusters of a particular size. Thus, despite dimers and clusters of greater than three Fe ions having similar probabilities for this range of $x$, there will be a greater number of dimers.

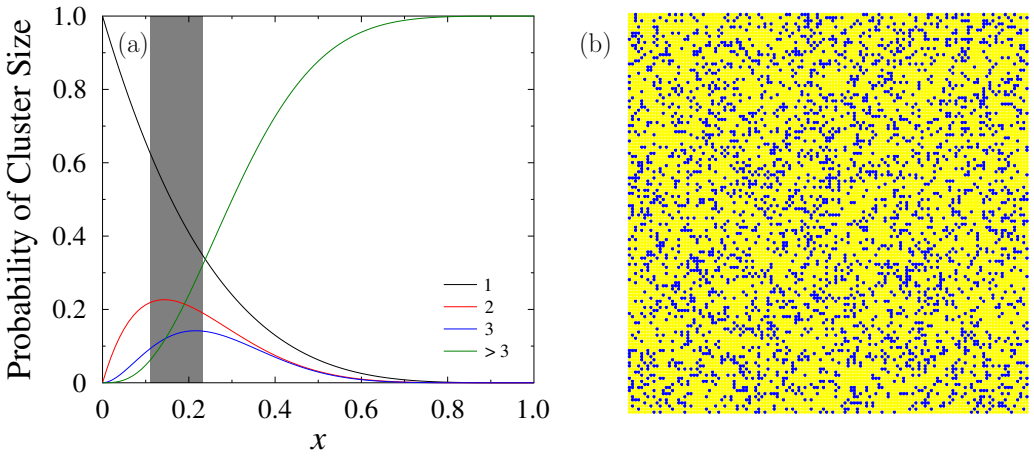



Figure 5.2: (a) Fraction of Fe in the hydroxide layer in clusters of one, two, three and more than three Fe ions given that the initially considered ion is iron. Distribution of Fe in the layer has been assumed random such that the probability of a hydroxide site containing Fe is equal to $x$. Only nearest neighbours have been considered as constituting a cluster. The region of $x$ spanned in this study are highlighted in grey. (b) Graphical representation of the 2-D hydroxide layer with $x = 0.2$, Li = yellow and Fe = blue.

To visualise the distribution of Fe ions in the hydroxide layer Fig. 5.2(b) was produced for $x = 0.2$ depicting Li as yellow and Fe as blue. A large number of clusters of varying sizes may be seen with no long range network across the sample (if only nearest neighbour interactions are considered), consistent with $x$ being well below the percolation threshold ($x_c = 0.5927$) for a two-dimensional square lattice [156, 157]. Thus long range magnetic order sustained by nearest-neighbour interactions would not be expected. Even taking into account longer range interactions, the competition that would arise between clusters due to differing cluster size, interaction type (ferromagnetic or antiferromagnetic), and possible anisotropies in each cluster seems to lead to a more disordered ground state than simple long range magnetic order that may have frustration. This analysis supports a spin glass-like magnetic interpretation of the hydroxide layer.

## 5.5 D.C. Magnetometry

Initial d.c. magnetic characterisation measurements are shown in Figs. 5.3(a) and (b). SC1 and SC2 both show a strong superconducting transition in Fig. 5.3(a)

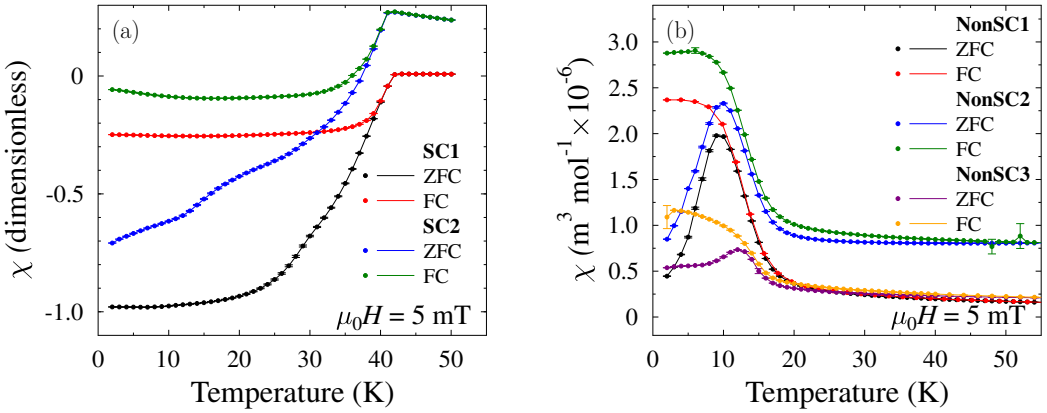



Figure 5.3: (a) Magnetic susceptibility, $\chi$, of superconducting samples SC1 and SC2 measured in a d.c. magnetic field of $\mu_0 H = 5$ mT. While an exact demagnetising factor is unknown an estimate of $\approx 0.4$ has been made by referring to the demagnetising factor of spherical particles in a cuboid container spanning values of 0.33–0.43 [158]. (b) Magnetic susceptibility, $\chi$, of non-superconducting samples NonSC1, NonSC2 and NonSC3 measured in a d.c. magnetic field of $\mu_0 H = 5$ mT. Due to smaller signal no demagnetising factor correction has been performed.

with a $T_c$ of approximately 40 K. Furthermore, both show high diamagnetic shielding at low temperatures demonstrating they are high $T_c$ FeSe superconductors with high volume fractions. NonSC1, NonSC2 and NonSC3 show no superconducting signature but instead a ZFC peak (henceforth referred to as $T_p$) in the range of 9 to 12 K accompanied by a divergence of ZFC and FC sweeps.

The presence of both ZFC peaks at $\approx$ 10 K and a divergence between ZFC and FC sweeps is suggestive of the development of at least some type of local magnetic order but does not distinguish between ferromagnetic or spin glass-like behaviour [61]. A similar ZFC peak in this temperature region has been detected in superconducting variants of these compounds which was interpreted as being due to long range ferromagnetic order [146]. However, a ZFC peak is not present in SC1 or SC2 nor in other members of this family of compounds [144, 145]. This suggests that this peak is fairly sensitive to $x$ as it has been detected in a previously reported member of this family which superconducts with $x \approx 0.2$ [146]. In fact, it may be that since the diamagnetic signal due to superconductivity is much greater than the magnetic signals at $T_p$ of the non-

superconductors it may be that such a feature is present in SC1 and SC2 but it is too weak to be detected. This is investigated in Fig. 5.4(a) in which the d.c. susceptibility sweeps of SC1 and NonSC1 have been plotted in the same units. The low temperature feature of NonSC1 is very small relative to the superconducting signal of SC1. If the magnitude of this is in some way related to $x$ it can be expected that the lower $x$ of the superconducting compounds produces an even smaller signal.

A separate study of a superconducting member of this family which did not display a similar peak in a d.c. magnetic field of $\mu_0 H = 1\ \mathrm{mT}$ was shown to display very similar susceptibility to the non-superconductors with a ZFC peak at $8.6\ \mathrm{K}$ accompanied by a divergence of ZFC and FC sweeps when measured in a high d.c. magnetic field of $\mu_0 H = 1.0\ \mathrm{T}$ [145]. This was explained by the $1.0\ \mathrm{T}$ field suppressing superconductivity and allowing only the hydroxide layer magnetism to be observed, which was interpreted in Ref. [145] as canted antiferromagnetism. Therefore, it was tested if a similar effect could be detected for SC1. This is shown in Fig. 5.4(b) and while superconductivity has not been completely suppressed, partial suppression has been accomplished indicating that $H_{\mathrm{c1}} < H < H_{\mathrm{c2}}$. Furthermore, a very asymmetric peak at approximately $T_{\mathrm{p}}$ is present which moves to lower temperatures with increased field as well as a divergence between ZFc and FC sweeps. These features suit a spin glass description of the system. During the ZFC sweep the moments of the hydroxide layer at low temperatures are frozen in random orientation with no net magnetisation with the superconductor contribution being a result of the intermediate state (hence partial diamagnetic shielding). On warming through $T_{\mathrm{p}}$ (which can be identified as the spin glass freezing temperature, $T_{\mathrm{f}}$) the moments become unfrozen and align with the applied field resulting in an enhancement of the magnetic field the superconducting FeSe layers experience further suppressing superconductivity. This suppresion is not complete as a small anomaly at $T_{\mathrm{c}}$ can still be

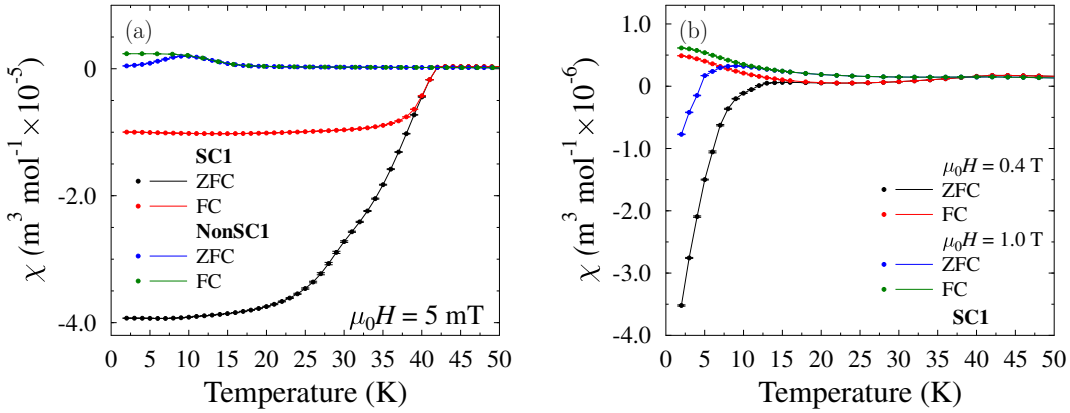



Figure 5.4: (a) Magnetic susceptibility, $\chi$, of samples SC1 and NonSC1 measured in a d.c. magnetic field of $\mu_0 H = 5$ mT from Fig. 5.3(a) and (b) plotted with the same units for comparison. (b) Magnetic susceptibility, $\chi$, of superconducting sample SC1 measured in d.c. magnetic fields of $\mu_0 H = 0.4$ T and $\mu_0 H = 1.0$ T.

detected, resulting in a small minimum occurring between $T_\mathrm{p}$ and $T_\mathrm{c}$. During the FC sweep by cooling in the applied field the hydroxide layer moments are frozen aligned with the magnetic field resulting in near complete suppression of superconductivity even at 2 K (though a small anomaly persists at $T_\mathrm{c}$).

## 5.6 A.C. Magnetometry

The slow dynamics of the proposed spin glass state were investigated using a.c. magnetic susceptibility. Measurements on NonSC1 are shown in Figs. 5.5(a) and (b) as the real part of the susceptibility and the imaginary part of the susceptibility respectively. The frequency dependence of $\chi'$ develops only below $T_\mathrm{p}$ and is accompanied by a set of frequency dependent peaks in $\chi''$. This bears strong similarity to the frequency dependence of SMMs [31, 32] and spin glasses [32, 37, 61] as described in Sections 3.4.1 and 3.4.2. To differentiate between these two possibilities the movement of the real peak, $\chi'(T)$ was quantified using Eq. 3.46 yielding $f = 0.016(1)$ which is consistent with a spin glass [31, 37].

This supports a spin glass description of the slow magnetic relaxation in this compound. A Cole-Cole plot was produced to investigate this further. This is shown in Fig. 5.5(c) and notably only small slices of what appear to be isother-

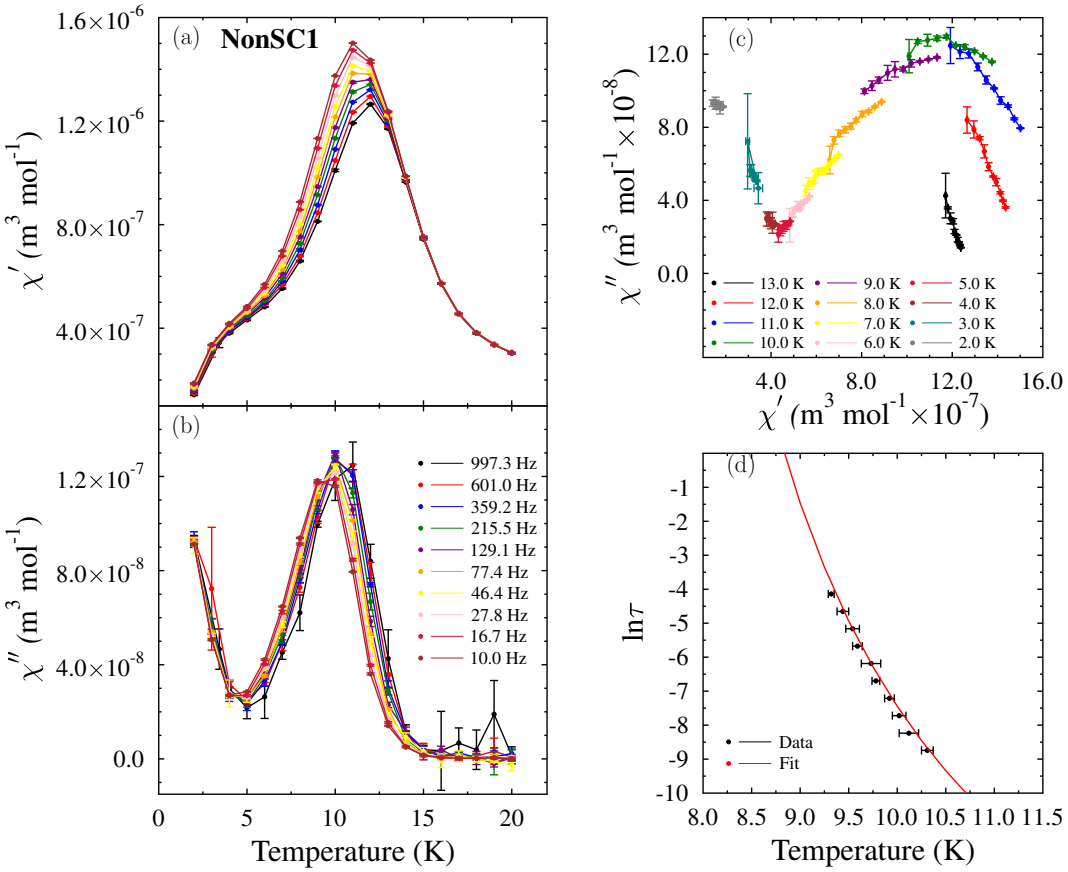



Figure 5.5: (a) and (b) show a.c. susceptibility of NonSC1 as measured at $\mu_0 H_{\mathrm{d.c.}} = 0$ T with an a.c. magnetic field amplitude of $\mu_0 H_{\mathrm{a.c.}} = 0.4$ mT. (a) shows the real/in-phase parts of susceptibility, $\chi'$, while (b) shows the imaginary/out-of-phase parts of susceptibility, $\chi''$. (c) Cole-Cole plot of a.c. susceptibility shown in (a) and (b). (d) Temperature of $\chi''$ peaks from (b) plotted with fit to Volger-Fulcher law where $\tau = 1/\omega$. These were determined by Gaussian fits to the peaks from $7 - 13$ K.

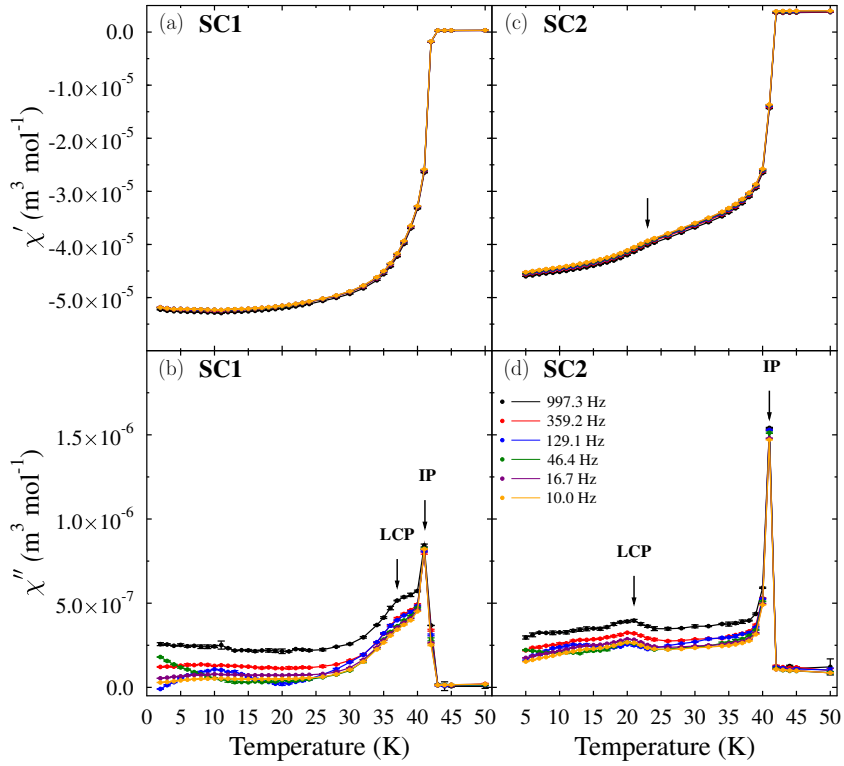



Figure 5.6: A.c. susceptibility of superconducting compounds as at $\mu_0 H_{\mathrm{d.c.}} = 0$ T with an a.c. magnetic field amplitude of $\mu_0 H_{\mathrm{a.c.}} = 0.4$ mT. (a) and (b) show the real/in-phase and imaginary/out-of-phase parts or susceptibility, $\chi'$ and $\chi''$, of SC1. (c) and (d) show the real/in-phase and imaginary/out-of-phase susceptibility, $\chi'$ and $\chi''$, of SC2.

mal arcs in the region of $T_{\mathrm{p}}$ can be detected. This suggests slow magnetic relaxation with a very broad spread of relaxation times, functioning to distort the arcs from the ideal semicircle of a single relaxation time [31, 61], similar to that observed in spin glasses [37, 61].

Additional anomalies can be identified in Fig. 5.5(a) and (b) as a closing of frequency dependence with a shoulder in $\chi'$ at $\approx 4$ K and upturn in $\chi''$ at $\approx 5$ K. These features are not observed in d.c. measurements. They can be seen in the Cole-Cole plot (Fig. 5.5(c)) as a set of isothermal points that span a very narrow region of $\chi'$. This could suggest the presence of a second, unknown relaxation processes becoming important at lower temperatures though the frequency range available in the MPMS prevents investigation of this.

Analysis of the peaks of $\chi''$ was performed using the Arrhenius law (Eq. 3.43)

and the Vogel-Fulcher law (Eq. 3.45). The Arrhenius fit was found to produce unphysical values (e.g. $E_a/k_B = 470 \pm 10$ K) which was noted to be known for spin glasses in Section 3.4.2 [37, 82, 86]. The Vogel-Fulcher fit (Fig. 5.5(d)) yielded $T_0 = 6.4 \pm 1.2$ K, $\ln \tau_0 = -23 \pm 6$ and $E_a/k_B = 60 \pm 40$ K, the large uncertainty in parameter values resulting from the narrow temperature range over which $\chi''$ peaks exist. As such this supports a spin glass description of the system [82, 86, 87].

A.c. susceptibility measurements of the superconductors SC1 and SC2 are shown in Fig. 5.6. $\chi'$ of each compound (Fig. 5.6(a) and (c)) both show strong superconducting transitions though a small anomaly can be detected as a broad hump for SC2 in the region of $25$ K (arrow in Fig. 5.6(c)). The out-of-phase susceptibility (Fig. 5.6(b) and (d)) of SC1 and SC2 appear very similar with a small, slightly non-zero $\chi''$ above $T_c$, a sharp and seemingly frequency independent peak at $T_c$ and an approximately steady, non-zero $\chi''$ at all lower temperatures. SC1 shows a shoulder just below $T_c$ while SC2 shows a bump at $\approx 20$ K (both indicated in Fig. 5.6(b) and (d)).

Section 3.4.6 described various ways superconductors may show a frequency dependent a.c. response. However, the quality of these measurements was insufficient to show any superconductivity related frequency dependence. Assuming the hydroxide layer magnetism and selenide layer superconductivity are well separated (since they are based on separate structural layers) it would be expected for a.c. behaviour to be a superposition of that for superconductivity and the glass-like slow relaxation detected in non-superconducting variants. Therefore, the series of frequency dependent peaks of $\chi''(T)$ observed in NonSC1 would be expected to be superimposed upon a superconducting $\chi''(T)$ only non-zero in the region of $T_c$. Thus with good separation in temperature between $T_p$ and $T_c$ a set of spin glass peaks would be expected around $T_p$ in superconducting compounds. This is not observed in Fig. 5.6(b) or (d), perhaps due to the

large non-zero $\chi''$ of each superconductor masking low temperature peaks or the lower iron concentration of the hydroxide layer of the superconductors or due to grain effects. Indeed, the two sets of peaks identified in $\chi''$ for both SC1 and SC can be associated with the superconducting transitions of the bulk sample (the intrinsic peak, IP) and grain boundaries (lower coupling peaks, LCP) [34, 110]. A bulge in $\chi'$ at a slightly higher temperature accompanies the LCP and this is highlighted by an arrow for SC2. For SC1 this is hidden by the rapid drop of $\chi'$ at $T_{\mathrm{c}}$.

## 5.7 Heat Capacity

Heat capacity measurements were performed on one non-superconductor (Non-SC2) and two superconductors (SC1 and SC2). Due to both superconductors showing similar behaviour the full region of interest is shown for only SC2 (see Fig. 5.7(a) and (b)). Unexpectedly, no feature can be distinguished in heat capacity of SC2 at $T_{\mathrm{c}}$ with no significant change when a d.c. magnetic field of $11\ \mathrm{T}$ was applied. The primary visible feature in heat capacity is a low temperature bump with a peak at $\approx 5\ \mathrm{K}$. In high magnetic fields the magnitude of this bump is suppressed and it is broadened and moved to higher temperatures. Plotting data as $C/T$ (Fig. 5.7(b)) accentuates the bump and perhaps shows a small anomaly at $T_{\mathrm{c}}$ (indicated by an arrow) though this may be an experiment artefact. The lack of a distinct feature at $T_{\mathrm{c}}$ for these compounds is not entirely unexpected. Elemental FeSe shows only a small heat capacity anomaly at $T_{\mathrm{c}}$ [159] and investigations of $Ba_{0.8}Fe_2Se_2$ [140] and LiFeAs [17] demonstrates the difficulty of detecting anomalies at $T_{\mathrm{c}}$ in iron-based superconductors. Furthermore, the Sommerfeld coefficient (obtained from third order polynomial fits to $C/T$ vs. $T$ from $13-50\ \mathrm{K}$ for $0\ \mathrm{T}$ data) for SC1 and SC2 was found to be $\gamma = 3(6)$ and $0.0(7)\ \mathrm{mJ\ mol^{-1}\ K^{-2}}$ for each compound respectively. Due to the low temperature anomaly limiting the lower bounds of the fits and the temperature region

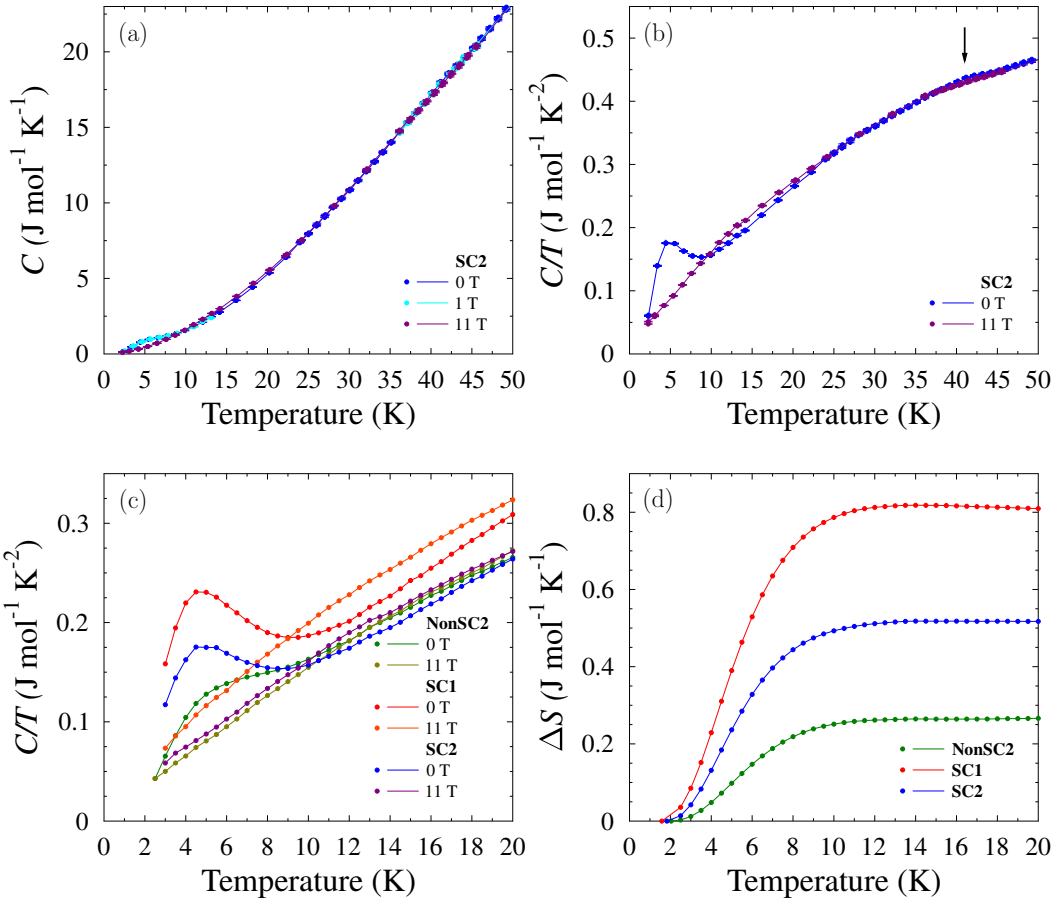



Figure 5.7: (a) Heat capacity of SC2 measured at various static magnetic fields ($\mu_0 H_{\mathrm{d.c.}} = 0, 1$ and 11 T). No anomaly can be observed at $T_{\mathrm{c}}$. (b) $C/T$ vs. $T$ of SC2 at magnetic fields of $\mu_0 H_{\mathrm{d.c.}} = 0$ and 11 T. An anomaly at $T_{\mathrm{c}}$ may exist in the form of a very subtle bulge indicated by an arrow. (c) $C/T$ vs. $T$ of NonSC2, SC1 and SC2 at magnetic fields of $\mu_0 H_{\mathrm{dc}} = 0$ and 11 T. (d) Entropy change for NonSC2, SC1 and SC2 obtained as detailed in text.

lying within the superconducting regime, exact determination of $\gamma$ is difficult with uncertainties likely larger than those quoted from polynomial fits. An upper bound may be placed on $\gamma$ of $\approx 50\ \mathrm{mJ\ mol^{-1}\ K^{-2}}$ by projecting $0\ \mathrm{T}$ data of Fig. 5.7(c) to $T = 0\ \mathrm{K}$. These suggest SC1 and SC2 show a very small electronic contribution to heat capacity. It can be noted that a similar small and difficult to detect anomaly was found in the compound LiFeAs [17]. As such, the lattice contributions in these compounds may be much greater which, combined with the smearing out of features due to the samples being pressed pellets, hides an anomaly at $T_\mathrm{c}$. These results are in agreement with those reported in a separate investigation [145] in which heat capacity was measured in the range $2 - 20\ \mathrm{K}$ for a superconducting sample with a similar composition.

The low temperature anomaly is shown in Fig. 5.7(c) (as $C/T$) for NonSC2, SC1 and SC2. Each shows the same anomaly at $5 - 6\ \mathrm{K}$ and share the behaviour that it is suppressed in magnitude and broadened at higher applied magnetic fields. The data shown are the interpolated results of several sweeps which facilitates the subtractions needed for the calculation of entropy. Slight variations between samples may be attributed to small errors when determining pellet masses or background contributions with the larger high temperature values of SC1 perhaps indicating a more homogeneous sample. This may be related to the fact that SC1 showed the greatest superconducting volume fraction in Fig. 5.3(a). These broad peaks extend to temperatures up to $\approx T_\mathrm{p}$ and may therefore be identified as originating from the same feature detected in magnetometry. SC1 and SC2 (with $x \approx 0.16$) show the sharpest peaks while the peak for NonSC2 (with $x \approx 0.21$) is much weaker being better described as a shoulder. This would seem to suggest that as $x$ increases this feature weakens. However, this anomaly in $C/T$ has been detected in a superconducting member of this family with $x = 0.2$ with similar sharpness to SC1 and SC2 [145]. Thus it does not appear to be a variance in $x$ which controls this feature. Instead it appears that the factors

which favour superconductivity in these compounds also favour an enhanced entropy change due to the magnetic state of the hydroxide layers.

The form of this feature (with a suppression and broadening in magnetic fields) is reminiscent of spin glasses [61] though it occurs over a narrower temperature range than expected [37, 160]. The magnetic contribution to $C/T$ was calculated by fitting a third order polynomial to the $0$ T $C/T$ data for each sample from $13-50$ K. This was then subtracted from each $0$ T dataset from $2-20$ K yielding $\Delta C/T$. Linear extrapolation extended $\Delta C/T$ to zero using the two lowest temperature points available from each heat capacity sweep. Integration of this (using $\Delta S = \int_0^T (\Delta C/T)\mathrm{d}T$) yielded the change in entropy due to the magnetic feature as shown in Fig. 5.7(d). While these values may be considered as lower bounds on $\Delta S$ since the lowest available temperature was $\sim 2$ K they are considerably lower than expected. If the entropy change through a magnetic transition is defined as $\Delta S = xR\ln[2J+1]$ (where $R$ is the gas constant, $x$ the Fe concentration of the hydroxide layer and $J$ is the effective spin of the magnetic moments in the system [160]) this can be used to predict a value of $J$ for these transitions (shown in Tab. 5.2). These values of $J$ all lie below the value for one free electron $(1/2)$ though it can be acknowledged that uncertainties are likely slightly underestimated due to the fitting procedure employed to find $\Delta C/T$. Furthermore, the spin expected from crystal field theory for the $Fe^{2+}$ ions in a tetrahedral coordination is $2$ and DFT calculations predict a moment of $\approx 3.5\ \mu_\mathrm{B}$ for hydroxide layer Fe [147, 148]. This underestimation of spins is a known feature of spin glasses due to a great deal of the entropy change associated with spin freezing occurring at temperatures above $T_\mathrm{f}$ [37, 61] and has been detected in the canonical spin glass CuMn [160]. This lends further support to the hydroxide layer displaying spin glass-like behaviour rather than the canted antiferromagnetism previously associated with this feature [145]. Importantly, since this feature exists in both superconducting and non-superconducting sam-

Table 5.2: Entropy change from low temperature transition and predicted moments of the hydroxide layer from Fig. 5.7(d). $\Delta S$ has been obtained from linear fits between the temperatures of $13 - 20$ K with gradient fixed to $0$.

| | $\Delta S$ (J mol$^{-1}$ K$^{-1}$) | Spin ($J$) |
|---|---|---|
| NonSC2 | 0.2646(2) | 0.083(3) |
| SC1 | 0.7856(9) | 0.396(8) |
| SC2 | 0.5166(3) | 0.230(7) |

ples this suggests a magnetic state coexisting with superconductivity.

## 5.8 ZF-$\mu$SR

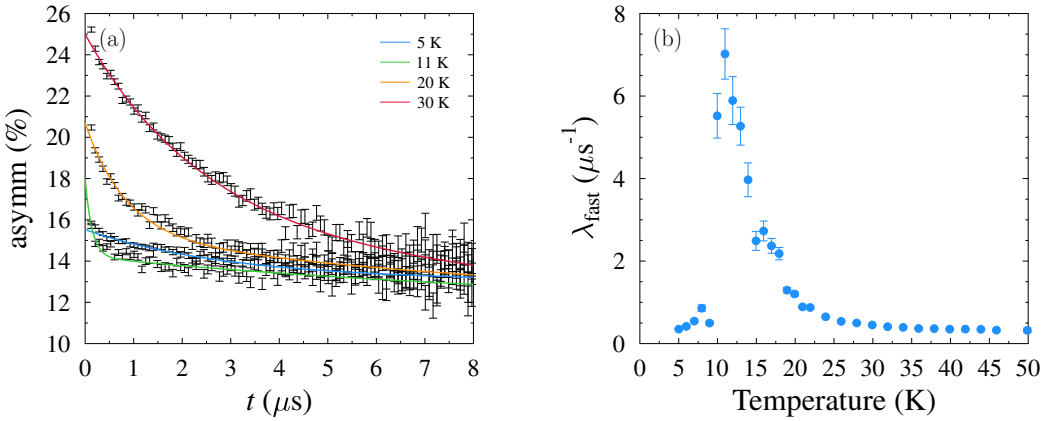



Figure 5.8: (a) Asymmetry of muons at various temperatures in zero magnetic field as measured in NonSC3. (b) Fast relaxation rates, $\lambda_{\text{fast}}$, of muons at various temperatures from fits to data as shown in (a). Data analysed by F. K. K. Kirschner.

Example ZF-$\mu$SR spectra for NonSC3 are shown in Fig 5.8(a). Clearly no oscillations are present at the investigated temperatures or Kubo-Toyabe-like relaxation suggesting a lack of long range order or static magnetism [26, 27]. It should be noted that as this measurement was performed at the ISIS pulsed muon facility, the pulsed structure of the muon beam precluded observation of precession signals faster than about 10 MHz.

Data were fitted with a two-component exponential relaxation function

$$A(t) = A_1 \exp\left(-\lambda_{\text{fast}} t\right) + A_2 \exp\left(-\lambda_{\text{slow}} t\right). \tag{5.1}$$

Here there is a slow-relaxing term with amplitude $A_2$ and relaxation rate $\lambda_{\text{slow}}$

associated with the background and a fast-relaxing term with amplitude $A_1$ and relaxation rate $\lambda_{\mathrm{fast}}$. As can be seen in Fig. 5.8(a) the quality of these fits decreases as temperature is lowered precluding strong conclusions. However, it can be tentatively noted that the fast relaxation rate appears to change in the region of $T_{\mathrm{p}}$ suggesting that these $\mu$SR measurements are detecting the same magnetic feature as observed in d.c. and a.c. susceptibility and heat capacity measurements.

As described in Section 2.3, an exponential relaxation implies moments fluctuating fast in comparison to the muon timescale and an unknown field distribution [161] or a dilute distribution of static moments [162]. As such, these measurements do not indicate the presence of long magnetic order and do not disagree with a spin glass-like state of the hydroxide layer iron moments. For a complete investigation of this feature using $\mu$SR further measurements must be carried out at a continuous wave muon source with higher resolution in time.

## 5.9 Conclusion

The magnetic behaviour of the $Li_{1-x}Fe_x(OH)Fe_{1-y}Se$ family was elucidated by studying both superconducting and non-superconducting members. D.c magnetometry revealed a low temperature feature common to both superconductors and non-superconductors which could therefore be attributed to the Fe ions present in the hydroxide layer. A.c. magnetometry of a non-superconducting variant showed spin glass-like slow relaxation to be present which was further suggested by heat capacity measurements which also showed this feature to coexist with superconductivity. Furthermore, $\mu$SR showed support to a spin glass-like feature and not a form of long magnetic order that has been previously reported.

In the context of this thesis this study presents an example of several techniques (a.c. susceptibility included) used in tandem to study a magnetic state

containing slow magnetic relaxation. It is of particular interest due to the spin glass nature of the slow magnetic relaxation (which is of an inherently different origin to that in SMMs) and the unique feature of this magnetic state coexisting with a superconducting state but based on neighbouring layers.

# Chapter 6

# Concluding Remarks

This thesis serves to describe the characterisation of the magnetic properties of materials specifically discussing the use of a.c. susceptibility for the study of slow magnetic dynamics. By beginning with electrons possessing non-zero angular momentum as the building blocks of condensed matter magnetism I have briefly outlined the necessary theory needed to understand different forms of magnetism. This has provided the foundation upon which to consider a.c. magnetometry and the various types of material that can show a distinct a.c. response.

Via contrast of d.c. and a.c. magnetometry I have shown that the two techniques may yield the same information when a studied system's dynamics lie outside the timescale of both measurements. However, when the system contains slow magnetic dynamics within the frequency range of the a.c. probe, a.c. magnetometry offers a wealth of information. Furthermore, by utilising linear response theory I have demonstrated that the ideal Debye model (often used to describe slow relaxing behaviour in dielectrics or magnetisation) may arise using only the assumption that the property of interest (magnetisation for magnetism) decays exponentially with a single relaxation time showing the wide applicability of the theory. The expected deviations from this model in real systems were also discussed in the context of distributions of relaxation times. Having outlined the

theoretical approaches to modelling a.c. susceptibility data I undertook a brief review of various types of material that may show slow relaxation with the aim to highlight similarities and differences in their response as well as identify the source of the magnetic sluggishness.

Finally, I presented the results of a.c. susceptibility practically applied in the studies of two classes of material. First, two families of zero-dimensional magnets with the potential for single-molecule magnet behaviour were examined. These were a useful platform for testing a.c. susceptibility since their isolated, molecular nature bore a close resemblance to the non-interacting ideal Debye model. The simpler $Co_2Ln$ family (Ln = Gd, Ho, Tb and Er) showed field-induced slow magnetic relaxation only in the Tb and Er analogues due to the central $Ln^{3+}$ ions (the $Co^{3+}$ ions being diamagnetic). D.c. magnetometry and structural considerations identified this slow relaxation to be indicative of single-molecule magnet behaviour with an easy axis anisotropy not present in the compounds with spherically symmetric $Gd^{3+}$ ions or with $Ho^{3+}$ ions (which show easy plane anisotropy). This prescribed a method for investigating the more complex $Ni_4Ln_4$ family (Ln = Gd, Ho, Dy, and Tb). An analysis of the possible exchange pathways suggested the formation of Ni–Ln dimers, though d.c. magnetometry suggested these only formed in $Ni_4Dy_4$ and $Ni_4Tb_4$ with ferromagnetic and antiferromagnetic dimer exchange respectively. Regardless, $Ln^{3+}$ anisotropy was expected to dominate any a.c. response with both $Ni_4Dy_4$ and $Ni_4Tb_4$ displaying field-induced slow relaxation. However, d.c. magnetometry suggested this originated from single-molecule magnet behaviour only in the $Dy^{3+}$ analogue with the $Tb^{3+}$ compound owing its slow relaxation to a level crossing induced by a d.c. magnetic field. Thus, this provided a practical example of a similar a.c. response regardless of the different local anisotropies.

The second study I presented elucidated the low temperature magnetism associated with the layered superconductor family $Li_{1-x}Fe_x(OH)Fe_{1-y}Se$ via the

measurement of both superconducting and non-superconducting variants. Rather than long range magnetic order originating from the hydroxide layer $Fe^{2+}$ ions I suggested a spin glass-like state which was supported by d.c. magnetometry and heat capacity measurements. Furthermore, a.c. susceptibility showed a response consistent with a spin glass with ZF-$\mu$SR suggesting the presence of distributions of relaxation times as expected of a spin glass. This is an especially interesting state as it coexists with superconductivity on separate layers.

Thus, this thesis has set out the tools to understand a.c. magnetic susceptibility from both a theoretical and experimental stance. A short survey of the literature shows the rich number of materials that can be probed by a.c. susceptibility with the two studies presented demonstrating this in single-molecule magnets and spin glasses. Importantly, this demonstrates that a.c. susceptibility works in tandem with other well known techniques for material characterisation such as d.c. magnetometry and calorimetry.

# Appendix A

# The Generalised Debye Model

The generalised Debye model (Eq. 3.28) was given by

$$\chi(\omega) = \chi_{\mathrm{S}} + \frac{\chi_{\mathrm{T}} - \chi_{\mathrm{S}}}{1 + (\mathrm{i}\omega\tau)^{1-\alpha}}. \tag{A.1}$$

This can be re-written by defining $\psi = (\omega\tau)^{1-\alpha}$ and noting $i^a = (\exp\{\pi/2\})^a$ according to Euler's formula where $a$ is some constant. Thus, $(i\omega\tau)^{1-\alpha} = \psi(\sin\frac{\pi\alpha}{2} + \mathrm{i}\cos\frac{\pi\alpha}{2})$ allowing the separation of the generalised Debye model into real and imaginary parts

$$\chi'(\omega) \;=\; \chi_{\mathrm{S}} + \frac{(\chi_{\mathrm{T}} - \chi_{\mathrm{S}})(1 + \sin\frac{\pi\alpha}{2}\psi)}{1 + 2\psi\sin\frac{\pi\alpha}{2} + \psi^2} \tag{A.2}$$

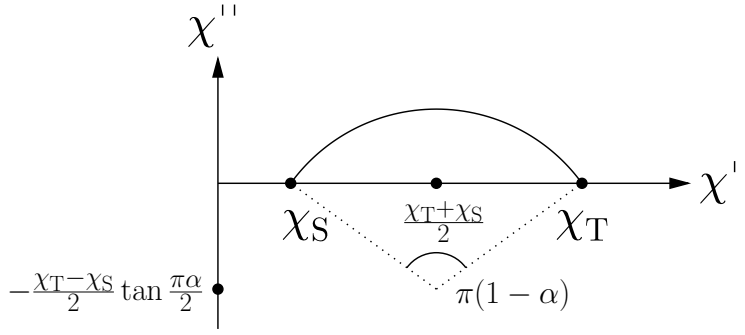



Figure A.1: Schematic of the generalised Debye model.

$$\chi''(\omega) = \frac{(\chi_T - \chi_S)\psi \cos\frac{\pi\alpha}{2}}{1 + 2\sin\frac{\pi\alpha}{2}\psi + \psi^2.} \tag{A.3}$$

This can be altered further by introducing the identities

$$\frac{\psi + \psi^{-1}}{2} = \cosh[(1-\alpha)\ln(\omega\tau)] \tag{A.4}$$

$$\frac{\psi - \psi^{-1}}{2} = \sinh[(1-\alpha)\ln(\omega\tau)]. \tag{A.5}$$

This allows the imaginary and real parts of the generalised Debye model to be written as

$$\chi'(\omega) = \chi_S + \frac{1}{2}(\chi_T - \chi_S)\left[1 - \frac{\sinh[(1-\alpha)\ln(\omega\tau)]}{\cosh[(1-\alpha)\ln(\omega\tau)] + \sin\frac{\pi\alpha}{2}}\right] \tag{A.6}$$

$$\chi''(\omega) = \frac{\frac{1}{2}(\chi_T - \chi_S)\cos\frac{\pi\alpha}{2}}{\cosh[(1-\alpha)\ln(\omega\tau)] + \sin\frac{\pi\alpha}{2}}. \tag{A.7}$$

These equations can be rearranged to yield

$$\sinh[(1-\alpha)\ln(\omega\tau)] = \frac{((\chi_T + \chi_S)/2 - \chi')\cos\frac{\pi\alpha}{2}}{\chi''} \tag{A.8}$$

$$\cosh[(1-\alpha)\ln(\omega\tau)] = \frac{(\chi_T - \chi_S)\cos\frac{\pi\alpha}{2}}{2\chi''} - \sin\frac{\pi\alpha}{2}. \tag{A.9}$$

Substituting the above equations into the identity $\cosh^2 x - \sinh^2 x = 1$ gives

$$\left(\chi' - \frac{\chi_T + \chi_S}{2}\right)^2 + \chi''^2\sec^2\frac{\pi\alpha}{2} - \left(\chi''\tan\frac{\pi\alpha}{2} - \frac{\chi_T - \chi_S}{2}\right)^2 = 0, \tag{A.10}$$

which can be simplified to using the identity $\tan^2 x + 1 = sec^2 x$ to yield

$$\left(\chi' - \frac{\chi_T + \chi_S}{2}\right)^2 + \left(\chi'' + \frac{\chi_T - \chi_S}{2}\tan\frac{\pi\alpha}{2}\right)^2 = \left(\frac{\chi_T - \chi_S}{2}\sec\frac{\pi\alpha}{2}\right)^2, \tag{A.11}$$

which is the equation of a circle, with centre

$$\left(\frac{\chi_T + \chi_S}{2}, -\frac{\chi_T - \chi_S}{2}\tan\frac{\pi\alpha}{2}\right) \tag{A.12}$$

and radius $\frac{\chi_T - \chi_S}{2} \sec \frac{\pi\alpha}{2}$. This provides the analytical form for the locus in the Cole-Cole plot, as shown in Fig. A.1(a) and also allows the opening angle to be derived as $\pi(1-\alpha)$, as shown. Eq. A.11 can be rearranged to write $\chi''$ as a function of $\chi'$, yielding

$$\chi'' = -\left(\frac{\chi_T - \chi_S}{2} \tan \frac{\pi\alpha}{2}\right) \pm \sqrt{\left(\frac{\chi_T - \chi_S}{2} \tan \frac{\pi\alpha}{2}\right)^2 + (\chi' - \chi_S)(\chi_T - \chi')}, \tag{A.13}$$

which is Eq. (3.38).

# Bibliography


[1] S. J. Blundell, *Magnetism in Condensed Matter* (Oxford University Press, Oxford, 2001).

[2] C. Foot, *Atomic Physics* (Oxford University Press, Oxford, 2014).

[3] K. Yoshida, *The Theory of Magnetism* (Springer-Verlag, Heidelberg, 1991).

[4] O. Kahn, *Molecular Magnetism* (VCH, Publishers, Inc., New York, 1993).

[5] D. C. Mattis, *The Theory of Magnetism I: Statics and Dynamics* (Springer-Verlag, Heidelberg, 1981).

[6] A. H. Morrish, *The Physical Principles of Magnetism* (John Wiley & Sons, Inc., New York, 1965).

[7] A. P. Ramirez, Annu. Rev. Mater. Sci. **24**, 453 (1994).

[8] J. F. Annett, *Superconductivity, Superfluids and Condensates* (Oxford University Press, Oxford, 2013).

[9] R. P. Huenbener, *Magnetic Flux Structures in Superconductors* (Springer-Verlag, Heidelberg, 1979).

[10] A. P. Malozemoff, Nat. Mater. **6**, 617 (2007).

[11] S. R. Foltyn, L. Civale, J. L. Macmanus-Driscoll, Q. X. Jia, B. Maiorov, H. Wang, and M. Maley, Nat. Mater. **6**, 631 (2007).

[12] M. Blackman, Rep. Prog. Phys. **8**, 11 (1941).

[13] J. C. Lashley, M. F. Hundley, A. Migliori, J. L. Sarrao, P. G. Pagliuso, T. W. Darling, M. Jaime, J. C. Cooley, W. L. Hults, L. Morales, D. J. Thoma, J. L. Smith, J. Boerio-Goates, B. F. Woodfield, G. R. Stewart, R. A. Fisher, and N. E. Phillips, Cryogenics **43**, 369 (2003).

[14] S. H. Simon, *The Oxford Solid State Basics* (Oxford University Press, Oxford, 2013).

[15] S. J. Blundell and K. M. Blundell, *Concepts in Thermal Physics* (Oxford University Press, Oxford, 2013).

[16] J. Singleton, *Band Theory and Electronic Properties of Solids* (Oxford University Press, Oxford, 2012).

[17] P. J. Baker, S. R. Giblin, F. L. Pratt, R. H. Liu, G. Wu, X. H. Chen, M. J. Pitcher, D. R. Parker, S. J. Clarke, and S. J. Blundell, New J. Phys. **11**, 025010 (2009).

[18] *Physical Property Measurement System Heat Capacity Option User's Manual*, Quantum Design, San Diego, USA, 11th ed. (2004).

[19] W. Schnelle, J. Engelhardt, and E. Gmelin, Cryogenics **39**, 271 (1999).

[20] J. G. Bunting, T. Ashworth, and H. Steeple, Cryogenics **9**, 385 (1999).

[21] Y. Moriya, H. Kawaji, T. Atake, M. Fukuhara, H. Kimura, and A. Inoue, Cryogenics **49**, 185 (2009).

[22] R. E. Schwall, R. E. Howard, and G. R. Stewart, Rev. Sci. Instrum. **46**, 1054 (1975).

[23] J. S. Hwang, K. J. Lin, and C. Tien, Rev. Sci. Instrum. **68**, 94 (1997).

[24] J. P. Shepherd, Rev. Sci. Instrum. **56**, 273 (1985).

[25] C. A. Kenneddy, M. Stancescu, R. A. Marriott, and M. A. White, Cryogenics **47**, 107 (2007).

[26] S. J. Blundell, Contemp, Phys. **40**, 175 (1999).

[27] A. Yaouanc and P. D. de. Réotier, *Muon spin rotation, relaxation, and resonance: applications to condensed matter* (Oxford University Press, Oxford, 2011).

[28] A. Yaouanc and P. D. de. Réotier, *Muon spin rotation, relaxation, and resonance: applications to condensed matter* (Oxford University Press, Oxford, 2011).

[29] A. Keren, P. Mendels, I. A. Campbell, and J. Lord, Phys Rev. Lett. **77**, 1386 (1996).

[30] B. R. Marting, *Nuclear and Particle Physics* (John Wiley & Sons Ltd, Chichester, 2011).

[31] D. Gatteschi, R. Sessoli, and J. Villain, *Molecular Nanomagnets* (Oxford Univeristy Press, Oxford, 2011).

[32] M. Bałanda, Acta. Phys. Pol. A **124**, 964 (2013).

[33] D. X. Chen, V. Skumryev, and J. M. D. Coey, Phys. Rev. B **53**, 15014 (1996).

[34] M. Nikolo, Am. J. Phys. **63**, 57 (1995).

[35] F. Gömöry, Supercond. Sci. Technol. **10**, 523 (1997).

[36] D. N. Woodruff, F. Schild, C. V. Topping, S. J. Cassidy, J. N. Blandy, S. J. Blundell, A. L. Thompson, and S. J. Clarke, Inorg. Chem. **55**, 9886 (2016).

[37] J. A. Mydosh, *Spin glasses: an experimental introduction* (Taylor & Francis, London, 1993).

[38] C. V. Topping and S. J. Blundell, J. Phys. Condens. Matter (accepted).

[39] *Magnetic Property Measurement System AC Option User's Manual*, Quantum Design, San Diego, USA, 2nd ed. (1999).

[40] *Physical Property Measurement System AC Measurement System (ACMS) Option User's Manual*, Quantum Design, San Diego, USA, 4th ed. (2003).

[41] *Magnetic Property Measurement System AC Option User's Manual*, Quantum Design, San Diego, USA, 2nd ed. (1999).

[42] A. K. Jonscher, J. Mater. Sci. **16**, 2037 (1981).

[43] K. S. Cole and R. H. Cole, J. Chem. Phys. **9**, 341 (1941).

[44] P. Debye, *Polar Moleules* (The Chemical Catalog Company, Inc., New York, 1929).

[45] C. J. Gorter and R. d. L. Kronig, Physica **3**, 1009 (1936).

[46] H. B. G. Casimir and F. K. du Pré, Physica **5**, 507 (1938).

[47] Y. Onodera, J. Phys. Soc. Jpn. **62**, 4104 (1993).

[48] L. D. Landau, E. M. Lifshitz, and L. P. Pitaevskii, *Electrodynamics of Continuous Media* (Pergamon Press, Oxford, 1984).

[49] S. Wang, Phys. Rev. A **60**, 262 (1999).

[50] E. Merzbacher, *Quantum Mechanics* (John Wiley & Sons, Inc., New York, 1998).

[51] L. Pan, N. J. Laurita, K. A. Ross, B. D. Gaulin, and N. P. Armitage, Nat. Phys. **12**, 361 (2015), 1501.05638 .

[52] P. Q. Mantas, J. Eur. Ceram. Soc. **19**, 2079 (1999).

[53] A. K. Jonscher, J. Electrostat. **3**, 53 (1977).

[54] J. Goura, J. Brambleby, P. A. Goddard, and V. Chandrasekhar, Chem. Eur. J. **21**, 4926 (2015).

[55] M. Hagiwara, J. Magn. Magn. Mater. **177–181**, 89 (1998).

[56] D. W. Davidson and R. H. Cole, J. Chem. Phys. **19**, 1484 (1951).

[57] S. Havriliak and S. Negami, Polymer **8**, 161 (1967).

[58] S. Havriliak Jr. and S. J. Havriliak, J. Non-Crystal. Solids **172-174**, 297 (1994).

[59] R. Zorn, J. Chem. Phys. **116**, 3204 (2002).

[60] D. Hüser, A. J. van Duyneveldt, G. J. Nieuwenhuys, and J. A. Mydosh, J. Phys. C: Solid State Phys. **19**, 3697 (1986).

[61] K. Binder and A. P. Young, Rev. Mod. Phys. **133**, 801 (1986).

[62] V. V. Novikov, A. A. Pavlov, Y. V. Nelyubina, M.-E. Boulon, Boulon, O. A. Varzatskii, Y. Z. Voloshin, and R. E. Winpenny, J. Am. Chem. Soc. **137**, 9792 (2015).

[63] R. Boča, C. Rajnák, J. Titiš, and D. Valigura, Inorg. Chem. **56**, 1478 (2017).

[64] M. I. Youssif, A. A. Bahgat, and I. A. Ali, Egypt. J. Solids **23**, 231 (2000).

[65] N. Couach and A. F. Khoder, in *Magnetic Susceptibility of Superconductors and Other Spin Systems*, edited by R. A. Hein, T. L. Francavilla, and D. H. Liebenberg (Plenum, New York, 1991) p. 25.

[66] A. Edgar, Am. J. Phys. **61**, 943 (1993).

[67] K. Matsuhira, Y. Hinatsu, and T. Sakakibara, J. Phys.: Condensed Matter **13**, L737 (2001).

[68] S. J. Blundell and F. L. Pratt, J. Phys.: Condens. Matter **16**, R771 (2004).

[69] D. Gatteschi and R. Sessoli, Angew. Chem. Int. Ed. **42**, 268 (2003).

[70] S. Hill, S. Datta, J. Liu, R. Inglis, C. J. Milios, P. L. Feng, J. J. Henderson, E. d. Barco, E. K. Brechin, and D. N. Hendrickson, Dalton Trans. **39**, 4693 (2010).

[71] C. Cadiou, M. Murrie, C. Paulsen, V. Villar, W. Wernsdorfer, and R. E. P. Winpenny, Chem. Comm. , 2666– (2001).

[72] D. Gatteschi, M. Fittipaldi, C. Sangregorio, and L. Sorace, Angew. Chem. Int. Ed. **51**, 4792 (2012).

[73] R. Orbach, Proc. Phys. Soc. **77**, 821 (1961).

[74] G. Christou, D. Gatteschi, D. N. Hendrickson, and R. Sessoli, MRS Bull. , 66 (2000).

[75] E. K. Brechin, M. Soler, G. Christou, J. Davidson, D. N. Hendrickson, S. Parsons, and W. Wernsdorfer, Polyhedron **22**, 1771 (2003).

[76] W. Huang, J. Xu, D. Wu, X. Huang, and J. Jiang, New J. Chem. **39**, 8650 (2015).

[77] J. Miklovič, D. Valigura, R. Boča, and J. Titiš, Dalton Trans. **44**, 12484 (2015).

[78] P.-H. Lin, N. C. Smythe, S. I. Gorelsky, S. Maguire, N. J. Henson, I. Korobkov, B. L. Scott, J. C. Gordon, R. T. Baker, and M. Murugesu, J. Am. Chem. Soc. **133**, 15806 (2011).

[79] J. Goura, J. Brambleby, C. V. Topping, P. A. Goddard, R. S. Narayanan, A. K. Bar, and V. Chandrasekhar, Dalton Trans. **45**, 9235 (2016).

[80] S. Biswas, J. Goura, S. Das, C. V. Topping, J. Brambleby, P. A. Goddard, and V. Chandrasekhar, Inorg. Chem. **55**, 8422 (2016).

[81] S.-D. Jiang, B.-W. Wang, H.-L. Sun, Z.-M. Wang, and S. Gao, J. Am. Chem. Soc. **133**, 4730 (2011).

[82] C. Y. Huang, J. Magn. Magn. Mater. **51**, 1 (1985).

[83] L. Lundgren, P. Svedlindh, and O. Beckman, J. Magn. Magn. Mater. **25**, 33 (1981).

[84] L. E. Wenger, in *Heidelberg Colloquium on Spin Glasses*, edited by J. L. van Hemmen and I. Morgenstern (Springer, Berlin, 1983) p. 60.

[85] R. M. Fuoss and J. G. Kirkwood, J. Am. Chem. Soc. **63**, 385 (1941).

[86] D. Hüser, L. E. Wenger, A. J. van Duyneveldt, and J. A. Mydosh, Phys. Rev. B **27**, 3100 (1983).

[87] J. L. Tholence, Solid State Commun. **35**, 113 (1980).

[88] S. Shtrikman and E. P. Wohlfarth, Phys. Lett. **85**, 467 (1981).

[89] J. Souletie and J. L. Tholence, Phys. Rev. B **32**, 516 (1985).

[90] M. J. Harris, S. T. Bramwell, D. F. McMorrow, T. Zeiske, and K. W. Godfrey, Phys. Rev. Lett. **79**, 2554 (1997).

[91] S. T. Bramwell and M. J. P. Gingras, Science **294**, 1495 (2001), 0201427 [cond-mat] .

[92] P. W. Anderson, Phys. Rev. **102**, 1008 (1956).

[93] L. Pauling, *The Nature of the Chemical Bond and the Structure of Molecules and Crystals* (Cornell University Press, Ithaca, 1948).

[94] I. A. Ryzhkin, J. Exp. Theor. Phys. **101**, 481 (2005).

[95] J. Snyder, B. G. Ueland, J. S. Slusky, H. Karunadasa, R. J. Cava, and P. Schiffer, Phys. Rev. B **69**, 064414 (2004).

[96] C. Castelnovo, R. Moessner, and S. L. Sondhi, Nature **451**, 42 (2008), 0710.5515 .

[97] L. D. C. Jaubert and P. C. W. Holdsworth, Nat. Phys. **5**, 258 (2009).

[98] M. Nikolo, V. S. Zapf, J. Singleton, J. Jiang, J. D. Weiss, and E. E. Hellstrom, J. Supercond. Nov. Magn. **29**, 2753 (2016).

[99] M. Nikolo, X. Shi, E. S. Choi, J. Jiang, J. D. Weiss, and E. E. Hellstrom, J. Low Temp. Phys. **178**, 188 (2015).

[100] C. J. van der Beek, V. B. Geshkenbein, and V. M. Vinokur, Phys. Rev. B **48** (1993).

[101] M. J. Qin and X. X. Yao, Phys. Rev. B **54**, 7536 (1996).

[102] T. Ishida and R. B. Goldfarb, Phys. Rev. B **41**, 8937 (1990).

[103] R. Cywinski and S. H. Kilcoyne, in *Handbook of Superconducting Materials, volume 2*, edited by D. A. Cardwell and D. S. Ginley (IOP Publishing, Bristol, 2003) p. 1371.

[104] C. P. Bean, Rev. Mod. Phys. **36**, 31 (1964).

[105] A. P. Malozemoff, T. K. Worthington, Y. Yeshurun, F. Holtzberg, and P. H. Kes, Phys. Rev. B **38**, 7203 (1988).

[106] F. Gömöry and S. Takács, Physica C **217**, 297 (1993).

[107] P. W. Anderson, Phys. Rev. Lett. **9**, 309 (1962).

[108] P. W. Anderson and Y. B. Kim, Rev. Mod. Phys. **36**, 39 (1964).

[109] M. Nikolo, Supercond. Sci. Technol. **6**, 618 (1993).

[110] M. Nikolo and R. B. Goldfarb, Phys. Rev. B **39**, 6615 (1989).

[111] R. B. Goldfarb, M. Lelental, and C. A. Thompson, in *Magnetic Susceptibility of Superconductors and Other Spin Systems*, edited by R. A. Hein, T. L. Francavilla, and D. H. Liebenberg (Plenum, New York, 1991) p. 49.

[112] R. B. Goldfarb, A. F. Clark, A. I. Braginski, and A. J. Panson, Cryogenics **27**, 475 (1987).

[113] J. R. Friedman and M. P. Sarachik, Annu. Rev. Condens. Matter Phys. **1**, 109 (2010).

[114] R. A. Layfield, Organometallics **33**, 1084 (2014).

[115] D. Gatteschi, Adv. Mater. **6**, 635 (1994).

[116] J. D. Rinehart and J. R. Long, Chem. Sci. **2**, 2078 (2011).

[117] D. N. Woodruff, R. E. P. Winpenny, and R. A. Layfield, Chem. Rev. **113**, 5110 (2013).

[118] A. Upadhyay, S. K. Singh, C. Das, R. Mondol, S. K. Langley, K. S. Murray, G. Rajaraman, and M. Shanmugam, Chem. Commun. **50**, 8838 (2014).

[119] M. Sugita, T. Ishikawa, S. Koshihara, and Y. Kaizu, Inorg. Chem. **45**, 1299 (2006).

[120] J. D. Rinehart, M. Fang, W. J. Evans, and J. R. Long, J. Am. Chem. Soc. **133**, 14236 (2011).

[121] T. D. Pasatoiu, J.-P. Sutter, A. M. Madalan, F. Z. C. Fellah, C. Duhayon, and M. Andruh, Inorg. Chem. **50**, 5890 (2011).

[122] S. R. Bayly, Z. Xu, B. O. Patrick, S. J. Rettig, M. Pink, R. C. Thompson, and C. Orvig, Inorg. Chem. **42**, 1576 (2003).

[123] C. A. Barts, S. R. Bayly, P. W. Read, B. O. Patrick, R. C. Thompson, and C. Orvig, Inorg. Chem. **47**, 2280 (2008).

[124] T. Shiga, N. Ito, A. Hidaka, H. Okawa, S. Kitagawa, and M. Ohba, Inorg. Chem. **46**, 3492 (2007).

[125] A. Upadhyay, C. Das, S. K. Langley, K. S. Murray, A. K. Srivastava, and M. Shanmugam, Dalton Trans. **45**, 3616 (2016).

[126] C. P. Landee, D. M. Mudgett, and B. M. Foxman, Inorganica Chim. Acta **186**, 45 (1991).

[127] S. K. Singh, N. K. Tibrewal, and G. Rajaraman, Dalton Trans. , 10897.

[128] F.-C. Hsu, J.-Y. Luo, K.-W. Yeh, T.-K. Chen, T.-W. Huang, P. M. Wu, Y.-C. Lee, Y.-L. Huang, Y.-Y. Chu, D.-C. Yan, and M.-K. Wu, Proc. Natl. Acad. Sci. U.S.A. **105**, 14262 (2008).

[129] T. M. McQueen, Q. Huang, V. Ksenofontov, C. Felser, Q. Xu, H. Zandbergen, Y. S. Hor, J. Allred, A. J. Williams, D. Qu, J. Checkelsky, N. P. Ong, and R. J. Cava, Phys. Rev. B **79**, 014522 (2009).

[130] S. Margadonna, Y. Takabayashi, Y. Ohishi, Y. Mizuguchi, Y. Takano, T. Kagayama, T. Nakagawa, M. Takata, and K. Prassides, Phys. Rev. B **80**, 064506 (2009).

[131] S. Medvedev, T. M. McQueen, I. A. Troyan, T. Palasyuk, M. I. Eremets, R. J. Cava, S. Naghavi, F. Casper, V. Ksenofontov, G. Wortmann, and C. Felser, Nat. Mater. **8**, 630 (2009).

[132] Q. Wang, Z. Li, W.-H. Zhang, Z. Zhang, J.-S. Zhang, W. Li, H. Ding, Y.-B. Ou, P. Deng, K. Chang, J. Wen, C.-L. Song, K. He, J.-F. Jia, S.-H. Ji, Y.-Y. Wang, L.-L. Wang, X. Chen, X.-C. Ma, and Q.-K. Xue, Chin. Phys. Lett. **29**, 037402 (2012).

[133] D. Liu, W. Zhang, D. Mou, J. He, Y.-b. Ou, Q.-Y. Wang, Z. Li, L. Wang, L. Zhao, S. He, Y. Peng, X. Liu, C. Chen, L. Yu, G. Liu, X. Dong, J. Zhang, C. Chen, Z. Xu, J. Hu, X. Chen, X. Ma, Q. Xue, and X. J. Zhou, Nat. Commun. **3**, 931 (2012).

[134] S. He, J. He, W. Zhang, L. Zhao, D. Liu, X. Liu, D. Mou, Y.-b. Ou, Q.-Y. Wang, Z. Li, L. Wang, Y. Peng, Y. Liu, C. Chen, L. Yu, G. Liu, X. Dong, J. Zhang, C. Chen, Z. Xu, X. Chen, X. Ma, Q. Xue, and X. J. Zhou, Nat. Mater. **12**, 605 (2013).

[135] V. Svitlyk, M. Raba, V. Dmitriev, P. Rodière, P. Toulemonde, D. Chernyshov, and M. Mezouar, Phys. Rev. B **96**, 014520 (2017).

[136] Y. Miyata, K. Nakayama, K. Sugawara, T. Sato, and T. Takahashi, Nat. Mater. **14**, 775 (2015).

[137] J. Guo, S. Jin, G. Wang, S. Wang, K. Zhu, T. Zhou, M. He, and X. Chen, Phys. Rev. B **82**, 180520 (2010).

[138] A. F. Wang, J. J. Ying, Y. J. Yan, R. H. Liu, X. G. Luo, Z. Y. Li, X. F. Wang, M. Zhang, G. J. Ye, P. Cheng, Z. J. Xiang, and X. H. Chen, Phys. Rev. B **83**, 060512 (2011).

[139] A. Krzton-Maziopa, Z. Shermadini, E. Pomjakushina, V. Pomjakushin, M. Bendele, A. Amato, R. Khasanov, H. Luetkens, and K. Conder, J. Phys. Condens. Matter **23**, 052203 (2011).

[140] T. P. Ying, X. L. Chen, G. Wang, S. F. Jin, T. T. Zhou, X. F. Lai, H. Zhang, and W. Y. Wang, Sci. Rep. **2**, 426 (2012).

[141] M. Burrard-Lucas, D. G. Free, S. J. Sedlmaier, J. D. Wright, S. J. Cassidy, Y. Hara, A. J. Corkett, T. Lancaster, P. J. Baker, S. J. Blundell, and S. J. Clarke, Nat. Mater. **12**, 15 (2012).

[142] A. Krzton-Maziopa, E. V. Pomjakushina, V. Y. Pomjakushin, F. von Rohr, A. Schilling, and K. Conder, J. Phys. Condens. Matter **24**, 382202 (2012).

[143] D. Guterding, H. O. Jeschke, P. J. Hirschfeld, and R. Valentí, Phys. Rev. B **91**, 041112 (2015).

[144] H. Sun, D. N. Woodruff, S. J. Cassidy, G. M. Allcroft, S. J. Sedlmaier, A. L. Thompson, P. A. Bingham, S. D. Forder, S. Cartenet, N. Mary, S. Ramos, F. R. Foronda, B. H. Williams, X. Li, and S. J. Clarke, Inorg. Chem. **54**, 1958 (2015).

[145] X. F. Lu, N. Z. Wang, H. Wu, Y. P. Wu, D. Zhao, X. Z. Zeng, X. G. Luo, T. Wu, W. Bao, G. H. Zhang, F. Q. Huang, Q. Z. Huang, and X. H. Chen, Nat. Mater. **14**, 325 (2014).

[146] U. Pachmayr, F. Nitsche, H. Luetkens, S. Kamusella, F. Brückner, R. Sarkar, H.-H. Klauss, and D. Johrendt, Angew. Chem. Int. Ed. **54**, 293 (2015).

[147] W. Chen, C. Zeng, E. Kaxiras, and Z. Zhang, Phys. Rev. B **93**, 064517 (2016).

[148] D.-Y. Liu, Z. Sun, and L.-J. Zou, New J. Phys. (2017), 10.1088/1367-2630/aa5a71.

[149] Y. P. Wu, D. Zhao, X. R. Lian, X. F. Lu, N. Z. Wang, X. G. Luo, X. H. Chen, and T. Wu, Phys. Rev. B **91**, 125107 (2015).

[150] R. Khasanov, H. Zhou, A. Amato, Z. Guguchia, E. Morenzoni, X. Dong, G. Zhang, and Z. Zhao, Phys. Rev. B **93**, 224512 (2016).

[151] V. Thampy, J. Kang, J. A. Rodriguez-Rivera, W. Bao, A. T. Savici, J. Hu, T. J. Liu, B. Qian, D. Fobes, Z. Q. Mao, C. B. Fu, W. C. Chen, Q. Ye, R. W. Erwin, T. R. Gentile, Z. Tesanovic, and C. Broholm, Phys. Rev. Lett. **108**, 107002 (2012).

[152] J. W. Lynn, X. Zhou, C. K. H. Borg, S. R. Saha, J. Paglione, and E. E. Rodriguez, Phys. Rev. B **92**, 1 (2015), 1507.0431 .

[153] P. J. C. King, R. de Renzi, S. P. Cottrell, A. D. Hillier, and S. F. J. Cox, Physica Scripta **88**, 068502 (2013).

[154] F. L. Pratt, Physica B **289-290**, 710 (2000).

[155] N. R. Davies, M. C. Rahn, H. C. Walker, R. A. Ewings, D. N. Woodruff, S. J. Clarke, and A. T. Boothroyd, Phys. Rev. B **94**, 144503 (2016).

[156] R. M. Ziff, Phys. Rev. Lett. **69**, 2670 (1992).

[157] D. Stauffer and A. Aharony, *Introduction to Percolation Theory* (Taylor & Francis Ltd, London, 1992).

[158] R. Bjørk and C. R. H. Bahl, Appl. Phys. Lett. **103**, 102403 (2013).

[159] A. E. Böhmer, T. Arai, F. Hardy, T. Hattori, T. Iye, T. Wolf, H. v. Löhneysen, K. Ishida, and C. Meingast, Phys. Rev. Lett. **114**, 027001 (2015).

[160] L. E. Wenger and P. H. Keesom, Phys. Rev. B **13**, 4053 (1976).

[161] R. Khasanov, H. Luetkens, A. Amato, H.-H. Klauss, Z.-A. Ren, J. Yang, W. Lu, and Z.-X. Zhao, Phys. Rev. B **78**, 092506 (2008).

[162] R. E. Walstedt and L. R. Walker, Phys. Rev. B **9**, 4857 (1974).